



저작자표시-비영리-변경금지 2.0 대한민국

이용자는 아래의 조건을 따르는 경우에 한하여 자유롭게

- 이 저작물을 복제, 배포, 전송, 전시, 공연 및 방송할 수 있습니다.

다음과 같은 조건을 따라야 합니다:



저작자표시. 귀하는 원저작자를 표시하여야 합니다.



비영리. 귀하는 이 저작물을 영리 목적으로 이용할 수 없습니다.



변경금지. 귀하는 이 저작물을 개작, 변형 또는 가공할 수 없습니다.

- 귀하는, 이 저작물의 재이용이나 배포의 경우, 이 저작물에 적용된 이용허락조건을 명확하게 나타내어야 합니다.
- 저작권자로부터 별도의 허가를 받으면 이러한 조건들은 적용되지 않습니다.

저작권법에 따른 이용자의 권리는 위의 내용에 의하여 영향을 받지 않습니다.

이것은 [이용허락규약\(Legal Code\)](#)을 이해하기 쉽게 요약한 것입니다.

[Disclaimer](#)

공학박사 학위논문

**Investigation on InSb Epitaxial Growth  
and Surface Passivation to Improve  
Device Performances**

적외선 검출소자 특성향상을 위한 InSb 성장 및  
표면 보호막에 대한 연구

2016년 2월

서울대학교 대학원  
재료공학부  
박 세 훈

## **Abstract**

# **Investigation on InSb Epitaxial Growth and Surface Passivation to Improve Device Performances**

**Sehun Park**

**Department of Materials and Science and Engineering**

**College of Engineering**

**Seoul National University**

Photodetectors (PDs) detecting mid-wavelength infrared (MWIR) region has been developed for the military applications for the first time by some developed countries, these days they have been widely used in the field of industry, medical and astronomy. Hence the market of IR PDs has been expanded significantly. However, the fabrication technology of IR PDs was selected as a key technology for military application, exportation to abroad or other countries are strictly restricted. On the other hand, the fabrication technology of IR PDs in Korea is positioned at low level to study fundamental technologies hence huge gap are existed.

Indium antimonide (InSb) is one of the suitable materials for MWIR detection due to the band gap of 0.23 eV at 77 K and its high electron mobility. To fabricate IR PDs, diffusion or ion-implantation of p-type dopant into n-type InSb substrate were generally adopted. However, these methods produced the surface defects, acting as the trap centers. Hence, device performances can be degraded due to the leakage current. In order to improve device performances, epitaxial growth of InSb was conducted. Unlike to other As, P and N related material growth, it has lots of difficulties in the epitaxial growth of InSb. Even though there are lots of difficulties, in this thesis, InSb epitaxial layers were grown by low pressure metalorganic chemical vapor deposition to obtain high quality of InSb epitaxial layers and its morphological, structural, electrical and optical properties was systematically investigated. For the device application, surface passivations for InSb were thoroughly investigated using ZnS films.

First prerequisites to growth high quality of InSb epitaxial layers was how to prepare the substrate for the epitaxial growth, called the preparation of epi-ready substrate. Although the preparation of well prepared substrate is very important process, it was not easy due to the low vapor pressure of Sb and no hydride precursors of Sb. Due to the these facts, thermal cleaning without Sb overpressure was reported. I noticed, however, that Sb overpressure during thermal cleaning process is necessary process in order to suppress undesirable byproducts. The thermal cleaning under H<sub>2</sub> ambient produces the In droplets surrounded by rectangular etch pits on InSb surface due to the selectively evaporation of Sb. Because, Sb has a much higher vapor pressure

than that of In. The formation of rectangular etch pits were reflected by the etching characteristics of zincblende structures. This preparation method of substrates found to influence on the crystal quality of InSb epitaxial layers.

In order to growth high quality of InSb epitaxial layers, growth parameters i.e., V/III ratio and growth temperature, were varied to find optimized growth conditions and its morphological, structural, electrical and optical properties were investigated. Optimized growth condition in this thesis found to be a growth temperature of 490 °C under V/III ratio of 8.8. With decreasing V/III ratio at low growth temperature such as 450 and 470 °C, In droplets were formed on the surface due to the insufficient supply of Sb. They were removed with increasing V/III ratio. At low V/III ratio at higher temperature of 490 or 510 °C, the formation of In droplets were prohibited due to the sufficient Sb supply, implying that TMSb was not fully decomposed in the investigated growth temperature ranges. Based on the growth behaviors of InSb, InSb growth rate was controlled by the surface reaction kinetics, called kinetically limited. It was dependent on the TMIn mole fraction but independent on the TMSb mole fraction. These growth behaviors represented that TMIn was also not fully decomposed in this growth temperature regions.

From the optical properties analysis, two dominant phenomena were observed. Growth parameters influenced on the optical quality of InSb epilayers. When the InSb were grown at non-stoichiometric growth condition, indium interstitial defects were incorporated into InSb epitaxial layers, affecting the reduction of band gap energy. Second, the origin of new PL emission, which has not been reported yet, was investigated. It was originated from the carbon due to the uncomplete decomposition of metalorganic

precursors.

Properties of ZnS were studied for the InSb surface passivation material. Until now, SiO<sub>2</sub> passivation material has been widely used but it showed degradation during the deposition or after deposition at the interface regions. In order to overcome these problems, new material was studied. After deposition of ZnS, interface properties showed the similar quality with interface trap density of  $2 \times 10^{11} \text{ cm}^{-2} \text{ eV}^{-1}$  compared to SiO<sub>2</sub>. It was found that surface leakage currents were reduced by depositing slightly non-stoichiometric ZnS films due to the charge compensation effects. It produces the flat-band voltage conditions, restricting the formation of surface leakage current paths.

The effectiveness of ZnS passivation deposited under optimized condition was investigated. The dark current of the sample passivated ZnS films were more than one order of magnitude reduction compared to the unpassivated sample. By comparing the sample passivated SiO<sub>2</sub>, it was also much effective way to reduce surface leakage current. Differential resistance area product at zero bias ( $R_0A$ ) was extracted from the current-voltage measurement. It shows that  $1.6 \times 10^4 \text{ } \Omega \text{ cm}^2$  was obtained from the ZnS passivated InSb devices. It was decreased to  $2 \times 10^3 \text{ } \Omega \text{ cm}^2$  and  $31 \text{ } \Omega \text{ cm}^2$  when the SiO<sub>2</sub> and unpassivated films were deposited, respectively. The reduction of surface leakage current also influence on the spectral response, responsivity and detectivity. All devices show the spectral response in the wavelength range between 1 to 5.5  $\mu\text{m}$  where maximum intensities were observed near 5.5  $\mu\text{m}$ . However, the strong intensity of spectral response when ZnS deposited was

observed and it was decreased when SiO<sub>2</sub> and unpassivated films were deposited. In case of ZnS deposition sample, spectral response was even observed near 220 K, implying that crystal quality was very high. From the responsivity and detectivity measurements at 77 K, maximum intensity of responsivity was observed near 5.18 μm. The corresponding detectivity show the strong intensity when ZnS films were deposited but it was reduced when InSb surface were not passivated.

---

---

**Key Words:**

Indium antimonide (InSb), Low Pressure Metalorganic Chemical Vapor Deposition (LP-MOCVD), Infrared Photodiodes (IR PDs), *in-situ* thermal cleaning (TC), Photoluminescence (PL), p-type doping, Zinc Sulfide (ZnS), Surface passivation, Dark current, Photoresponse, Responsivity and Detectivity (D\*)

**Student Number:** 2009-20602

---

---

# Contents

<b>Abstract .....</b>	<b>i</b>
<b>Content .....</b>	<b>vi</b>
<b>List of Figures .....</b>	<b>xi</b>
<b>List of Tables .....</b>	<b>xx</b>
<b>Chapter 1. Introduction .....</b>	<b>1</b>
<b>1.1. Infrared fundamentals .....</b>	<b>1</b>
<b>1.1.1. Infrared history .....</b>	<b>1</b>
<b>1.1.2. Infrared radiation .....</b>	<b>3</b>
<b>1.1.3. Infrared sources.....</b>	<b>4</b>
<b>1.1.4. Concept of blackbody radiation .....</b>	<b>4</b>
<b>1.1.5. Radiation transmission window at atmospheric ambient.....</b>	<b>8</b>
<b>1.1.6. Selection of IR wavelength .....</b>	<b>9</b>
<b>1.2. Photo-detection principle and materials for MWIR detection.....</b>	<b>12</b>
<b>1.2.1. Operating principle of photodiodes .....</b>	<b>12</b>
<b>1.2.2. Application fields of IR photodiodes.....</b>	<b>13</b>
<b>1.2.3. Materials for MWIR photodetection .....</b>	<b>17</b>
<b>1.3. A survey of previous researches for InSb MWIR photodiodes.....</b>	<b>23</b>
<b>1.3.1. Previous research of MWIR photodiodes fabricated by diffusion and ion implantation .....</b>	<b>23</b>
<b>1.3.2. Previous research of MWIR photodiodes fabricated by crystal growth techniques .....</b>	<b>24</b>
<b>1.4. Organization of this thesis .....</b>	<b>32</b>

1.5. Bibliography .....	34
-------------------------	----

## **Chapter 2. Experimental methods: material growth, device**

### **fabrication and characterization tools..... 40**

2.1. Material growth system: Low-Pressure Metalorganic Chemical Vapor Deposition (LP-MOCVD) .....	40
2.1.1. LP-MOCVD system @ SNU.....	40
2.1.2. Metalorganic (MO) source materials.....	44
2.1.3. InSb substrate preparation.....	45
2.1.4. Epitaxial growth procedures .....	46
2.2. Dielectric deposition systems.....	49
2.2.1. Plasma Enhanced Chemical Vapor Deposition (PECVD).....	49
2.2.2. Electron Beam Evaporation .....	49
2.3. Device fabrication methods .....	50
2.3.1. Sample preparation.....	50
2.3.2. Mesa etching .....	50
2.3.3. Dielectric deposition.....	54
2.3.4. Metallization .....	54
2.4. Characterization tools.....	56
2.4.1. Atomic Force Microscopy .....	56
2.4.2. Ellipsometry.....	56
2.4.3. High resolution X-Ray Diffraction.....	57
2.4.4. Scanning Electron Microscopy.....	57
2.4.5. Transmission Electron Microscopy .....	58
2.4.6. Secondary Ion Mass Spectroscopy.....	58

2.4.7. Energy Dispersive X-ray Spectroscopy .....	58
2.4.8. X-ray Photoelectron Spectroscopy .....	58
2.4.9. Auger Electron Spectroscopy .....	59
2.4.10. Photoluminescence .....	59
2.4.11. Capacitance-Voltage measurement .....	60
2.4.12. Current-Voltage measurement .....	60
2.4.13. Hall measurement .....	61

### **Chapter 3. Surface treatment ambient on the quality of InSb**

<b>epitaxial layers .....</b>	<b>63</b>
3.1. Introduction .....	63
3.2. Motivation .....	67
3.3. Theoretical background .....	70
3.4. Experimental procedures .....	73
3.5. <i>ex-situ</i> wet chemical etching of InSb substrate .....	74
3.6. <i>in-situ</i> thermal cleaning (TC) of InSb substrat .....	80
3.6.1. H <sub>2</sub> ambient .....	80
3.6.1.1. Effects of TC temperatures on InSb substrate .....	80
3.6.1.2. Formation of indium droplets surrounded by rectangular etch pits .....	80
3.6.2. TMSb ambient .....	87
3.6.2.1. Effects of TC temperatures on InSb substrate .....	87
3.6.2.2. Effects of TMSb mole fraction on InSb surface morphology .....	88
3.7. Effects of thermal cleaning ambient on the quality of InSb epilayers .....	94
3.7.1. Influence on the crystallinity .....	94

3.7.2. Origin of the degraded quality of InSb epilayers .....	95
3.8. Summary .....	99
3.9. Bibliography .....	100

## **Chapter 4. Growth and characterization of InSb epitaxial**

<b>layers .....</b>	<b>104</b>
4.1. Introduction .....	104
4.2. Motivation .....	107
4.3. Experimental procedures.....	109
4.4. Epitaxial growth of unintentionally doped InSb .....	111
4.4.1. Effect of growth parameters on InSb surface morphologies .....	111
4.4.2. Effects of growth parameters on InSb crystallinity.....	112
4.4.3. Growth behavior of InSb grown using TMIIn and TMSb .....	113
4.5. Optical analysis of unintentionally doped InSb .....	121
4.5.1. Near band edge emission shift .....	121
4.5.2. Carbon impurity related PL emission .....	133
4.6. p-type doping in InSb.....	137
4.7. Summary .....	140
4.8. Bibliography .....	142

## **Chapter 5. ZnS surface passivation of InSb photodiodes and its device performances.....**

5.1. Introduction .....	148
5.2. Motivation .....	151
5.3. Experimental procedures.....	154

5.4. Interfacial properties of Au/ZnS/InSb MIS structures .....	155
5.4.1. Effects of deposition rate on interface trap density ( $D_{it}$ ).....	155
5.4.2. Effects of deposition rate on fixed charge density ( $N_f$ ).....	158
5.4.3. Chemical composition analysis of ZnS films.....	159
5.4.4. Defect origin analysis of S-deficient ZnS films .....	160
5.5. Surface leakage currents of ZnS passivated InSb PDs.....	165
5.5.1. Theoretical background .....	165
5.5.2. The dependence of deposition rates on the surface leakage currents ....	166
5.6. Device performance .....	172
5.6.1. Dark current .....	172
5.6.2. Spectral response.....	173
5.6.3. Responsivity and Detectivity ( $D^*$ ).....	179
5.7. Summary .....	183
5.8. Bibliography .....	185
<b>Chapter 6. Conclusions .....</b>	<b>192</b>
<b>Abstract (in Korean) .....</b>	<b>196</b>
<b>Publication List.....</b>	<b>200</b>

## List of Figures

Fig 1.1 A chart of the electromagnetic spectrum of solar radiation. It was classified by radio, terahertz, infrared, visible, ultraviolet, x-ray and gamma ray. The frequency and wavelength of each spectrum are shown.....	6
Fig. 1.2. Plank's law at various blackbody temperatures and wavelength regimes.....	7
Fig. 1.3. Transmission of the atmosphere for a 6000 ft horizontal path at sea level. Common atmospheric transmission windows are located at 0.7-2 $\mu\text{m}$ , 3-5 $\mu\text{m}$ and 8-12 $\mu\text{m}$ .....	10
Fig. 1.4. Schematic diagram of an IR photodiode system including its components. More detail structures of IR detector is represented in box below.....	14
Fig. 1.5. (a) Schematic band diagram of p-n photodiode with electron-hole pair generation. (b) current-voltage characteristics for the illuminated and non illuminated photodiodes.....	15
Fig. 1.6. Illustration of the various applications for IR detection.....	16
Fig. 1.7. A plot of band gap energy versus lattice constant.....	20

Fig. 1.8. Temperature–composition binary phase diagram of In and Sb, describing the equilibrium of solid with a liquid of InSb.....	22
Fig. 1.9. X-ray diffraction spectra of 3.0 $\mu\text{m}$ thick InSb films grown on InSb, GaAs and GaAs coated Si substrates.....	30
Fig. 1.10. Growth efficiency of $\text{InAs}_{1-x}\text{Sb}_x$ and InSb versus reciprocal temperature. This semi-log plot indicates that the growth rate is thermally activated for both materials. The filled circles are data for InSb from P. K. Chiang.....	31
Fig. 2.1 Schematic illustration of MOCVD including vent-run manifold gas delivery system.....	43
Fig. 2.2 An illustration of InSb device fabrication sequence.....	52
Fig. 2.3 The etching rate of InSb epitaxial layer in the mixture of citric acid and $\text{H}_2\text{O}_2$ . The etching rate is 70 nm/min.....	53
Fig. 2.4 A cryostat system cooled by $\text{LN}_2$ equipped with Agilent 4980A and Keithley 2636A.....	62
Fig. 3.1 A schematic illustration of InSb native oxides formation process when exposed to air. Native oxides are composed of indium oxides ( $\text{In}_2\text{O}_3$ ) and antimony oxides ( $\text{Sb}_2\text{O}_3$ ) and elemental Sb.....	66

Fig. 3.2. Vapor pressure of the III-V elements as a function of temperature.....	69
Fig. 3.3. (a) A XTEM image of air exposed InSb substrate with 24 Å thickness of native oxides. (b) Optical microscopy images of surface etched in lactic: nitric acid (1:1) (c) native oxide thickness measured by ellipsometer depending on the mixture ratio and etching time.....	77
Fig. 3.4. AFM images of InSb surface etched in lactic: nitric acid (10:1) with different etching time (a) 0 sec, (b) 30 sec, (c) 120 sec, (d) 300 sec. (e) A graph of RMS roughness depending on the etching time.....	78
Fig. 3.5. Native oxides thickness and RMS roughness depending on the thermal cleaning temperature and corresponding AFM images of (b) after H <sub>2</sub> purge (c) 495 °C, (d) 505 °C, and (e) 515 °C for 5 min in H <sub>2</sub> ambient.....	79
Fig. 3.6. (a) A SEM images of InSb surface thermally treated at 515 °C in H <sub>2</sub> ambient. Corresponding EDS mapping images of (b) indium and (c) antimony.....	84
Fig. 3.7. (a) An enlarged SEM images of InSb surface thermally treated at 515 °C in H <sub>2</sub> ambient. (b) XSEM image cleavaged by A-A' direction. The angle between (100) and (111) is 54.4°.....	85
Fig. 3.8. Illustration of native oxide desorption and In droplet formation (a) native oxides re-growth (b) thermal desorption of native oxides (c) Sb	

evaporation from InSb surface (d) In droplet formation with rectangular etch pits.....86

Fig. 3.9. (a) SEM image of InSb thermally annealed at 515 °C for 300 sec (TMSb molar flow rate= 18.1 μmol/min) (b) Native oxide thickness and corresponding RMS roughness of InSb substrates thermally annealed at 495 °C and 515 °C. A data obtained H<sub>2</sub> ambient were included for the comparison.....90

Fig. 3.10. AFM images of InSb annealed under different TMSb molar flow rate of (a) 18.1, (b) 63.4, (c) 108.7, and (d) 154.0 μmol/min and (e) its corresponding surface line profiles.....91

Fig. 3.11. Illustration of chemical potential of Sb between gas phases (vapor) and substrate surface (solid) (a)  $P_{Sb}$  at solid >  $P_{Sb}$  at vapor (b)  $P_{Sb}$  at solid =  $P_{Sb}$  at vapor (c)  $P_{Sb}$  at solid <  $P_{Sb}$  at vapor.....92

Fig. 3.12. Raman results of InSb samples thermally treated under TMSb ambient. TMSb molar flow rate was varied from 18.1 to 154.0 μmol/min.....93

Fig. 3.13. X-ray rocking curve of InSb epitaxial layers grown on InSb substrates thermally treated under either H<sub>2</sub> or TMSb ambient. Reciprocal space mapping results of (004) reflection for the two InSb epitaxial layers grown on the substrate annealed under (b) H<sub>2</sub> and (c) TMSb ambient, respectively.....97

Fig. 3.14. Photoluminescence of InSb epilayers grown on InSb substrate thermally treated under H <sub>2</sub> and TMSb ambient. The PL emission was obtained at 10 K with a power density of 400 mW.....	98
Fig. 4.1. Band structure of InSb at 300 K.....	106
Fig. 4.2. (a) A technique for growth rate measurements and (b) its result measured surface profiler.....	110
Fig. 4.3. AFM images of InSb epilayers grown at different V/III ratio and growth temperature.....	118
Fig. 4.4. FWHM of InSb grown at different (a) V/III ratio and (b) growth temperature.....	119
Fig. 4.5. (a) Arrhenius plot of the growth rate of InSb for TMIn/TMSb. Growth rate of InSb at 490 °C for varying (a) TMIn mole fraction and (b) TMSb mole fraction.....	120
Fig. 4.6. . (a) PL spectrum of InSb samples grown at different V/III ratio range from 2.2 to 13.2. (b) Peak position and FWHM of NBE emission with a dependence of V/III ratio .....	128
Fig. 4.7. Carrier concentration and Hall mobility for the InSb samples grown at various V/III ratios. Hall measurements were performed at 77 K under	

applied magnetic field of 0.37 T.....129

Fig. 4.8. (a) SEM image of InSb sample grown at V/III ratio of 2.2. Inset shows the enlarged image of droplet. (b) Chemical composition of droplet was confirmed by HCl etching and EDX analysis, indicating In droplet. (c) PL intensity of NBE emission with a dependence of V/III ratio.....130

Fig. 4.9. (a) Band edge fluctuation due to incorporated donor type of defects (b) Plots of energy and density of states. Two types of density of state due to perturbed and unperturbed conduction band ( $E_C$ ).....131

Fig. 4.10. (a) Raman spectrum of all InSb samples (b) Intensity ratio of TO/LO and FWHM of LO phonon with a dependence of V/III ratio.....132

Fig. 4.11. (a) PL spectrum of InSb samples grown at different  $T_G$  ranged from 450 to 510 °C. PL spectrum was measured at 10 K with a power density of 400 mW/cm<sup>2</sup>. The inset shows the PL spectrum of bulk InSb. (b) The relative PL intensity of the Peak #4 was represented as a function of  $T_G$ .....134

Fig. 4.12. SIMS depth profile of carbon in InSb epilayer/InSb substrate structures. Carbon concentration in InSb samples grown at (a) V/III ratio of 2.2 and 8.8 and (b)  $T_G$  of 450, 470 and 490 °C. SIMS depth profiles of bulk InSb was inserted as a reference .....135

Fig. 4.13. (a) Hole concentration and Hall mobility of Zn doped InSb as a

function of (a) DEZn mole fraction (b) growth temperature.....139

Fig. 5.1. (a) Unpassivated InSb IR PDs structures. Enlarged square express the detail structure of surface with dangling bonds, which acting as trap sites for the increase of surface leakage current. (b) A possible solution is passivation layer deposition on InSb IR PDs.....150

Fig. 5.2. (a) Capacitance-voltage curves of Au/ZnS/InSb MIS structures. The ideal C-V curves is inserted as a reference. (b) The calculated  $D_{it}$  at the mid gap as a function of ZnS deposition rate.....156

Fig. 5.3. (a) An XPS spectrum of In 3d region recorded at the interface regions of ZnS/InSb deposited at 0.5 A/sec. The deconvolution of In 3d spectra into three different chemically shifted components of In-Sb, In-S and In-O binding. (b) Relative intensity ratio of its binding area to total area of XPS peak.....157

Fig. 5.4. The fixed charge density ( $N_f$ ) calculated from flat band voltage shifts as a function as ZnS deposition rate. ....162

Fig. 5.5. Intensity ratio of Zn/S at the interface of ZnS/InSb obtained from AES depth profiles measurements.....163

Fig. 5.6. PL emission spectra of ZnS films deposited at different deposition rates.....164

Fig. 5.7. Schematic illustration of  $1/R_oA$  versus perimeter to area (P/A) ratio. This graph represents the dependence of ideal passivation, non-ideal passivation and unpassivation on  $R_oA$  products.....168

Fig. 5.8. Optical image of the sample for VADA measurements.....169

Fig. 5.9. (a) I-V curved for the ZnS passivated InSb pn IR PDs (b) dependence of  $1/R_oA$  vs P/A ratio for the InSb pn diodes.....170

Fig. 5.10. Schematic images of (a) unpassivated InSb pn structure and (b) ZnS passivated InSb pn structure and corresponding band diagrams were represented.....171

Fig. 5.11. Schematic images of (a) unpassivated mesa type InSb pin structure and (b) ZnS passivated mesa type InSb pin structure.....175

Fig. 5.12. (a) Dark current density versus applied voltage of the unpassivated,  $SiO_2$  and the ZnS passivated photodiodes measured at 80 K. (b) Differential resistance area product at zero bias ( $R_oA$ ) vs applied voltage of three samples.....176

Fig. 5.13. (a) Photograph of measured samples. Contacts were connected by Au wiring to the sample holder. (b) Optical microscope image of ZnS passivated InSb photodiodes.....177

Fig. 5.14. (a) Spectral response of unpassivated and passivated sample.

Temperature dependence of spectral response of (b) unpassivated and (c) passivated sample.....178

Fig. 5.15. (a) Responsivity and (b) detectivity ( $D^*$ ) of three samples measured at 77 K under zero bias.....181

## List of Tables

Table 1.1 Spectral regions of IR ranges.....	6
Table 1.2. The strength and weakness of IR ranges.....	11
Table 1.3. Physical properties of HgCdTe and InSb.....	21
Table 2.1. MO source materials used in this study for MOCVD growth.....	48
Table 4.1. Electron effective mass of III-V semiconductors.....	106

# **Chapter 1. Introduction**

## **1.1. Infrared fundamentals**

### **1.1.1. Infrared (IR) history**

From the historical views, visible light is the only known part of the electromagnetic spectrum. The first “infrared (IR) detection systems” were used by the ancient Egyptians in around 3000 B. C. as they moved their hands over the body sensing changes in temperatures. Later, in 400 B.C., the Greek philosopher and physician Hippocrates wrote, “In whatever part of the body with excess heat or cold is felt, the disease is to be discovered”. He would identify the disease parts from human body by covering the thin layer of mud. If the covered mud would be dried faster, compared to the other parts, he recognizes the disease part and tissues due to the more radiated heat than healthy parts. These are the basis for the modern IR medical imaging where painful parts of human body is non-invasively recognized and its position through the detection of abnormal IR radiation emitted from a human body is easily detected. Through old techniques, infrared photodetector technology has been significantly improved and provides for sensitivity of a few thousandths of a degree Celsius over large area with a high resolution. The first discovery of IR electromagnetic radiation was done by astronomer and musician Friedrich Wilhelm Herschel, commonly known as William Herschel when he worked on designing a telescope for solar observation [1]. He used the various filter for sun light and found that there seemed to pass

different amount of heat. Based on the different colors corresponded to different temperatures, Herschel used a prism to pass the sun light and used a thermometer to measure the temperature of refracted light in 1800 [1]. The experiment verified and confirmed his hypothesis that the amount of heat can be changed with changing color, increasing in temperature from blue to red and even to “invisible” region beyond the red. He observed that temperature increased from the blue to the red regions of the sun light spectrum and when he placed a thermometer at the red region, where no refracted light was visible so he observed the highest temperature. This means that, even though one could not see it, some form of radiation was incident upon the last thermometer, causing it to heat up. Thus, IR radiation, firstly called calorific rays, was firstly discovered.

Following Herschel’s experiment in 1800, a number of scientists began to more closely investigate the IR region of the spectrum. Most IR detectors like thermometer were invented in the similar times. It absorbs the radiation and produces a change in some temperature dependent property of the material which can be measured such as volume. A few years later, Nobile made the first thermopile in 1829 composed of a series of thermocouples that was orders of magnitude more sensitive than the thermometer [2]. About half a century later, Langley’s invention of the bolometer used platinum temperature-dependent electrical resistance as a basis to detect a cow from a quarter of a mile away [3]. Whether the incident radiation induces a change in volume, voltage, resistance or capacitance of the material, these infrared detectors are generally wavelength independent and inherently slow, but can operating without cooling.

### **1.1.2. Infrared radiation**

All objects are composed of continually vibrating atoms. The atoms containing more high energy vibrates more frequently. The vibration of all particles including these atoms generates electromagnetic waves. The higher temperature of an object, the faster the vibration result in the higher the spectral radiation energy. As a result, all objects are continually emitting radiation at a rate with wavelength distribution that depends on the temperature of the object and its spectral emissivity.

The electromagnetic radiation spectrum from solar radiation is useful in describing the characteristics of materials. This spectrum can be classified by the wavelength into radio waves, terahertz wave, IR wave, visible, ultraviolet (UV), X-ray and gamma rays as shown in Fig. 1.1. An IR radiation is a form of radiated electromagnetic energy, located between visible and terahertz waves. It is composed of five sub-categories, depending on the wavelength as shown in table 1.1. The IR region of electromagnetic radiation covers the range from 0.7  $\mu\text{m}$  to roughly 1 mm. IR ranges are defined as NIR, SWIR, MWIR, LWIR, FIR which are abbreviation of near IR, short wavelength IR, mid wavelength IR, long wavelength IR and far IR, respectively.

### **1.1.3. Infrared source**

As mentioned above, all objects which have a temperature, if its temperature is above 0 K, emits radiation. For example, the human body at room temperature radiates with a maximum spectral intensity at around 10

$\mu\text{m}$  that is located in the region of LWIR, which is beyond the sensitivity range of the human eyes. However, LWIR radiation can be sensed by our skin due to the heat generated from the objects. When the temperature of an object increase to  $\sim 1000$  K, the human eye can see some visible light emitted by the object. However, most of the spectral radiation can not be detected by human eyes. These phenomena can be explained with the blackbody theory.

#### 1.1.4. Concept of blackbody radiation

Radiation emission is usually treated in terms of the concept of a blackbody [4]. A blackbody is an object that absorbs all incident radiation, and conversely according to the Kirchhoff's law, is a perfect radiator. The energy emitted by a blackbody is the maximum theoretical possible for a given temperature. The radiative power, or sometimes represented in the number of photon emitted, and its wavelength distribution are given by the Plank radiation law.

$$W(\lambda, T) = \frac{2\pi hc^2}{\lambda^5} [\exp(\frac{hc}{\lambda kT}) - 1]^{-1} \quad W/(cm^2 \mu m) \quad [\text{eq. 1-1}]$$

$$P(\lambda, T) = \frac{2\pi c}{\lambda^4} [\exp(\frac{hc}{\lambda kT}) - 1]^{-1} \quad \text{photons}/(s \cdot cm^2 \mu m) \quad [\text{eq. 1-2}]$$

Where  $\lambda$  is the wavelength, T is the absolute temperature, h is the Plank's constant, c is the velocity of light, and k is the Boltzmann's constant.

Figure 1.2 shows a plot of these curves for a number of blackbody temperatures. As the temperature increase, the amount of energy emitted at any wavelength increase and the wavelength of peak emission decrease. The latter is described by the Wien's displacement law. Wien's law states the relationship between the temperature of a blackbody and its peak emission wavelength as shown by equation 1-3 and 1-4.

$$\lambda_{mw}T = 2898\mu mK \quad \text{for maximum watts} \quad [\text{eq. 1-3}]$$

$$\lambda_{mp}T = 3670\mu mK \quad \text{for maximum photons} \quad [\text{eq. 1-4}]$$

From the these theory, for instance, we need detectors operating near 10  $\mu\text{m}$  IR ranges if we want to see the objects with around 300 K temperature such as people and animal. For the detection of much hotter objects such as car and jets engines or missiles, the detectors operated at much shorter wavelength in the region from 3 to 5  $\mu\text{m}$  is needed.

## Electromagnetic spectrum of solar radiation

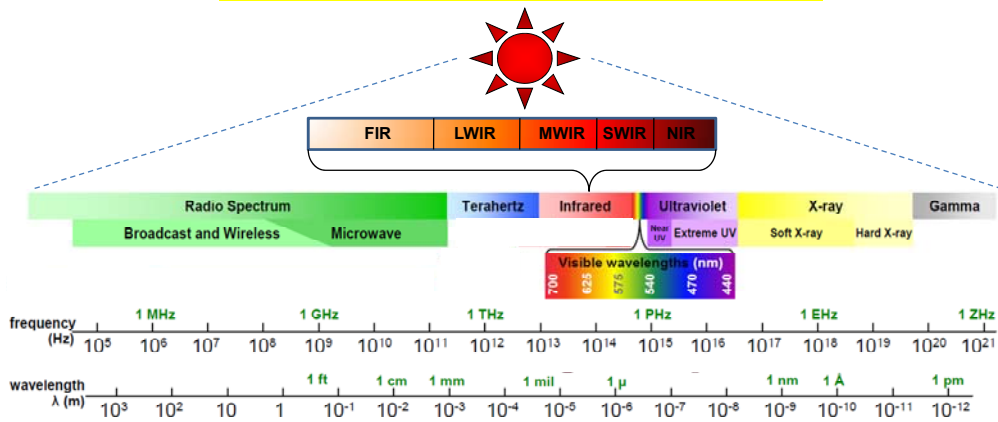


Fig 1.1 A chart of the electromagnetic spectrum of solar radiation. It was classified by radio, terahertz, infrared, visible, ultraviolet, x-ray and gamma ray. The frequency and wavelength of each spectrum are shown.

Wavelength ( $\mu\text{m}$ )	0.7-1.4	1.4-3	3-8	8-15	14-1000
Classification of IR radiation	Near Wavelength IR (NIR)	Short Wavelength IR (SWIR)	Mid Wavelength IR (MWIR)	Long Wavelength IR (LWIR)	Far IR (FIR)

Table 1.1 Spectral regions of IR ranges

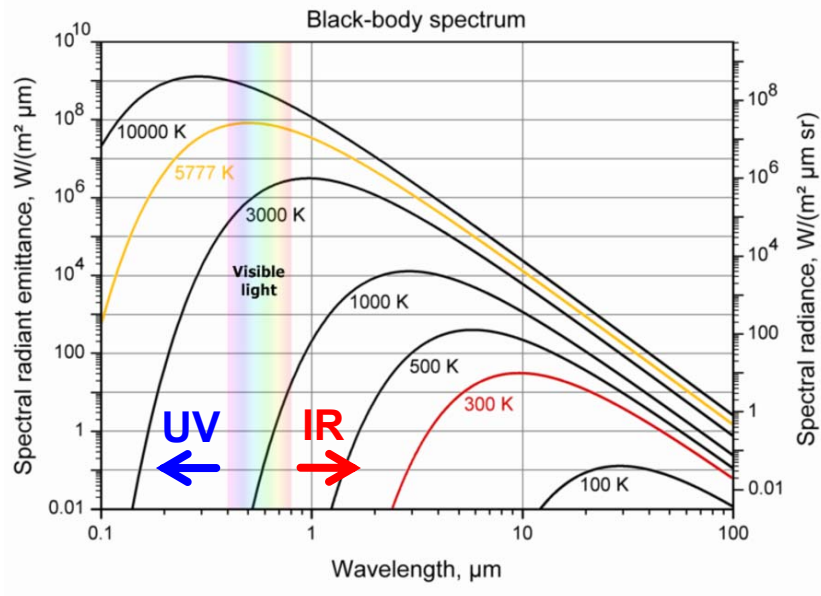


Fig. 1.2. Planck's law at various blackbody temperatures and wavelength regimes

### **1.1.5. Radiation transmission window at atmospheric ambient**

Most of the above mentioned application requires IR transmission through air because IR moves from object to detector in the air [4]. In reality, the IR radiation is attenuated by the scattering and absorption process by gases molecules. The radiant flux of a heated object is selectively absorbed by the gases constituents of the atmosphere. Water vapor, carbon dioxide, and ozone are the most dominant absorbers for each absorption band. IR radiation in several regions between 1 and 3  $\mu\text{m}$ , and 6.3  $\mu\text{m}$  is absorbed by water vapor. Strong absorption in the neighborhood of 2.6, 4.3, and 15  $\mu\text{m}$  is mainly due to the carbon dioxide. The stretching and bending of chemical bonds that cause a dipole change and absorption of a photon of the same frequency is the principle behind IR spectroscopy, which identifies the absorption frequencies of a molecule at multiple modes of oscillation. It is also based on this concept that IR detectors and telescopes can be selected typically in wavelength regions where the radiation can penetrate and has weak interaction with smog, fog, or dust to significantly increase the visibility of the interested objects.

As a result, strong transmission region of radiant was represented in yellow box where we can obtain IR radiation spectrum. In case of MWIR region, as mentioned at table 1.1, whole MWIR ranges from 3-8 mm can not be detected due to the strong absorption by water vapor. Consequently, detection for MWIR region was restricted to 3-5  $\mu\text{m}$  ranges.

### **1.1.6. Selection of IR wavelength**

There are 5 types of IR ranges as described in Table 1.1. Among them, there are two spectral windows of reasonably high transmission of IR such as mid-wavelength infrared (MWIR) which spans 3~5  $\mu\text{m}$  and the long-wavelength infrared (LWIR) which spans 8~14  $\mu\text{m}$ . IR detection in the LWIR clearly offers a high photon flux, whereas MWIR range provides a better thermal contrast. The strengths and weaknesses of each IR ranges are arranged in Table 1.2.

In this study, MWIR is the main IR range target that I can focus on for the military applications. The MWIR range which is corresponds to the heat of objects with a temperature of around 1000 K is very important IR range to track the missiles and engines of aircraft and tanks

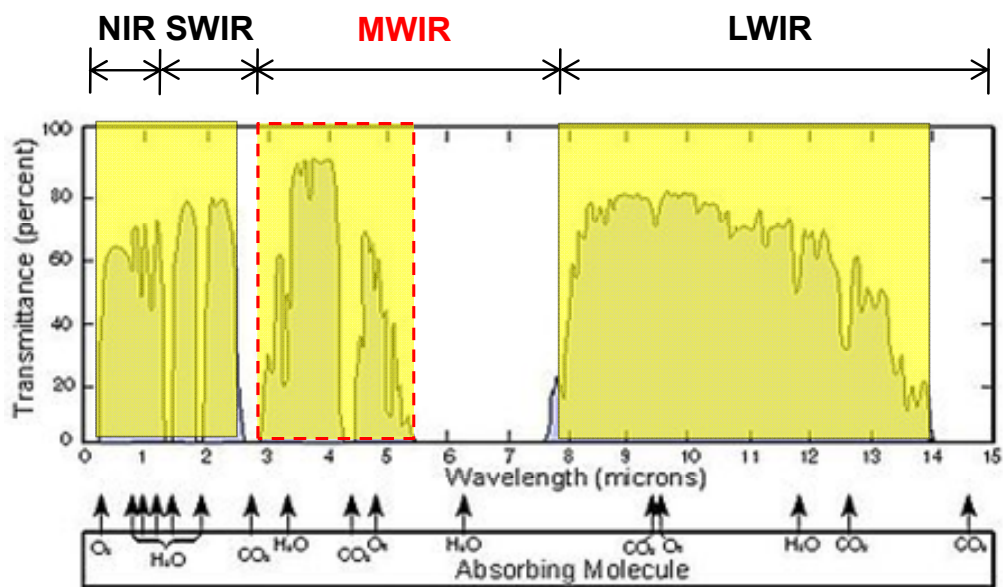


Fig. 1.3. Transmission of the atmosphere for a 6000 ft horizontal path at sea level. Common atmospheric transmission windows are located at 0.7-2  $\mu\text{m}$ , 3-5  $\mu\text{m}$  and 8-12  $\mu\text{m}$ .

	SWIR	MWIR	LWIR
View through smoke	Better than visible	Better than SWIR	Better than MWIR
High humidity	Better than visible	Best: Better than SWIR and LWIR	Moderate
Cold weather night vision	N/A	Moderate	Best
Night vision in total darkness	Poor-relies on nightglow	Excellent	Excellent
View through fog	Better than visible	Better than SWIR	Better than MWIR

Table 1.2. The strength and weakness of IR ranges. Taken from reference [5].

## **1.2. Photo-detection principle and materials for MWIR detection**

In the previous section, I describe that what is the IR and the characteristics of IR. For the IR detection, IR photodiode device is needed. In this section, I will briefly explain the principle of photo-detection and what kinds of materials are suitable for the MWIR detection.

### **1.2.1. Operating principle of photodiodes**

A typical component of an infrared camera system is composed of optics for light collection, IR device, a focal plane array for detecting the IR signal and converting it to an electrical signal, a cooling system for the focal plane array, a read out integrated circuit (ROIC) to collect the electrical signal and perform initial, digital signal processing, and electronic devices for digital display of infrared images. The schematic diagram of IR system is illustrated in Fig. 1.4.

Now, the operating principle of IR photodiode will be described. IR detectors can be received the IR radiation emitted from the objects with a temperature above 0 K. Optics are necessary to focus IR radiation since objects emits IR radiation everywhere. Absorbed the IR with an equal or exceed energy of band gap generate electron-hole pair. They can make an electrical signal induced in the p-n junction which is converted to the digital signal through Si ROIC. We can be observed the objects through display devices even in the dark environments.

The operation theory of p-n junction photodiode is illustrated in Fig. 1.5 (a). IR photons with energy equal or greater than the energy band gap create electron-hole pairs in the vicinity of pn junctions. The generated electron and hole are separated by the strong electric field induced in the depletion width. The minority carrier generated by photon becomes majority carrier on the other side. From this mechanism, photocurrent is generated which shifts the current-voltage curve, as shown in Fig. 1.5 (b), towards negative current direction.

### **1.2.2. Application fields for IR photodiodes**

It is no wonder IR detection has already been spread in wide range applications, including industry, law enforcement, medical, military, astronomy and others fields. An illustration of IR applications is shown in Fig. 1.6. When the IR photodiodes were invented, its application was restricted only to military applications such as aircraft collision/warning, surveillance and missile tracking etc. However, IR detection has been spread to medical, industrial, astronomy, law enforcement and others. They are normally used to measure the temperature of brake linings, power lines, cutting tools, welding and soldering operation and ingots for industrial application. Skin temperature, cancer detection, monitoring of eye movement, CO<sub>2</sub> levels in blood and breath are applications for medical area.

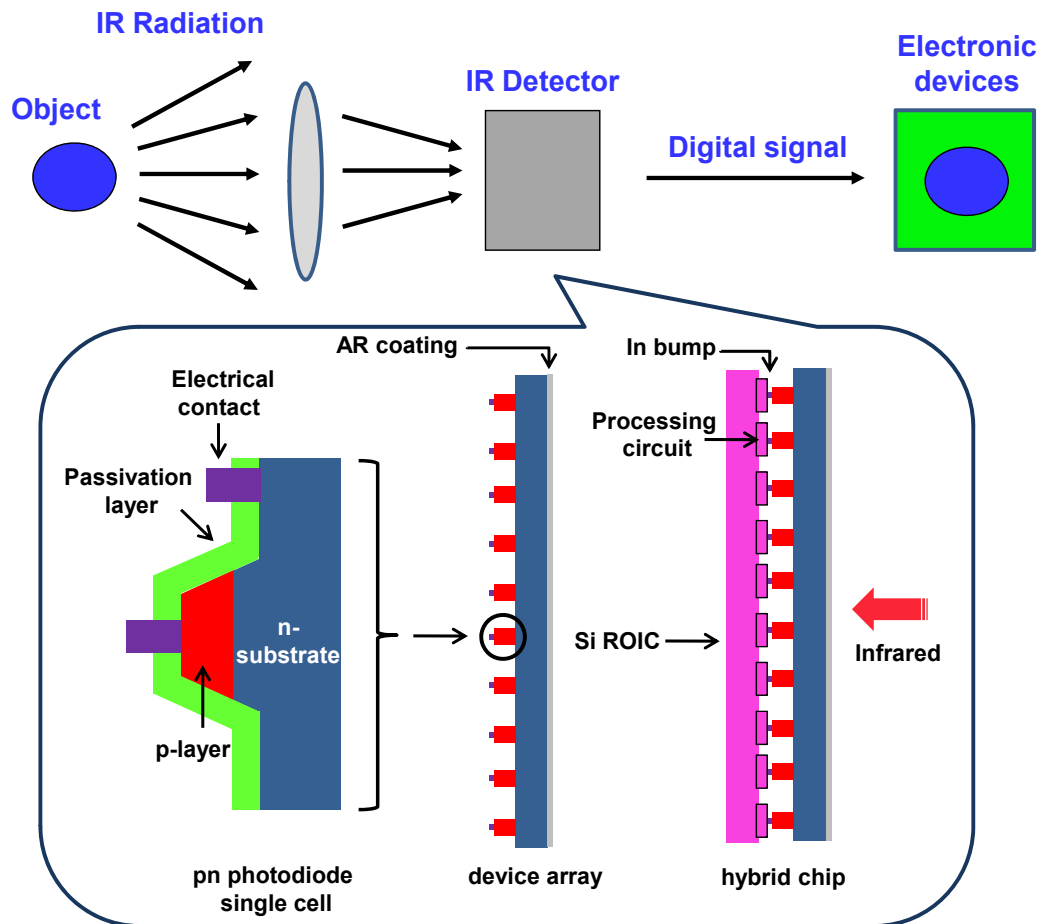


Fig. 1.4. Schematic diagram of an IR photodiode system including its components. More detail structures of IR detector is represented in box below.

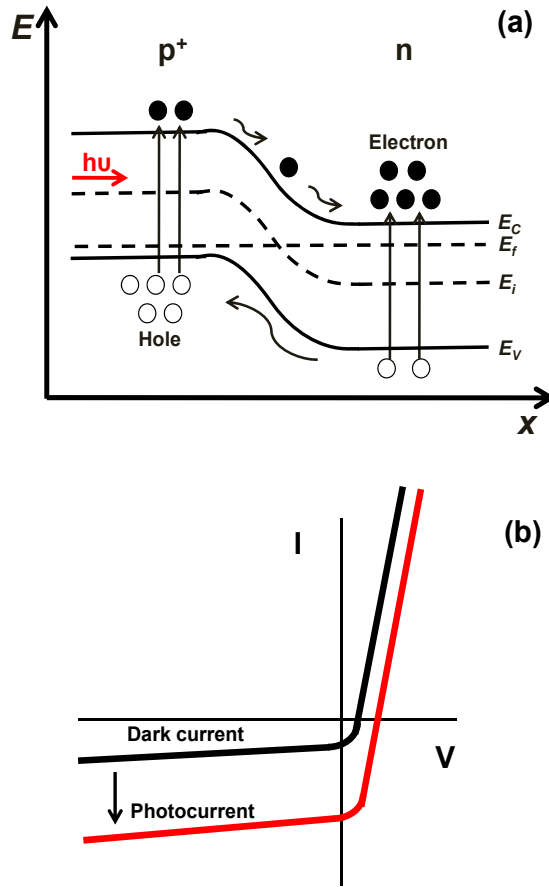


Fig. 1.5. (a) Schematic band diagram of p-n photodiode with electron-hole pair generation. (b) current-voltage characteristics for the illuminated and non illuminated photodiodes.

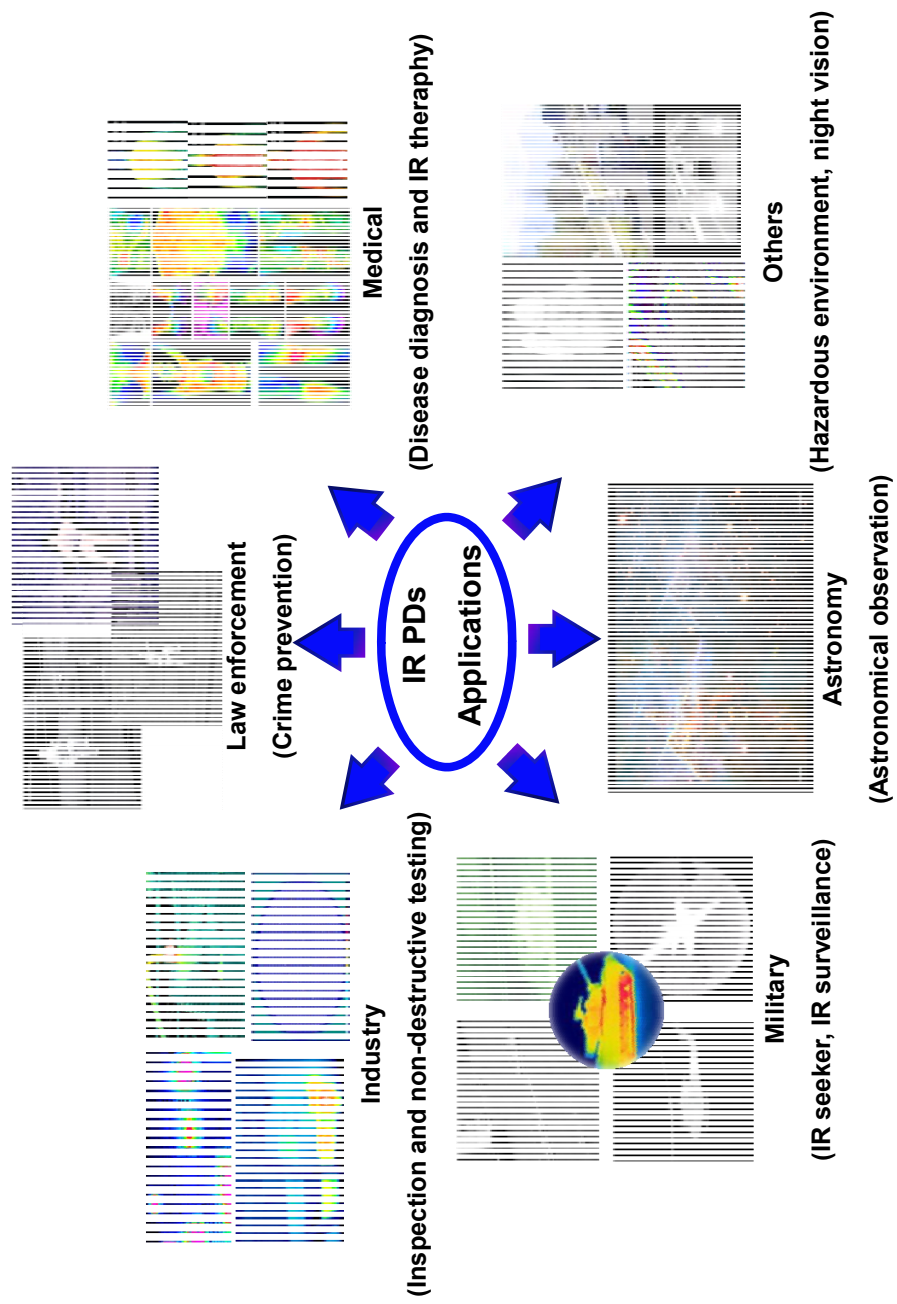


Fig. 1.6. Illustration of the various applications for IR detection

### 1.2.3. Materials for MWIR detection

In the range of 3-5  $\mu\text{m}$  for MWIR detection, materials with band gap energy is well matched to its wavelength should be selected. The band gap energy of MWIR was represented in the gray region in the plot of band gap energy versus lattice constant as shown in Fig. 1.7. Two types of materials systems can be selected as a possible material for MWIR detection.

The first one is mercury cadmium telluride ( $\text{Hg}_{1-x}\text{Cd}_x\text{Te}$  - MCT), the ternary alloy as a mixture of CdTe and HgTe as represented with red circles in Fig. 1.7.  $\text{Hg}_{1-x}\text{Cd}_x\text{Te}$  was first synthesized in 1958 by a Lawson at the Royal Radar Establishment in England [6]. From the development, it becomes an attractive material due to the direct band gap, intrinsic semiconductor for the LWIR spectral region. Advancement of the crystal growth technology has proceeded deliberately and steadily for four decades in spite of the high vapor pressure of Mercury (Hg) at the melting point of HgCdTe and the known toxicity of the materials. HgCdTe has several properties to qualify it as highly useful material for IR detection such as the tenability of the band gap from 0.7 to 25  $\mu\text{m}$ , direct band gap with high absorption coefficient, moderate dielectric constant/index of refraction and availability of wide band gap lattice-matched substrates for the epitaxial growth. The band gap of HgCdTe is a function of the alloy composition of Cd and the temperature of material as expressed in eq. 1-5 which is developed by G. L. Hansen *et. al.*, [7].

$$E_g = -0.302 + 1.93x - 0.81x^2 + 0.832x^3 + 5.35(1 - 2x)10^{-4}T \quad [\text{eq-1.5}]$$

where,  $x$  is composition of Cd and  $T$  is the temperature. With increasing composition of Cd contents, the band gap span from the long to mid wavelength regions. At higher values of Cd composition, the band gap can be increased corresponding to the wavelength as short as  $0.7 \mu\text{m}$ . Direct band-gap semiconductor have a sharp optical absorption as the photon energy increase above energy band-gap in contrast to the indirect semiconductors such as Si, and Ge. As a result, strong optical absorption is possible, making it to required minimized HgCdTe thickness. It helps to minimize the volume of material which can generate noise, thermal excess carrier in the diffusion limited operation mode. However, MgCdTe alloys posses some serious drawbacks such as (i) a sensitive dependence of the energy gap on the alloy composition ratio, requiring a precise control over the growth temperature during the growth (ii) large non-uniformity over larger area due to high vapor pressure of Hg, causing high dark current in MCT devices (iii) large tunneling current due to low electron effective mass. Some physical properties of HgCdTe is represented in Table 1.3.

Another material for the MWIR detection is an InSb. It has also direct and small energy band gap among III-V semiconductor whose properties was firstly observed by H. Welker in 1952 [8]. Since then, many researchers have focus on the scientific investigation of InSb. As the InSb is a direct semiconductor, conduction band minimum and valence band maximum is located at the same  $k$  vales ( $k=0$  in E-K diagram), making it possible to fabricate high quantum efficient device. Since its band gap energy is the

smallest values known at that time, its application is, no doubtably, focused on the Infrared detector. The band gap of 0.18 eV at room temperature indicates that it corresponds to the wavelength of 7  $\mu\text{m}$ , whereas it is increased up to 0.24 eV when it is cooled at liquid nitrogen. This band gap enables to cover MWIR ranges up to 5.5  $\mu\text{m}$ . The most interesting features of InSb come not only from the smallest band gap but also high quality single crystal preparation due to the congruent melting point at 525.7  $^{\circ}\text{C}$ , enabling it to be grown from melt by conventional crystal growth as represented in Fig. 1.8 [9]. These days, a fabrication of 3 inch and even larger sized InSb wafer is available in the industry, which is the attractive prospect for focal plan array fabrication. The physical properties such as lattice constant, band gap energy, electron and hole mass, refractive index, and thermal expansion coefficient are summarized in Table 1.3.

Based on the comparison between  $\text{Hg}_{1-x}\text{Cd}_x\text{Te}$  and InSb above, I conclude that InSb is more suitable material for high performance MWIR photodetector with low price. InSb is chosen for this research.

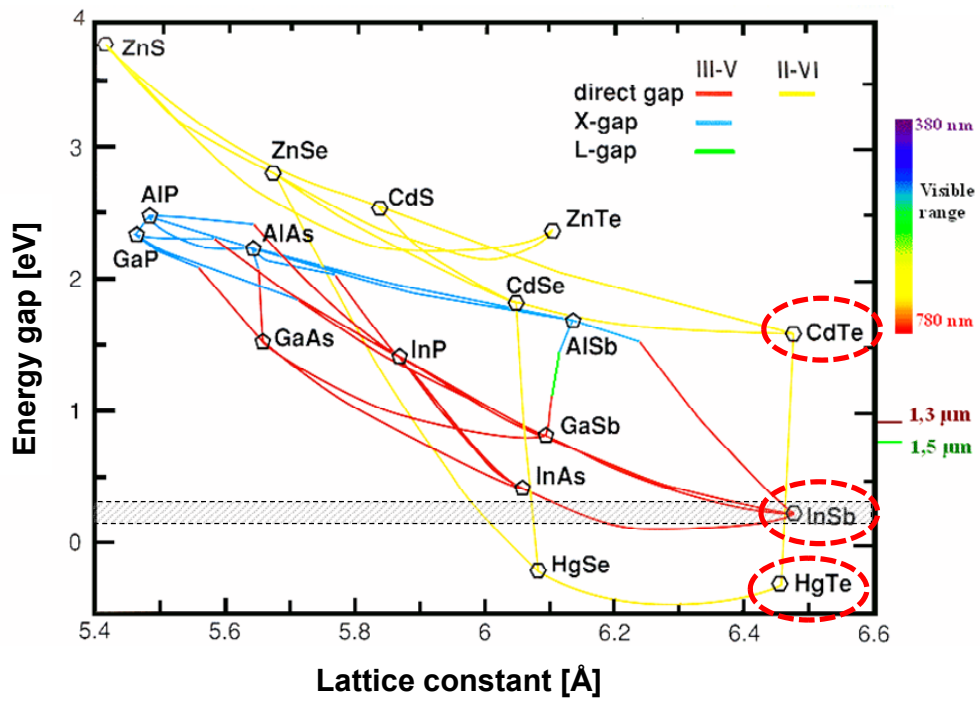


Fig. 1.7. A plot of band gap energy versus lattice constant

	T(K)	Hg <sub>0.775</sub> Cd <sub>0.225</sub> Te [10]	InSb [11]
Lattice structure		Zincblende	Zincblende
Lattice constant (Å)	300	6.464	6.478
Thermal expansion coefficient (10 <sup>-6</sup> K <sup>-1</sup> )	300 77		5.04 6.50
Melting point (°C)			525.7
Energy gap (eV)	300 77	0.123	0.180 0.228
m <sub>e</sub> <sup>*</sup> /m <sub>0</sub>	300 77	0.007	0.0116
m <sub>h</sub> <sup>*</sup> /m <sub>0</sub>	300		0.41
Electron mobility (cm <sup>2</sup> /Vs)	300 77	1.0 x 10 <sup>5</sup>	8 x 10 <sup>4</sup> 10 <sup>6</sup>
Hole mobility (cm <sup>2</sup> /Vs)	300 77	450	800 10 <sup>4</sup>
Refractive index			3.96
Intrinsic carrier concentration (cm <sup>-3</sup> )	300 77	6.3 x 10 <sup>12</sup>	4.1 x 10 <sup>16</sup> 2.6 x 10 <sup>9</sup>

Table 1.3. Physical properties of HgCdTe and InSb

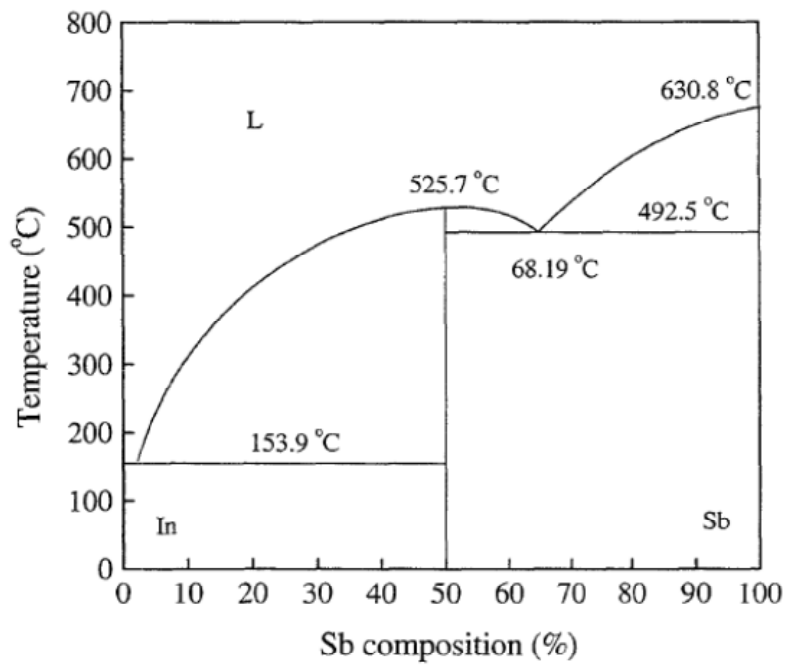


Fig. 1.8. Temperature–composition binary phase diagram of In and Sb, describing the equilibrium of solid with a liquid of InSb [9]

### **1.3. A survey of previous researches for InSb MWIR photodiodes**

In this section, I describe two ways to fabricate MWIR device including an ion implantation and crystal growth. In case of ion implantation, low temperature process, direct control of junction depth formation, and high uniformity process are possible. On the other hand, ion implantation has disadvantages such as shallow depth up to 1  $\mu\text{m}$  and surface damage region formation which is the main drawback of ion implantation. In the crystal growth method, multilayer can be grown during crystal growth and junction depth is controlled by changing the growth time or source mole fractions. The most striking advantage is no surface damage. Thin films can be grown layer by layer on the lattice matched substrate or lattice mismatched substrate by inserting buffer layer or some dots to reduce the stress induced by the lattice mismatch. As the source is sometimes very toxic, flammable and corrosive, special equipment and caution has to be needed for the safety.

#### **1.3.1. Previous research of MWIR photodiode fabricated by diffusion and ion implantation**

Initially pn junctions in InSb were made by diffusing Zinc (Zn) [12, 13] or Cadmium (Cd) [14] into n-type substrates with net donor concentration in the range of  $10^{14}\sim 10^{15}\text{ cm}^{-3}$  at 77 K. It was found, however, by several researcher that Zn and Cd produce a porous surface that is difficult to remove [15]. To circumvent this surface problem and to make high quality p-n

junctions, ion implantation into n-type InSb substrate can be conducted with light ions such as Proton and Magnesium (Mg) [16-22]. Heavy atoms such as Mg appears that InSb can be made amorphous [21] and produce surface damage [23, 24] by implanting it at room temperature. Zn and Cd may be too heavy to implant in InSb. As a result, beryllium (Be) was applied as a p-type dopant into InSb substrate. However, it was reported that Be out-diffusion problem was generated near implanted InSb surface during RTA process [25]. RTA process was inevitable step to remove surface damages after ion implantation. However, Be was out diffused due to the non-stoichiometry at the InSb surfaces.

In conclusions, ion implantation process produce surface damage inevitably even though light ion of Be is used. In order to remove surface damage, post annealing treatment has to be made at a high temperature, producing other problems such as dopant diffusion and Sb evaporation near surface to make an Sb vacancy ( $V_{Sb}$ ).

### **1.3.2. Previous research of MWIR photodiode fabricated by crystal growth techniques**

A crystal growth of InSb has extensively researched by metalorganic chemical vapor deposition (MOCVD). Since it is reported that there is a stable hydride group V source such as arsine ( $AsH_3$ ) and phosphine ( $PH_3$ ) for As and P based III-V semiconductor growth. Hydride group V source is very beneficial to remove native oxides during in-situ thermal cleaning and to reduce the carbon contents in the epitaxial layers. There is an only one gas

source of antimony. O. Sugiura *et. al.*, of Tokyo Institute of Technology have grown InSb on InSb substrate using triethylindium (TEIn) and stibine (SbH<sub>3</sub>) as a indium and antimony source, respectively [26]. They used the SbH<sub>3</sub> gas source instead of metalorganic antimony source for the first time. The optimum growth conditions for InSb homoepitaxial growth is at 490 °C under V/III ration of 8. At low V/III ratio, Indium droplets were formed on the surface. The InSb epitaxial layer was n-type with a carrier density and mobility of  $1.5 \times 10^{16} \text{ cm}^{-3}$  and  $7.6 \times 10^4 \text{ cm}^2/\text{Vs}$  (measured at 77 K), respectively. Even at 300 °C, single crystal of InSb layer can be grown by inserting a buffer layer grown at 400 °C. The growth rate at 400 °C increased in proportional to the TEIn flow rate, but independent of the SbH<sub>3</sub>. P. K. Chiang *et. al.*, of North Carolina State University reported the MOCVD grown InSb using TEIn and trimethylantimony (TMSb) [27]. In this experiment, high quality of InSb can be grown even though TMSb overpressure was not maintained during the *in-situ* thermal cleaning process. An excellent surface morphology was achieved on InSb (100) substrates. The growth rate is dependent on both the TMSb flow rate with a constant TEIn flow rate and growth temperature. Electrical properties of InSb grown on semi-insulating GaAs substrate with the same growth condition of InSb homoepitaxial growth were measured. A carrier concentration and electron mobility measured at 300 K are  $2.0 \times 10^{16} \text{ cm}^{-3}$  and  $40,000 \text{ cm}^2/\text{Vs}$ , respectively (thickness= 1 $\mu\text{m}$ ). With dependence of Hall measurements, mobility tents towards a maximum value in the vicinity of 300 K and decrease monotonically with increasing temperature, explaining the presence of high dislocation density in the InSb epilayer on GaAs substrates. O. Sugiura *et. al.*, at Tokyo Institute of Technology used vacuum MOCVD to

growth InSb using TEIn and TMSb as a indium and antimony source, respectively [28]. P-type conductivity of InSb grown at 400 °C has been reported. From the capacitance-voltage measurements (C-V), the impurity density near surface was  $2 \times 10^{15} \text{ cm}^{-3}$ . Average hole density and mobility evaluated from the Van der Pauw method at 77 K were  $2 \times 10^{17} \text{ cm}^{-3}$  and  $4 \times 10^3 \text{ cm}^2/\text{Vs}$ , respectively. There is an inconsistency between two methods, indicating that there is a highly conductive p-region near the epilayer. The work of D. K. Gaskill *et. al.*, reported the highest quality of InSb epitaxial layer grown by MOCVD [29]. An intentionally doped InSb layer has a n-type carrier concentration and mobility of  $1.4 \times 10^{15} \text{ cm}^{-3}$  and  $2.53 \times 10^5 \text{ cm}^2/\text{Vs}$ , which was measured at 77 K. this mobility value is equal or exceeds the best ALE values reported at the time of reports [30]. For the transport measurements, p-type InSb substrates with resistivity of 50-100  $\Omega\text{cm}$  were used. Double crystal x-ray diffractometry of InSb grown at 450 °C yields a full width at half maximum (FWHM) of 13 arcsec. Y. H. Choi *et. al.*, of Northwestern University reported the crystal quality of InSb grown on InSb, GaAs and GaAs coated on Si substrates [11, 31, 32]. As shown in Fig. 1.9, the film grown on InSb had x-ray FWHM of 14 arcsec while those grown on GaAs and GaAs coated on Si substrate exhibited FWHM of 171 and 361 arcsec, respectively. The broader peaks on GaAs and Si substrates are due to higher dislocation density generated at the epilayer/substrate interface. Crystal quality is dependence on the film thickness when the InSb is grown on lattice mismatched substrates. The FWHM of InSb grown on both substrates decrease with increasing film thickness, indicating improved crystalline quality away from the highly mismatched epilayer substrate interface. The electrical properties of the epilayers were investigated through

Hall measurements using Van der Pauw method. The Hall mobility of InSb grown on GaAs substrates is found to improve with increasing thickness, reflecting the decrease of dislocation density away from the interface. InSb epilayer showed n-type characteristics with a carrier concentration of  $1 \times 10^{16} \text{ cm}^{-3}$  at 300 K. The work of Noreika *et. al.*, was one of the pioneering research works conducted with InSb [32]. Measurements of the surface residence lifetime of Sb on InSb defined the substrate temperature ranges in which it could be grown. Epitaxial layers were grown on (111)A, (111)B, and (001) InSb substrates with corresponding reconstruction temperature and data. Data was collected to physically represent an effective vapor pressure of Sb over InSb required to sustain a particular surface reconstruction. R. M. Biefeld *et. al.*, researched the InSb epitaxial growth extensively using MOCVD [33]. InSb growth mechanism was researched using TMIn and TMSb sources. The growth rate is directly dependence on the TMIn flow rate which has also found for the growth of a variety of other III-V materials including GaAs and GaP [34, 35]. At the InSb growth temperature between 450 to 500 °C, the vapor pressure of Sb is about two orders of magnitude greater than that of In, so that, in the presence of excess Sb, any In atoms which strike the substrate will stick to the surface and react to form InSb [36, 37]. If the vapor pressure of Sb in the reactor exceeds that of the equilibrium vapor press for solid Sb, elemental Sb will be deposited on the substrate surface. As illustrated in Fig. 1.10, the growth efficiency for InSb is thermally activated with higher growth efficiencies at higher temperatures. The growth of InSb between 400 and 500 °C appears to be dominated by reaction kinetics. This effect was also found in P. K. Chiang's reports [27]. The rate limiting step in the growth of InSb is probably due to the incomplete

pyrolysis of TMSb. TMSb has been found to be only partially decomposed below 500 °C [38, 39]. He also explained the origin of surface roughness. When the V/III ration and growth temperature exceed the optimum conditions, rough surface morphology was observed. This surface roughness can be explained by a combination of factors which include preferential nucleation, surface diffusion, substrate preparation, substrate defects, vapor phase composition, and surface reaction. If preferential nucleation takes place on the surface and surface diffusion is too slow in comparison to the growth rate to allow for the migration of atoms to fill in the remaining surface sites, then hillock formation will take place. Hillock formation will occur when either the growth temperature is too low which will result in slow surface diffusion or the growth rate is too high. Preferential nucleation often results from the presence of defects or impurities on the substrate and also from substrate orientation [40]. When the temperature is so low that the metalorganics and/or the hydride do not decompose on the surface of the substrate, then an imbalance of the reactants can occur on the surface. In the case of InSb, an excess of In causes alloying on the surface and the formation of droplets of In rich materials. An excess of Sb results in the formation of Sb hillock. A smooth surface morphology of epitaxial layer can be obtain when the temperature is high enough for decomposition of the reactants, and the growth rate is low enough for a specific temperature. It is reported that trimethlyantimony (TMSb) source is not completely decomposed in the InSb growth temperature region [38, 39]. Trisdimethylaminoantimony (TDMASb) [41], triisopropyl-antimony (TIPSb) [42-45], diisopropylantimonyhydride (DIPSbH) [46] and tertiarybutyldimethylantimony (TBDMSb) [42, 45] have been adapted for the InSb epitaxial growth as an alternative antimony source.

These sources have been used to reduce carbon impurity level in the epilayers, if present, by the elimination of methyl groups. Carbon makes an important role in InSb as a possible intrinsic p-type defect. As a result, electronic properties have been improved.

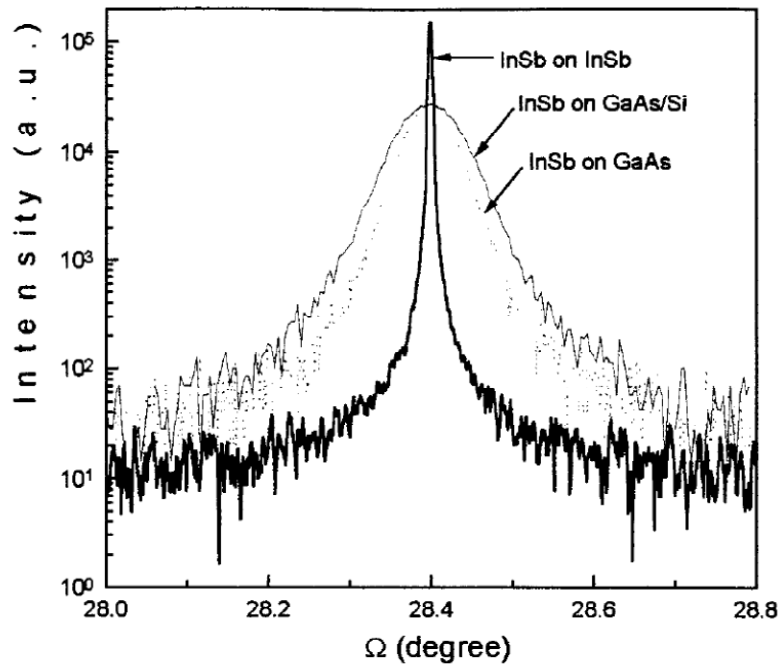


Fig. 1.9. X-ray diffraction spectra of 3.0  $\mu\text{m}$  thick InSb films grown on InSb, GaAs and GaAs coated Si substrates

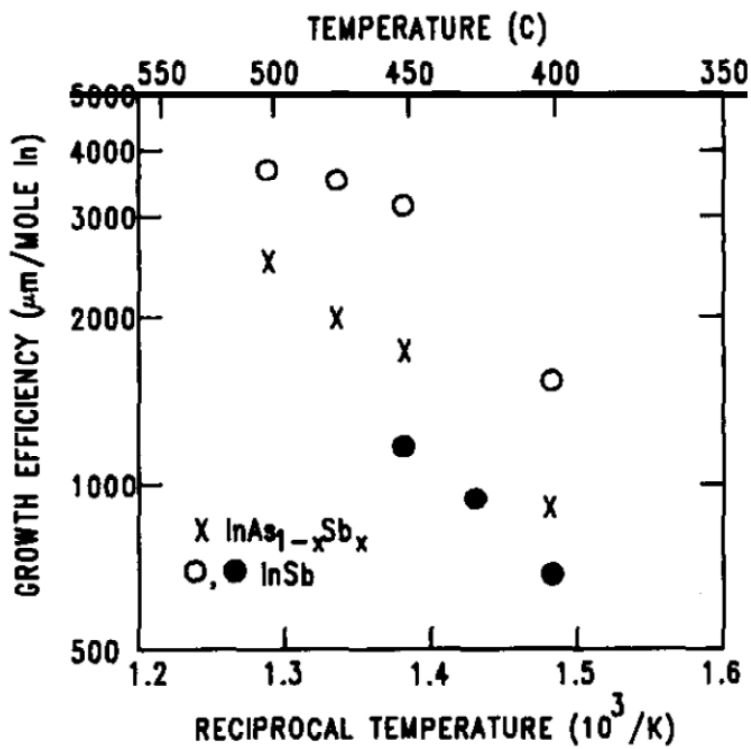


Fig. 1.10. Growth efficiency of  $\text{InAs}_{1-x}\text{Sb}_x$  and  $\text{InSb}$  versus reciprocal temperature. This semi-log plot indicates that the growth rate is thermally activated for both materials. The filled circles are data for  $\text{InSb}$  from P. K. Chiang [27].

## 1.4. Organization of this thesis

As we discussed above, the major purpose of this dissertation is to grow high quality of InSb epitaxial layers by changing growth parameters, mainly growth temperature and V/III ratio, instead of the p-n photodiodes fabrication using diffusion and ion implantation process. So, this dissertation is focused on the high quality of InSb epitaxial growth using LP-MOCVD and the improvement of subsequent p-n photodiode performance by implementation of the ZnS passivation. This dissertation covers three topics.

The most important prerequisite for the high quality epitaxial layers is how to prepare an epi-ready substrate where epitaxial layers can be grown on. Due to the stable native oxides of InSb, *ex-situ* wet cleaning process was adopted before inserting the substrate into the chamber. *in-situ* thermal cleaning process was investigated in order to well prepared InSb substrates before epitaxy. With or without trimethylantimony (TMSb) has important role to prepare the substrates and the effects of with or without TMSb overpressure on the InSb substrate were analyzed in chapter 3.

In chapter 4, InSb epitaxial layers were grown on InSb substrates by changing growth parameters such as growth temperature and V/III ration to obtain optimized growth conditions. The effects of growth parameters on the quality of InSb epilayers were investigated and growth behavior of InSb was represented. For the use of opto-electronic devices, optical quality of InSb was systematically investigated using PL measurements. The origin of PL

peak was analyzed. In this chapter, p-type doping study for p-n junction formation was researched using diethylzinc.

In chapter 5, I developed the new passivation materials for InSb photodiodes. The origin of surface state will be explained as well as the mechanism of the reduction of surface state after depositing ZnS passivant will be explored.

Finally conclusion of this dissertation will be presented in chapter 6.

## 1.5. Bibliography

- [1] W. Herschel, "Investigation of the Powers of the Prismatic Colours to Heat and Illuminate Objects; With Remarks, That Prove the Different Refrangibility of Radiant Heat. To Which is Added, an Inquiry into the Method of Viewing the Sun Advantageously, with Telescopes of Large Apertures and High Magnifying Powers. By William Herschel, LL. DFRS," *Philosophical Transactions of the Royal Society of London*, vol. 90, pp. 255-283, 1800.
- [2] E. S. Barr, "Historical survey of the early development of the infrared spectral region," *American Journal of physics*, vol. 28, pp. 42-54, 1960.
- [3] S. P. Langley, "The bolometer and radiant energy," in *Proceedings of the American Academy of Arts and Sciences*, 1880, pp. 342-358.
- [4] A. Rogalski and K. Chrzanowski, "Infrared devices and techniques," *Optoelectronics Review*, pp. 111-136, 2002.
- [5] J. L. Miller, "Future sensor system needs for staring arrays," *Infrared Physics & Technology*, vol. 54, pp. 164-169, 2011.
- [6] W. Lawson, S. Nielsen, E. Putley, and A. Young, "Preparation and properties of HgTe and mixed crystals of HgTe-CdTe," *Journal of Physics and Chemistry of Solids*, vol. 9, pp. 325-329, 1959.
- [7] G. Hansen, J. Schmit, and T. Casselman, "Energy gap versus alloy composition and temperature in  $\text{Hg}_{1-x}\text{Cd}_x\text{Te}$ ," *Journal of Applied Physics*, vol. 53, pp. 7099-7101, 1982.
- [8] H. Welker, "Über neue halbleitende Verbindungen," *Zeitschrift für Naturforschung A*, vol. 7, pp. 744-749, 1952.

- [9] T. B. Massalski, H. Okamoto, P. Subramanian, L. Kacprzak, and W. W. Scott, *Binary alloy phase diagrams* vol. 1: American Society for Metals Metals Park, OH, 1986.
- [10] A. Rogalski, "HgCdTe infrared detector material: history, status and outlook," *Reports on Progress in Physics*, vol. 68, p. 2267, 2005.
- [11] M. Razeghi, "Overview of antimonide based III-V semiconductor epitaxial layers and their applications at the center for quantum devices," *The European Physical Journal Applied Physics*, vol. 23, pp. 149-205, 2003.
- [12] K. Nishitani, K. Nagahama, and T. Murotani, "Extremely reproducible zinc diffusion into InSb and its application to infrared detector array," *Journal of Electronic Materials*, vol. 12, pp. 125-141, 1983.
- [13] K. Nishitani, K. Nagahama, and T. Murotani, "Zinc diffusion into InSb," *Japanese journal of applied physics*, vol. 22, p. 836, 1983.
- [14] P. Catagnus, C. Polansky, and J. Spratt, "Diffusion of cadmium into InSb," *Solid-State Electronics*, vol. 16, pp. 633-635, 1973.
- [15] C. Hurwitz and J. Donnelly, "Planar InSb photodiodes fabricated by Be and Mg ion implantation," *Solid-State Electronics*, vol. 18, pp. 753-756, 1975.
- [16] A. Foyt, W. Lindley, and J. Donnelly, "n-p Junction photodetectors in InSb fabricated by proton bombardment," *Applied Physics Letters*, vol. 16, pp. 335-337, 1970.
- [17] P. McNally, "Ion implantation in InAs and InSb," *Radiation Effects*, vol. 6, pp. 149-153, 1970.

- [18] R. Thom, T. Koch, J. Langan, and W. Parrish, "A fully monolithic InSb infrared CCD array," *Electron Devices, IEEE Transactions on*, vol. 27, pp. 160-170, 1980.
- [19] C.-Y. Wei, K. Wang, E. Taft, J. Swab, M. Gibbons, W. Davern, *et al.*, "Technology development for InSb infrared imagers," *Electron Devices, IEEE Transactions on*, vol. 27, pp. 170-175, 1980.
- [20] J. Rosbeck, I. Kasai, R. Hoendervoogt, and M. Lanir, "High performance Be<sup>+</sup> implanted InSb photodiodes," in *Electron Devices Meeting, 1981 International*, 1981, pp. 161-164.
- [21] J. Donnelly, "The electrical characteristics of ion implanted compound semiconductors," *Nuclear Instruments and Methods*, vol. 182, pp. 553-571, 1981.
- [22] H. Fujisada and T. Sasase, "Effects of Insulated Gate on Ion Implanted InSb p<sup>+</sup> n Junctions," *Japanese Journal of Applied Physics*, vol. 23, p. L162, 1984.
- [23] H. Betz, K. Wiedeburg, H. Ryssel, and H. Kranz, "Ion implanted InSb photodetectors," in *Electron Devices Meeting, 1977 International*, 1977, pp. 551-554.
- [24] G. Destefanis and J. Gailliard, "Very efficient void formation in ion implanted InSb," *Applied Physics Letters*, vol. 36, pp. 40-42, 1980.
- [25] J. Liu and T. Zhang, "Rapid thermal annealing characteristics of Be implanted into InSb," *Applied surface science*, vol. 126, pp. 231-234, 1998.
- [26] O. Sugiura, H. Kameda, K. Shiina, and M. Matsumura, "Low-temperature growth of InSb by vacuum MOCVD using TEIn and SbH<sub>3</sub>," *Journal of electronic materials*, vol. 17, pp. 11-14, 1988.

- [27] P. Chiang and S. Bedair, "Growth of InSb and InAs $_{1-x}$ Sb $_x$  by OM-CVD," *Journal of The Electrochemical Society*, vol. 131, pp. 2422-2426, 1984.
- [28] O. Sugiura and M. Matsumura, "Homoepitaxial growth of InSb by vacuum metal-organic chemical vapor deposition," *Japanese journal of applied physics*, vol. 24, p. L925, 1985.
- [29] D. Gaskill, G. Stauf, and N. Bottka, "High-mobility InSb grown by organometallic vapor phase epitaxy," *Applied physics letters*, vol. 58, pp. 1905-1907, 1991.
- [30] P. Thompson, J. Davis, J. Waterman, R. Wagner, D. Gammon, D. Gaskill, *et al.*, "Use of atomic layer epitaxy buffer for the growth of InSb on GaAs by molecular beam epitaxy," *Journal of applied physics*, vol. 69, pp. 7166-7172, 1991.
- [31] Y. Choi, R. Sudharsanan, C. Besikci, E. Bigan, and M. Razeghi, "High-Quality InSb Growth on GaAs and Si by Low-Pressure Metalorganic Chemical Vapor Deposition," in *MRS Proceedings*, 1992, p. 375.
- [32] A. Noreika, M. Francombe, and C. Wood, "Growth of Sb and InSb by molecular-beam epitaxy," *Journal of Applied Physics*, vol. 52, pp. 7416-7420, 1981.
- [33] R. M. Biefeld, "The preparation of InSb and InAs  $1-x$  Sb  $x$  by metalorganic chemical vapor deposition," *Journal of Crystal growth*, vol. 75, pp. 255-263, 1986.
- [34] R. M. Biefeld, "The preparation of device quality gallium phosphide by metal organic chemical vapor deposition," *Journal of Crystal*

- Growth*, vol. 56, pp. 382-388, 1982.
- [35] G. Stringfellow, "A critical appraisal of growth mechanisms in MOVPE," *Journal of Crystal Growth*, vol. 68, pp. 111-122, 1984.
- [36] R. Hultgren, P. D. Desai, D. T. Hawkins, M. Gleiser, and K. K. Kelley, "Selected values of the thermodynamic properties of the elements," DTIC Document 1973.
- [37] N. Sirota, R. Willardson, and A. Beer, "Semiconductors and Semimetals, Vol," ed: 4 Academic Press, New York, 1968.
- [38] C. Larsen, S. Li, and G. Stringfellow, "Decomposition mechanisms of trimethylantimony and reactions with trimethylindium," *Chemistry of Materials*, vol. 3, pp. 39-44, 1991.
- [39] G. B. Stringfellow, *Organometallic vapor-phase epitaxy: theory and practice*: Academic Press, 1999.
- [40] H. Mori and S. Takagishi, "Morphology of GaAs epitaxial layers grown by MOCVD," *Journal of crystal growth*, vol. 69, pp. 23-28, 1984.
- [41] K. Baucom and R. Biefeld, "Growth of InSb using tris (dimethylamino) antimony and trimethylindium," *Applied physics letters*, vol. 64, pp. 3021-3023, 1994.
- [42] R. Biefeld and R. Gedridge, "The growth of InSb using triisopropylantimony or tertiarybutyldimethylantimony and trimethylindium," *Journal of crystal growth*, vol. 124, pp. 150-157, 1992.
- [43] G. Stauf, D. Gaskill, N. Bottka, and R. Gedridge Jr, "Low-temperature organometallic vapor phase epitaxy of InSb using

- the novel Sb precursor triisopropylantimony," *Applied physics letters*, vol. 58, pp. 1311-1313, 1991.
- [44] C. Chen, Z. Fang, G. Stringfellow, and R. Gedridge Jr, "Triisopropylantimony for organometallic vapor phase epitaxial growth of GaSb and InSb," *Applied physics letters*, vol. 58, pp. 2532-2534, 1991.
- [45] C. Chen, G. Stringfellow, D. Gordon, D. Brown, and B. Vaartstra, "Tertiarybutyldimethylantimony: A new Sb source for low-temperature organometallic vapor phase epitaxial growth of InSb," *Applied physics letters*, vol. 61, pp. 204-206, 1992.
- [46] J. Shin, K. Chiu, G. Stringfellow, and R. W. Gedridge, "Diisopropylantimonyhydride (DIPSbH) for low temperature epitaxial growth of InSb," *Journal of crystal growth*, vol. 132, pp. 371-376, 1993.

## **Chapter 2. Experimental methods: material growth, device fabrication and characterization tools**

### **2.1. Material growth system: Low-Pressure Metalorganic Chemical Vapor Deposition (LP-MOCVD)**

In order to growth InSb epitaxial layers, home-made low pressure metalorganic chemical vapor deposition (LP-MOCVD) are used. The schematic diagram of MOCVD is illustrated in Fig. 2.1. The MOCVD system is composed of four parts: gas delivery part, reactor (growth chamber), pressure control part, and exhaust part.

#### **2.1.1 LP-MOCVD system @SNU**

In order to growth InSb epitaxial layers, home-made low pressure metalorganic chemical vapor deposition (LP-MOCVD) are used. The schematic diagram of MOCVD is illustrated in Fig. 2.1. The MOCVD system is composed of four parts: gas delivery part, reactor (growth chamber), pressure control part, and exhaust part.

##### **Gas delivery part**

In MOCVD system, the gas delivery part is an important part. In this part,

metalorganic (MO) source materials can be metered by a mass flow controller (MFC) and be mixed prior to reaching the growth chamber. The gas mixing line is made of stainless steel with clean, leak-free conditions. 8 sources including 3 gas source and 8 MO source are connected in this system. Each source line equipped with MFC. All MO source are contained in the stainless steel bubblers. The carrier gas for the MO source transports is H<sub>2</sub> gas which is supplied from the Inter-university Semiconductor Research Center (ISRC) at Seoul National University. H<sub>2</sub> gas is purified for the safety. The carrier gas is controlled by the MFC and it can flow through the by-pass line when the source is not used.

### **Reactor system**

In my MOCVD system, reactor is a horizontal type, cold wall, and low pressure. The horizontal reactor is made of quartz which is high purity, optical transparency and low electrical conductivity. This type of reactor is preferred to obtain a more laminar gas flow since gas flow is parallel to the substrate surface. The cold wall type of reactor have an advantages in minimizing contamination from the growth chamber walls during the growth and reducing the possibility of premature source decomposition and/or chemical reactions between source materials. The low pressure system provides the reduction of parasitic reaction in the gas phase, resulting in the increment of growth efficiency, the compositional homogeneity, the improvement interface quality, and the reduced impurity level. Low pressure increase the rapid transport of source materials in the gas phase which decrease the contact time between source atoms. SiC coated graphite is used as a susceptor. This is the rectangular shape including sample loading area up

to 2 inch. The susceptor is heated by RF induction at a frequency of 30 KHz with a maximum power of 7.5 kW. The induction coil is surrounded around growth chamber and is used to heat the graphite susceptor. The thermocouple is used to monitor the susceptor temperature as well as to provide its temperature information to the temperature controller. Pyrometer is equipped for the temperature comparison. The real temperature of growth chamber is calibrated by melting of InSb substrate. Since InSb is melt at 525.7 °C, the point of InSb melting is observed by varying temperature of chamber.

#### **Pressure control parts (Pump)**

The outlet–end of the reactor is linked to the heat exchanger where water is circulating to decrease the temperature of gases. During decreasing temperature, some particles in the gas stick to the heat exchanger so maintenance is needed to remove particles. Low temperature gases containing particles move to the pall filter where the residual particles are removed through passing it. Chamber pressure is controlled by the rotary pump and maintaining the fixed pressure during epitaxial growth is possible by using a throttle valve.

#### **Exhaust system**

The exhaust system is installed at the end of the MOCVD system. Gas exhausted through a scrubber, where the un-reacted source gases are filtered and reacted into stable species.



### 2.1.2 Metalorganic (MO) source materials

Two types of gas and three types of MO source are used for the epitaxial growth in this study. The nitrogen (N<sub>2</sub>) is supplied from the ISRC. The purpose of N<sub>2</sub> is to purge the gas line and reactor before the growth to eliminate any air in the chamber and after growth to eliminate any H<sub>2</sub> or MO sources before opening the chamber. As mentioned above, the carrier gas used in this system is hydrogen gas (H<sub>2</sub>) supplied from ISRC. It is purified by the heated getter gas purifier produced by MONO TORR. Impurities such as H<sub>2</sub>O, O<sub>2</sub>, CO, CO<sub>2</sub> and N<sub>2</sub> contained in H<sub>2</sub> gas can be removed less than 1 ppb by passing the zirconium alloy. Getter bed is maintained at the temperature of 400 °C

The group III source is electronic grade metalorganic compounds supplied by the Rohm & Hass. The indium source is trimethylindium (TMIn), [(CH<sub>3</sub>)<sub>3</sub>In]. TMIn is a volatile solid at ambient conditions. The vapor pressure of TMIn as a function of temperature is given by eq. 2-1.

$$\log_{10} P(TMIn) = 10.52 - \frac{3014}{T} \quad [\text{eq. 2-1}]$$

where P is a pressure in torr and T is temperature in Kelvin. The temperature of TMIn is fixed to 18 °C, resulting in a vapor pressure of 1.45 torr. As a group V source, electronic grade trimethylantimony (TMSb), [(CH<sub>3</sub>)<sub>3</sub>Sb] is adapted supplied from Rohm & Hass. The vapor pressure of TMSb is expressed in eq. 2-2. The TMSb sources are kept at a temperature of 0 °C and it has a vapor pressure of 30.95 torr.

$$\log_{10} P(TMSb) = 7.7068 - \frac{1697}{T} \quad [\text{eq. 2-2}]$$

For p-type doping of the InSb, group II source of diethylzinc (DEZn),  $[(\text{CH}_3)_2\text{Zn}]$  is used. It is also supplied from the same company as mentioned. The vapor pressure of DEZn is represented in eq. 2-3

$$\log_{10} P(DEZn) = 8.28 - \frac{2190}{T} \quad [\text{eq. 2-3}]$$

DEZn is maintained at a temperature of  $-10\text{ }^\circ\text{C}$ . The list of MO source materials used in this study is given in Table 2.1 along with the melting point

### 2.1.3 InSb substrate preparation

The substrate used for the InSb epitaxial growth is InSb substrate with an orientation of (100). The InSb substrate supplied from Wafer Technology. LTD, is Te doped with a concentration of  $5\sim 20 \times 10^{14} \text{ cm}^{-3}$  at 77 K. The side of wafer is 2 inch with single side polished as an epi-ready condition. For the growth, 2 inch InSb substrates are cleaved into some pieces with a size of 7 mm x 7 mm. Substrate preparation before inserting into the growth chamber is degreasing, etching, and rinsing. Acetone, methanol, and isopropylalcohol (IPA) are used for each 2 min in ultrasonic condition for sample degreasing. And then, samples are rinsed in running DI water for 2 min to remove residual solvent followed by dried with filtered  $\text{N}_2$ . The surface of InSb samples is etched by the mixture of lactic acid and nitric acid (10:1 with a

volume ratio) for 5 min to remove native oxides. It is rinsed in running DI water for 30 sec to remove etchant existed on the surface followed by N<sub>2</sub> dried. Due to the viscosity of lactic acid, enough stirring of etchant mixture are necessary for completely mixing in order not to etch InSb surface selectively. More detail etching process will be described in the chapter 3.

#### **2.1.4 Epitaxial growth procedures**

The epitaxial growth procedure can be divided by four major steps: MOCVD start up, epitaxial growth, MOCVD shut down, and growth chamber cleaning. After prepared InSb sample as described in the previous section are inserted into the growth chamber, pumping is performed by closing all the valves for the MOCVD start up process. N<sub>2</sub> purge is performed through growth chamber to remove air and residual impurities. Subsequent four times of N<sub>2</sub> purge brought down the pressure of reactor below 150 mtorr. Purified H<sub>2</sub> as a carrier gas with a flow rate of 1.5 slm is switched into the reactor to replace N<sub>2</sub>. For the system stabilization, purge with H<sub>2</sub> is maintained for 20 min through all the parts such as source line and growth chamber. During H<sub>2</sub> purge, MFC control box, electronic pressure controller (EPC) readout must be check that it operates under setting conditions. All the inlet and outlet valves of MO source are opened to pass the H<sub>2</sub> gas into MO bubbler.

After checking all the parameter and equipments, for the epitaxial growth process, RF generator is turned on and sample is heated up to 400 °C under

H<sub>2</sub> ambient. However, TMSb overpressure has to be maintained in order to prevent any surface degradation due to Sb evaporation from the InSb substrate. As the temperature is reached at 515 °C, in-site thermal cleaning process is proceeded for 3 min to remove any H<sub>2</sub>O vapor or some residues on the InSb substrates. A temperature in growth chamber is cooled down to the target temperatures, group III MO source is switched to the run line from the vent line, starting InSb growth. The InSb growth lasts for 60 min or even further time.

After growth is finished, In MO source is switched from run line to vent line and hence stopping the source. RF generator is then turned off and samples are allowed to cool down naturally. The Sb overpressure is maintained to 400 °C in order not to evaporate Sb elements from InSb surface. All the inlet and outlet of MO source is closed, resulting in the H<sub>2</sub> flow through by-pass line. After the temperature is cooled down to 150 oC, H<sub>2</sub> is replaced to N<sub>2</sub> gas. The pressure of growth chamber is cycled from atmosphere to low pressure about four times to remove any residual MO source and H<sub>2</sub> in the source line and growth chamber prior to unload the samples.

For the reproducible growth of InSb, chamber cleaning process is very important procedure. Since deposited on the quartz tube and susceptor are affecting to degrade the film quality of the following growth as well as hindering and accurate reading of the sample temperature by the IR pyrometer, the cleaning is performed just after the growth.

Mo source	Acronym	Melting point (°C)	Phase
Trimethylindium	TMI <sub>n</sub>	88.4	Solid
Trimethylantimony	TMS <sub>b</sub>	-87.6	Liquid
Diethylzinc	DEZ <sub>n</sub>	-28	Liquid

Table 2.1. MO source materials used in this study for MOCVD growth

## **2.2. Dielectric deposition systems**

### **2.2.1. Plasma Enhanced Chemical Vapor Deposition (PECVD)**

A silicon dioxide ( $\text{SiO}_2$ ) and silicon nitride ( $\text{Si}_3\text{N}_4$ ) are deposited by plasma enhanced chemical vapor deposition (PECVD) at ISRC. PECVD system is manufactured by the surface technology system (STS). For  $\text{SiO}_2$  deposition, 5 %  $\text{SiH}_4$  diluted  $\text{N}_2$ ,  $\text{N}_2\text{O}$ , and  $\text{N}_2$  gas are used with a flow rate of 160, 1500, and 240 sccm, respectively. The deposition pressure is fixed to 550 mtorr. RF power for plasma generation is fixed to 60 W with a frequency of 187 kHz. The deposition temperature is 180 and 250 °C. The deposition rate is confirmed to be 200 Å/sec. For  $\text{Si}_3\text{N}_4$  deposition, source gases are 5 %  $\text{SiH}_4$  diluted  $\text{N}_2$ ,  $\text{NH}_3$ , and  $\text{N}_2$  with a flow rate of 800, 10, and 1200 sccm, respectively. RF power for the plasma generation is the same as the  $\text{SiO}_2$  condition. The deposition rate of  $\text{Si}_3\text{N}_4$  is turned out to be 100 Å/sec

### **2.2.2. Electron Beam Evaporation**

Electron beam evaporator is used to deposit zincsulfide ( $\text{ZnS}$ ) films. This evaporator is manufactured by Ultech.  $\text{ZnS}$  source for the evaporation has 99.99 % purity and its stoichiometry is 1 confirmed by the refractive index (2.4 at 632 nm). The base pressure is  $2 \times 10^{-6}$  torr and deposition rate are varied from 0.5 to 2.0 Å/sec.  $\text{ZnS}$  source soaking time is fixed for 4 min totally.  $\text{ZnS}$  film deposition is conducted at room temperature.

## **2.3. Device fabrication methods**

A simple mesa type device structures are fabricated by conventional lithography, wet etching, dielectric deposition, and metallization process. An entire process for device fabrication is illustrated in Fig. 2.2

### **2.3.1. Sample preparation**

Before fabricating InSb devices, as-grown InSb samples are degreased in solvents as mentioned in the previous section 2.1.3. Native oxides are removed by dipping in dilute HF solution. Then samples are rinsed in DI water followed by N<sub>2</sub> dry.

### **2.3.2. Mesa etching**

To fabricate mesa structures, patterns are defined by photoresist (PR) of AZ 7210 via a conventional photo lithography process at ISRC (SNU). The detailed processes are described as follows:

- a) Sample pre-baking: pre-baking at 100 °C for 3 min is necessary to remove any solvents, acids, and water vapor in order to increase the PR adhesion. Then samples must be cooled down at room temperature for 3 min.
- b) PR coating: Hexamethyldisilazan (HMDS) and AZ 7210 are spin coated on the InSb substrate in regular sequence. First HMDS are coated to increase adhesion of PR on InSb substrate with a spin

rate of 500 rpm for 5 sec and 2500 rpm for 5 sec. Then PR is spin coated with a spin rate of 500 rpm for 5 sec and 4000 rpm for 35 sec. The thickness of PR confirmed by the surface profiler is 0.9  $\mu\text{m}$ .

- c) Soft baking: PR coated has to be baked in order to remove liquid in PR. So samples with PR coated are heated at 95 °C for 2 min.
- d) Exposure: Using designed mask, UV exposure process is essential to make patterns in PR. Exposure process is done by the MA-6 II aligner (Karl-Suss) with the intensity of 20  $\text{mW}/\text{cm}^2$  for 11 sec. A soft contact and front side illumination are selected.
- e) Post exposure baking (PEB): PEB process is conducted at 110 °C for 45 sec.
- f) Develop: A PR is developed by dipping in AZ300MIF with stirring. The develop time is approximately 15 sec.
- g) Hard baking: A developed PR is hard baked at 130 °C for 2 min.

After PR patterning, InSb epitaxial layers are etched by dipping in the mixture of citric acid and  $\text{H}_2\text{O}_2$  (100g: 100 ml). The temperature of etchant are maintained at 60 °C and etching process is done for 25 min with an etch rate of 70 nm/min. An etching rate is obtained by changing etching time as shown in Fig. 2.3. The etched thickness is measured by surface profiler (a-step). After mesa etching, residual PR is removed by dipping in acetone solution.

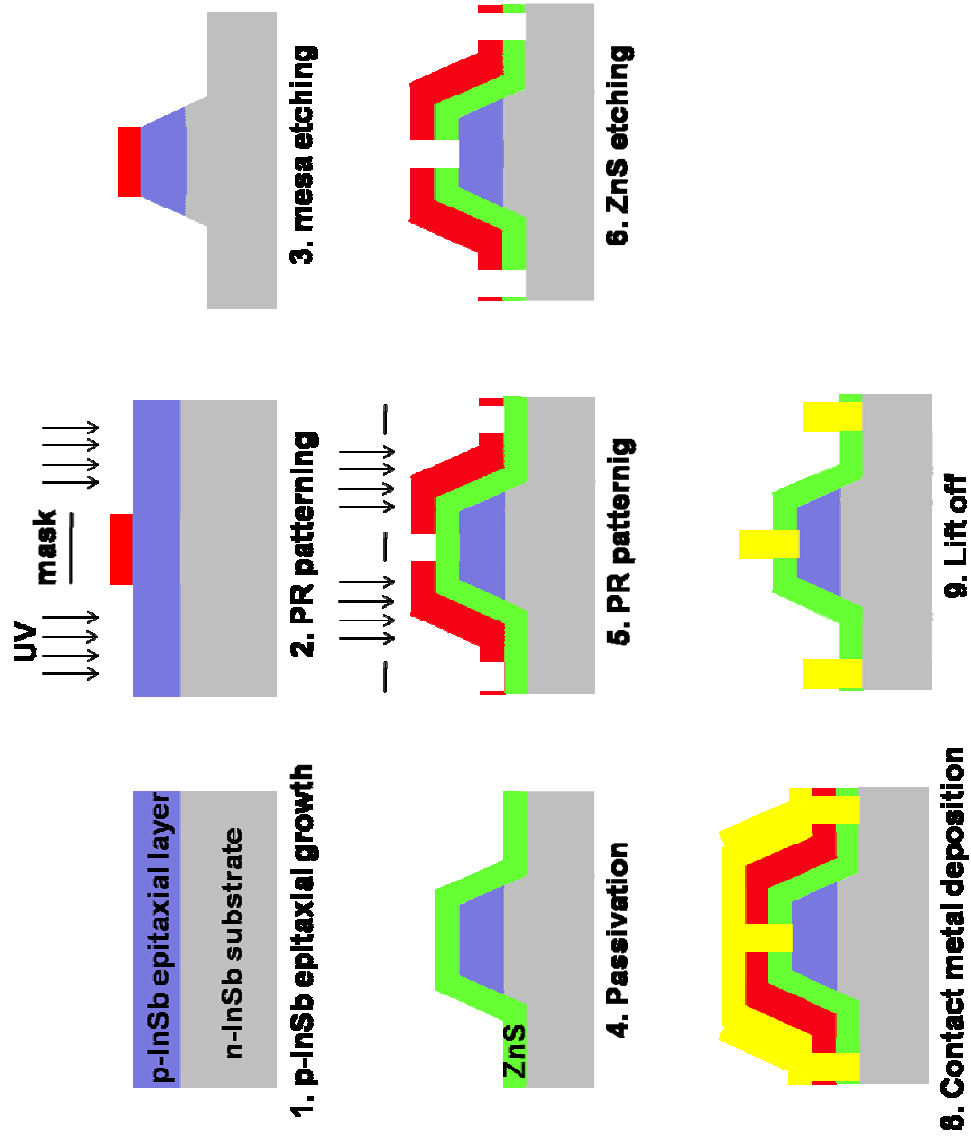


Fig. 2.2 An illustration of InSb device fabrication sequence

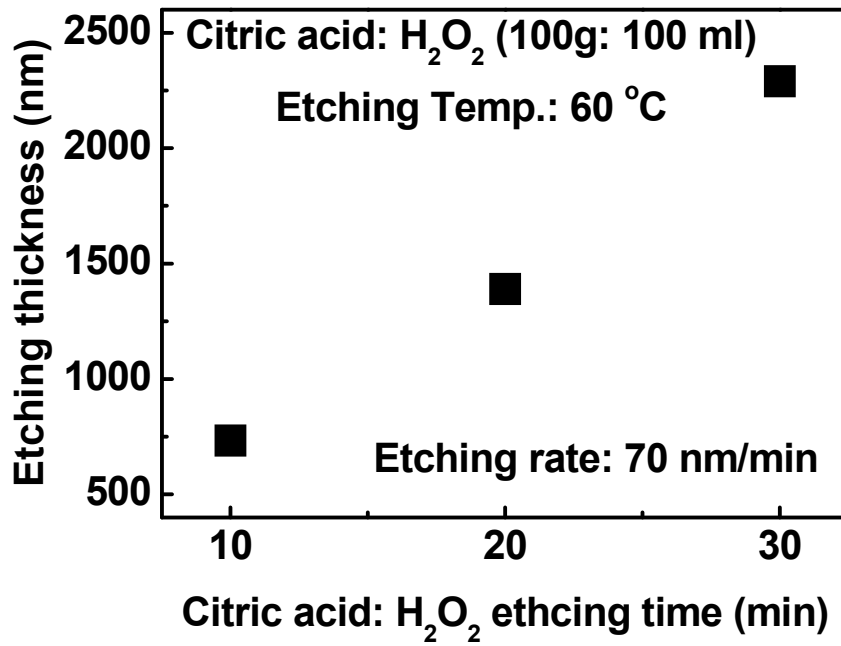


Fig. 2.3 The etching rate of InSb epitaxial layer in the mixture of citric acid and H<sub>2</sub>O<sub>2</sub>. The etching rate is 70 nm/min.

### **2.3.3. Dielectric deposition**

Dielectrics were deposited on mesa patterned structures for surface passivation using electron beam evaporator at KANC.

### **2.3.4. Metallization**

A PR patterning process is needed to make contact for the electrical measurements. A selectively etching of ZnS passivation layers are also conducted for the metal contact in this process. Negative PR AZ 5214 is used. More detail process is described below:

- a) Sample pre-baking: pre-baking at 100 °C for 3 min is done after the sample cleaning process.
- b) PR coating: Hexamethyldisilazan (HMDS) and AZ 5214 are spin coated on the InSb. The spin rate of HMDS is 500 rpm for 5 sec and 2500 rpm for 5 sec. That of AZ 5214 is 500 rpm for 5 sec and 4000 rpm for 40 sec
- c) Soft baking: PR coated is heated at 80 °C for 5 min.
- d) Exposure: Exposure process is done with the intensity of 20 mW/cm<sup>2</sup> for 3.4 sec.
- e) Image reversal baking: samples are heated on the hotplate at 100 °C for 5 min
- f) Flood exposure: Samples are exposed to UV light for 24 sec with the same intensity of 20 mW/cm<sup>2</sup>.
- g) Develop: Diluted AZ 300MIF is used to develop the PR. The ratio

of this developer is 6:1 (AZ 300MIF:H<sub>2</sub>O in a volume ratio). The develop time is for 35 sec.

- h) After confirming the PR removal by optical microscope, exposed ZnS layer are etched by dipping in HCl solution for 1 sec.
- i) Metallization: Ti/Au are deposited by electron beam evaporator with a thickness of 20/200 nm.
- j) PR removal: After metallization, a PR is removed by dipping in acetone solvent.
- k) Metal alloying: In order to make an ohmic contact, rapid thermal annealing treatment in N<sub>2</sub> ambient is conducted at 180 °C. Specific contact resistance are measured by transmission line method with 4 point probe at 77 K. the specific contact resistance is obtained as low as  $9.9 \times 10^{-5} \Omega\text{cm}$  at 180 °C

## **2.4. Characterization tools**

After the InSb growth and dielectric deposition, its structural, compositional, optical, and electrical property are analyzed by using various analysis tools. Now I will briefly express the analysis tools and techniques.

### **2.4.1. Atomic Force Microscopy**

In order to investigate surface morphology and average roughness using a root-mean-square, a measurement using atomic force microscopy (AFM) (Seiko Instrument, SPA-400) is conducted under non-contact mode in an atmospheric ambient. The Au-coated Si tip is used for all the measurements.

### **2.4.2. Ellipsometry**

Ellipsometer measurement is carried out to identify the thickness of native oxides on InSb. Native oxides are so thin that I can not measure it easily. The only way to measure it accurately is using transmission electron microscopy which is expensive technique. On the other hand, ellipsometer is the easiest way and cheap measurement technique. In this experiment, J. A. Woollam (M-2000V) ellipsometer is used to fit the thickness of native oxide. Wide range between 390 and 1000 nm measurement are conducted. A Quartz Tungsten Halogen and back-thinned silicon CCD array is the light source and detector, respectively.

### **2.4.3. High Resolution X-Ray Diffraction**

High resolution X-ray diffraction technique is a well established and commonly used tool for the non-destructive characterization of semiconductor films. By determination of diffraction patterns, alloy composition and stress induced by lattice mismatch can be obtained. For this measurement, two type of XRD system such as D8-Advance manufactured by BRUKER MILLER CO. and X'pert Pro manufactured by PANalytical are used. The alloy composition is easily identified by D8-advance and crystal quality of films deduced by full width at half maximum (FWHM) are measured by X'pert Pro system. 3 kW x-ray tube with Cu target of a 1.5406 Å wavelength is equipped in the D8 system. In the X'pert Pro system, the same targets of Cu with 1.5406 Å are used. The generator voltage and tube current are 30 kV and 10 mA are applied for the measurements. The rocking curve of (004) peak are conducted to obtain FWHM of InSb films.

### **2.4.4. Scanning Electron Microscopy**

In order to determine the thickness of films and surface measurement, scanning electron microscopy (SEM) (Hitachi SU70) measurements are conducted. The acceleration voltage and emission current are 5~15 kV, which is depending on the measurement condition and 26 mA, respectively. For the dielectric measurement, Cr coated samples are prepared since dielectrics are not conductive films.

#### **2.4.5. Transmission Electron Microscopy**

The measurement of Transmission Electron Microscopy (TEM) is carried out to confirm the thickness of native oxides. The TEM samples are fabricated by Focused Ion Beam (FIB) using Ga ion with a current of 20 nA. JEOL JEM-3000F TEM is used for the high resolution TEM analysis with an acceleration voltage of 300 KV

#### **2.4.6. Secondary Ion Mass Spectroscopy**

Secondary Ion Mass Spectroscopy (SIMS) depth profiling is performed at Evans Analytical Group to investigate the presence and concentration of impurities and dopant in the epitaxial layers. A Cs<sup>+</sup> ion is used as a primary ion source and depth profiling is conducted with a crater size of 1 x 1 cm<sup>2</sup>.

#### **2.4.7. Energy Dispersive X-ray Spectroscopy**

Energy Dispersive X-ray Spectroscopy (EDS or EDX) are used to determine various elements and its composition ratio in the epitaxial layers which is connected with SEM SU-70. The acceleration voltage is varied from 5 to 10 kV depending on a sample condition.

#### **2.4.8. X-ray Photoelectron Spectroscopy**

X-ray Photoelectron Spectroscopy (XPS) measurements are conducted to

identify the chemical bindings at bulk and/or interface region of films. Thermo VG, UK XPS equipped with monochromated Al X-ray source (Al  $K_{\alpha}$ = 1486.6 eV) with a condition of 12 kV and 3 mA are utilized. The base pressure and pressure during a measurement of this XPS system are  $2.8 \times 10^{-9}$  and  $4.8 \times 10^{-9}$  mbar, respectively. For the depth profile, Ar ion etching is used with the condition of 1 kV and 2.0  $\mu$ A. The etching rate is 0.15 nm/sec. The raster size and measurement area are 2 mm x 2 mm and 400  $\mu$ m in diameter.

#### **2.4.9. Auger Electron Spectroscopy**

To compare the contents of element in films, Auger Electron Spectroscopy (AES) (PHI 700, ULVAC-PHI, INC) measurement is conducted at Korea Institute of Science and Technology (KIST). An electron beam energy and target current are 5 kV and 10 nA, respectively. The measurements are done with a tilting of 30 degree and the samples are sputtered by Ar ion with a voltage of 3 kV. Its raster area is 2 mm x 2 mm with an etching rate of 160  $\text{\AA}/\text{min}$

#### **2.4.10. Photoluminescence**

A photoluminescence (PL) measurement is carried out in order to find defects in the epitaxial layers at Korea Institute of Science and Technology (KIST) with Dr. S. H. Kim and Dr. M. S. Park assistance. The Fourier Transform PL spectroscopy is equipped in the Bruker Vertex 80 V (FTS) for

low temperature and vacuum condition. The excitation laser is 532 nm line of Ar<sup>+</sup> laser with a power density from 29 to 788 mW. The liquid nitrogen (LN<sub>2</sub>) cooled mercury cadmium telluride (MCT) detector with a detection range from 2 to 30 μm is used to detect PL signal. The measured temperature range is varied from 10 to 300 K cooled with liquid helium. And ZnS and CaF<sub>2</sub> windows for the transparent of infrared are installed in this system.

#### **2.4.11. Capacitance-Voltage measurement**

In order to measure the electrical properties of dielectrics deposited on InSb, capacitance-voltage (C-V) measurements are conducted at 77 K in all measurements. Agilent 4980A LCR meter is employed to measure high frequency C-V of dielectrics. For a high frequency measurement (1 MHz), a small-amplitude AC voltage (15 mV) is superimposed in DC bias with a sweep rate of 0.1 V/s. All measured high frequency C-V curve is compared with the ideal high frequency C-V calculated theoretically in obtain the interface trap density ( $D_{it}$ ) and flat band voltage shift ( $\Delta V_{FB}$ ). More detailed expression and theoretical background are expressed in Appendix A.

#### **2.4.12. Current-Voltage measurement**

A dark current of device is measured by current-voltage (I-V) measurements at 77 K. Keithley 2636A parameter analyzer is used to measure the electrical properties. Some cases, current is transformed into current density (J)

All the C-V and I-V curves are measured in LN<sub>2</sub> cooled cryostat equipped with Agilent 4980A and Keithley 2636A. Figure 2.4 shows the cryostat system installed in Compound Semiconductor Epitaxy Laboratory (CSEL) at Seoul National University.

### **2.4.13. Hall measurement**

The carrier concentration and Hall mobility in unintentionally doped and intentionally doped with Zn are characterized by the Hall measurements at KIST assisted with Dr. Jin dong Song assistance [Ecopia, HMS-3000]. For the Hall measurements using Van der Pauw method, four ohmic contacts are formed on the InSb surface. All measurements are conducted at 77 K and magnetic field applied to the sample is fixed at 0.37 T. An applied current are 10 nA and sometimes current are changed.



Fig. 2.4 A cryostat system cooled by LN<sub>2</sub> equipped with Agilent 4980A and Keithley 2636A

# **Chapter 3. Surface treatment ambient on the quality of InSb epitaxial layers**

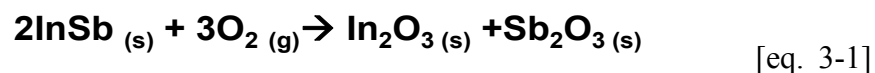
## **3.1. Introduction**

The word used in this thesis, epitaxy, is originated from two ancient Greek words of  $\epsilon\pi\iota$  and  $\tau\alpha\xi\iota\varsigma$ . The  $\epsilon\pi\iota$  and  $\tau\alpha\xi\iota\varsigma$  are translated to resting upon and arrangement, respectively. The epitaxy refers to extended single-crystal film formation on top of crystalline substrates. There are two distinguished types of epitaxy. Homoepitaxy refers to the case where the film and substrate are the same material with the same crystallographic orientation. In this case of the homoepitaxy, it has advantages to obtain high quality of epilayers with free of defects, which represents that the epilayers is purer than the wafer substrates. This is caused by the same lattice parameters which realizing perfect matched and there is no interfacial bond straining. The second type of epitaxy is known as heteroepitaxy. In this case, films and substrates are composed of different materials. Due to lattice constant differences between films and substrates, it produces the dislocation and defects at the interface regions. However, in modern semiconductor technologies, it has been widely used and important techniques in the processing of electronic and optoelectronic devices.

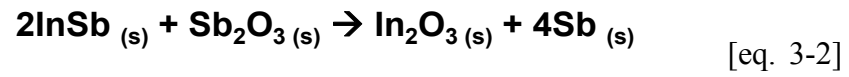
In order to growth high quality of epilayers, substrates have to be well prepared with smooth, stoichiometric, atomically clean and oxide-free surface.

Generally, well treated surface is prepared by two methods: *ex-situ* wet chemical etching and *in-situ* thermal cleaning (TC). *Ex-situ* wet chemical etching is widely used to remove organic and/or metal contaminants even native oxides using chemical solutions. In-situ TC is also a well-known method for epitaxial growth, especially for the growth of arsenide (As) and phosphide (P) based III-V semiconductors. In the process of in-situ TC, contaminants left after wet cleaning and/or sometimes native oxides, in the case of As and P based material growth, can be easily removed from the surface at a high temperature regions.

Let me study the mechanism of native oxides formation on InSb. Like other III-V semiconductors, native oxides formation of InSb has similar a mechanism. When the clean InSb substrate is exposed to air, its surface is easily oxidized and a several nanometer thick native oxides layer are quickly formed upon exposure to air. A schematic diagram is represented in Fig. 3.1. Oxidation of InSb starts with the breakage of the bonds of surface atoms and subsequent rearrangement after initial oxide layer formation. The oxygen in air diffuses into the InSb surface, reacting with In and Sb atoms to form a In oxide (In<sub>2</sub>O<sub>3</sub>) and Sb oxide (Sb<sub>2</sub>O<sub>3</sub>), respectively. It is represented in eq. 3-1.



This native oxide formation process is non-equilibrium process, making further surface reaction proceeded as shown in eq. 3-2.



$\text{Sb}_2\text{O}_3$  phase formed reacts with more InSb to form a further  $\text{In}_2\text{O}_3$  and elemental Sb. Thermodynamically,  $\text{In}_2\text{O}_3$  and elemental Sb are the only stable phases after InSb is oxidized [1]. Equation 3-1 and 3-2 are spontaneous reaction even at room temperature.

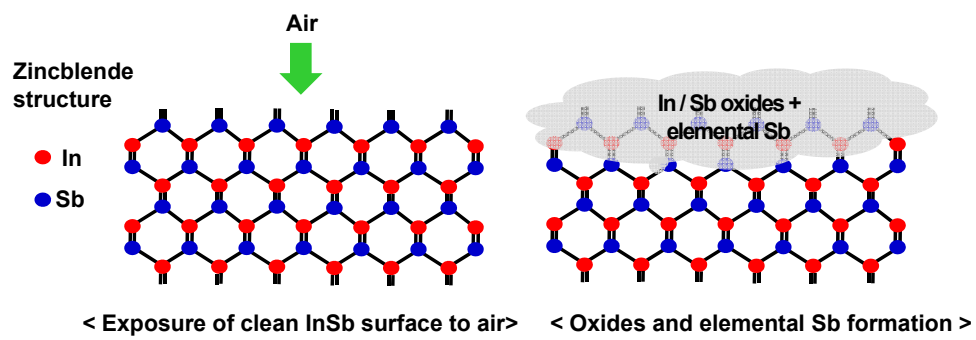


Fig. 3.1 A schematic illustration of InSb native oxides formation process when exposed to air. Native oxides are composed of indium oxides ( $\text{In}_2\text{O}_3$ ) and antimony oxides ( $\text{Sb}_2\text{O}_3$ ) and elemental Sb

### 3.2. Motivation

As mentioned in section 3.1, a presence of native oxides on the surface is an obstacle for the epitaxial growth. Hence it has to be removed before epitaxy. In both native oxides of InSb,  $\text{Sb}_2\text{O}_3$  has a much lower melting point ( $\sim 655^\circ\text{C}$ ) rather than that of  $\text{In}_2\text{O}_3$  ( $\sim 2000^\circ\text{C}$ ). It implies that  $\text{Sb}_2\text{O}_3$  can be removed more easily as a result of evaporation from the surface. During the sublimation of Sb from the surface,  $\text{In}_2\text{O}_3$  can not be evaporated from the InSb surface due to the stable molecule characteristics. It represents that  $\text{In}_2\text{O}_3$  can not be removed during the thermal cleaning process because it is stable even at the melting point of InSb ( $527^\circ\text{C}$ ). Since it is difficult to remove during TC process, native oxides of InSb have been removed by wet chemical etching [2-4].

After wet etching of native oxides, additional native oxides are formed on the surface as exposed to air before inserting MOCVD growth chamber. Before epitaxial growth of InSb, the substrates are *in-situ* thermally cleaned in the chamber to remove  $\text{H}_2\text{O}$  vapors and some residues existed on the surface. This method is a well known process for the growth of arsenide (As), phosphide (P) based III-V semiconductors [5-7]. As and P based III-V semiconductors are thermally cleaned under the large flow of group V hydride such as arsine ( $\text{AsH}_3$ ) and phosphine ( $\text{PH}_3$ ). The active hydrogen generated from the group V hydride decomposition plays an important role in removing the native oxides on the surface [8]. The desorption of group V atoms on the surface during TC is inhibited due to the high vapor pressure of

group V materials in the gas phase, suppressing the formation of non-stoichiometric and rough surface [8]. Unfortunately, there are no commercially available antimony (Sb) based hydride sources even though there is a stibine ( $\text{SbH}_3$ ) which is unstable even at room temperature, starting the source decomposition [9]. As a result, most of Sb based III-V growth using MOCVD use alkyl-based Sb source such as trimethylantimony (TMSb) [3, 4, 10, 11] and triethylantimony (TESb) [12-15]. As a result, removing native oxides and obtaining stabilized surfaces are difficult when the alkyl based Sb sources are used due to the lack of active hydrogen. This is the first obstacle to remove native oxides through *in-situ* TC process.

Another obstacle is the low vapor pressure of Sb compared to that of As and P based materials as shown in Fig. 3.2. As the vapor pressure of Sb is almost lower order of  $10^7$  rather than that of As and P at around 750 K where InSb can be normally grown. In case of As and P based semiconductors, there is no any group V condensation on the surface due to the high vapor pressure since un-reacted group V elements can diffuse out of boundary layer and removed through the gas phase if there is no available group III elements on the surface. On the other hand, even though the TC of InSb under group V ambient is normal process [8, 10], TC under group V ambient shows the controversial problems. It was reported that the InSb epitaxial layers can be grown on the substrate thermally cleaned without Sb ambient [3, 16-18]. In that large flow of Sb during TC process is preferred to suppress the loss of Sb atoms from InSb surface [18] however, in many cases this technique lead to rough surface morphology due to the condensation of Sb hillocks on the surface [17]. So, precisely control of Sb overpressure has to be maintained

during TC process.

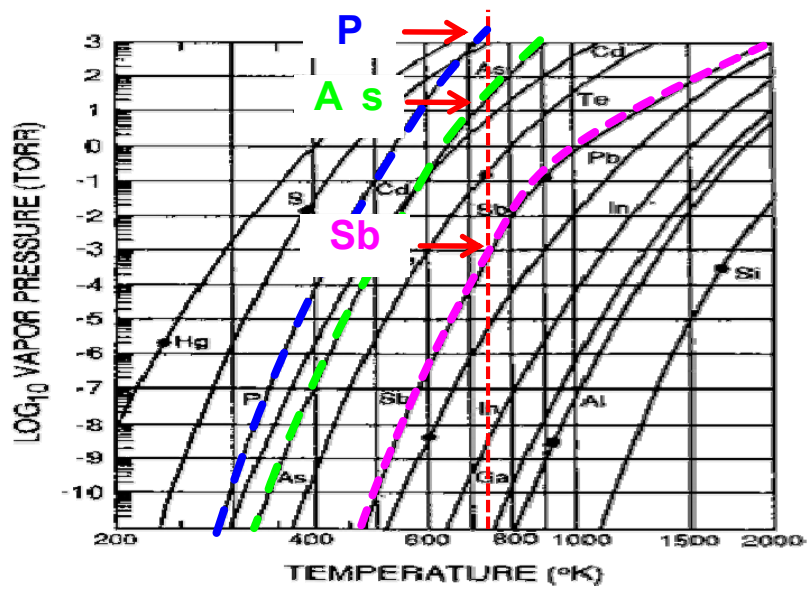


Fig. 3.2. Vapor pressure of the III-V elements as a function of temperature

### 3.3. Theoretical background [19, 20]

Epitaxial crystal growth is an example of a dynamical phase transition. A stable phase, the epitaxial layers, grows out from a metastable phase, that is from an amorphous solid, melt (or liquid solution), or vapor. The driving force for the epitaxial growth is the chemical potential difference of the stable and the metastable phases. The simple assumption of the linear response, which means that the growth velocity is proportional to the driving force, gives ideal linear growth laws.

Let me explain the brief review of the basic concepts and terminology of thermodynamics before express the relationship between solid and vapor composition at the interface, during the epitaxial growth process, by assuming the thermodynamic equilibrium conditions. Phase is the first important phenomenological concept used in this thesis when considering thermodynamics of crystal growth. This is a distinguishable region with other phases. Thus, we can consider various phases such as solid, liquid, and vapor phases when growing different materials systems using epitaxial method.

The basic purpose of thermodynamics when treated in epitaxial growth is to determine the composition of the various phases and reaction directions in an equilibrium system at a constant temperature and pressure condition. The terminology of equilibrium means that Gibbs free energy,  $G$ , has the minimum values. Gibbs free energy is determined in terms of the enthalpy,  $H$ , and entropy,  $S$ :

$$G = H - TS \quad \text{[eq. 3-3]}$$

where,

$$H = U + PV \quad [\text{eq. 3-4}]$$

and U is the internal energy, V is the system volume, and P is the pressure of the system. G, H, S, U, and V are all extensive quantities, i.e., they all depend on the size of the system. Since two phases system was considered, the total free energy is given:

$$G^{\text{TOT}} = G^{\alpha} + G^{\beta}, \quad [\text{eq. 3-5}]$$

Since  $G^{\text{TOT}}$  is a minimum a equilibrium, the change in  $G^{\text{TOT}}$  by transferring an infinitesimally small number of moles of component i ,  $dn_i$ , between two phases caused no change in  $G^{\text{TOT}}$ . This may be expressed as:

$$\left(\frac{\partial G}{\partial n_i}\right)_{T,P,n}^{\alpha} = \left(\frac{\partial G}{\partial n_i}\right)_{T,P,n}^{\beta} \quad [\text{eq. 3-6}]$$

where the superscripts  $\alpha$  and  $\beta$  represent the two phases. The partial derivative of G with respect to  $n_i$  is so important quantity for thermodynamic calculation that it is given a name, the chemical potential, represented as  $\mu_i$ . Thus, the equilibrium condition may be expressed in the simple form

$$\mu_i^{\alpha} = \mu_i^{\beta} \quad [\text{eq. 3-7}]$$

for each component in the system. For a reversible perturbation of the system, it can be shown from the equation 3-4 and 3-5 and the relationship of  $dU=TdS-SdT$  that

$$dG=VdP-SdT \quad [\text{eq. 3-8}]$$

This is the one of the Maxwell's equation of thermodynamics [20]. For an ideal system (e.g., ideal gas)  $PV=nRT$ , thus, at constant T, equation 3-9 yields for a change in pressure

$$dG=nRTd \ln(P) \quad [\text{eq. 3-9}]$$

hence, for an ideal single gas

$$\mu = RT \ln(P) \quad [\text{eq. 3-10}]$$

and

$$\mu = \mu^0 + RT \ln (P/P^0) \quad [\text{eq. 3-11}]$$

where,  $\mu^0$  and  $P^0$  represent the chemical potential and pressure of an arbitrary standard state. For an ideal gas mixture,

$$\mu_i = \mu_i^0 + RT \ln (P_i/P_i^0) \quad [\text{eq. 3-12}]$$

where  $P_i$  is the partial pressure, equal to the mole fraction  $x_i$  multiplied by  $P$ , and the standard state is usually a pure component  $i$ .

### **3.4. Experimental procedures**

In order to optimize the best InSb surface quality for the epitaxial growth, InSb substrates were prepared by solvent cleaning, native oxide removal, thermal cleaning depending on the ambient subsequently. Solvents cleaning was treated as represented in the Sec. 2 and followed by drying with N<sub>2</sub> gas. For the native oxides etching, the mixture of lactic acid (LA) and nitric acid (NA) with different mixture ratio and etching time was investigated. Then rinsing in DI water was adapted to remove any acids on the surface. In order to investigate the effects of group V overpressure conditions on surface morphology, thermal cleaning (TC) process was done under either H<sub>2</sub> or TMSb ambient with different temperature, flow rate, and time. All the optimized condition was determined using surface morphology and native oxides thickness measured by AFM, and ellipsometer, respectively.

### **3.5. *ex-situ* wet chemical etching of InSb substrate**

Before in-situ TC process, the native oxides of InSb have to be removed by wet chemical etching process as explained in the Sec. 3.2. There are many etchant reported for InSb etching. However, for the epitaxial growth, the mixture of lactic acid (LA) and nitric acid (NA) were widely used [4]. In this thesis, the same etchant were used to remove native oxides.

To ensure the ellipsometer measurement data, TEM analysis was performed. Figure 3.2 (a) shows the cross section TEM (XTEM) images of air exposure InSb substrate. Native oxides region with different contrast was observed and it is confirmed by diffraction patterns with amorphous phases. The air exposed InSb substrates has the 24 Å of native oxides thickness as confirmed by XTEM measurements. The same sample was used to measure the native oxide thickness using ellipsometer. The thickness of native oxides measured by ellipsometer is also 24 Å. From the consistent thickness measured by two techniques, the thickness of native oxides measured by ellipsometer is reliable values.

In this experiment, native oxides were effectively removed in the mixture ratio of two acids. The five mixture ratios of LA: NA = 1:1, 5:1, 10:1, 20:1 and 50:1 were investigated. In case of (1:1) for dipping at 300 sec, the InSb surface turned out to be burned as confirmed by optical microscopy as shown in Fig. 3.3. The surface was not uniform due to the burned area so ellipsometry measurement was not conducted as shown in fig 3.3 (c). In Fig. 3.3 (c), in case of (50:1), the thickness of native oxides were increased from

27 to 40 Å as the etching time was increased from 180 to 360 sec, indicating that oxidation was proceeded. In case of LA:NA ratio of 5:1 and 20:1, the native oxides thickness was reduced with increasing etching time. I found that best effective etchant for InSb native oxides was determined by the mixture ratio of 10:1 as etching was done about 300 sec as shown in Fig. 3.3 (c).

For the effective wet etching, oxidizer, etchant and diluter are mixed adequately. In this experiment, NA was used as an oxidizer and LA has a role of etchant. Dilution was not conducted. With increasing oxidizer ratio, the surface will be significantly oxidized due to the strong effects of oxidizer. On the other hand, no etching will be conducted if there will be lots of etchant ratio because etchant will not attack covalent bond of InSb. Oxidizer can break the covalent bond in order to remove easily by etchant. In case of (50:1) ratio, there are too many etchant compared to the oxidizer, NA. In this case, although InSb surface is oxidized due to the presence of NA, etching process is prohibited due to the hindrance of LA supply towards the oxidized InSb surface. It produces the increase of native oxide thickness. Based on the empirical rule in III-V semiconductor etching [21], NA breaks the covalent bonds of InSb and subsequently the electron rich  $\alpha$ -hydroxy acids (lactic acid) bind to In ions ( $\text{In}^{3+}$ ). The additional action of the  $\alpha$ -hydroxy acids makes an important role to remove In. The binding between lactic acid and In ions were due to the presence of numerous lone electron pairs on the oxygen atoms of the  $-\text{COOH}$  and the  $-\text{OH}$  groups [22]. With increasing the concentration of lactic acids, the hindrance of unpaired electrons by repulsive forces is the main origin that lactic acid can not move to the oxidized surface

effectively. The surface morphology was analyzed by the AFM as shown in Fig. 3.4. The mixture of LA: NA (10:1) solution was used as an etchant and etching time was varied. The surface morphology of bare InSb is represented in Fig. 3.4 (a) with a RMS roughness of 0.14 nm and the highest RMS roughness is obtained at 120 sec. It is gradually decreased with increasing etching time from 120 to 300 sec. It is speculated that surface is not reacted with etchant significantly with small variation of RMS roughness up to 60 sec. However, the InSb surface was selectively etched, showing the large RMS roughness then it is smoothing with increasing etching time.

The thickness of native oxides was reduced since rinsing durations in DI water is reduced. After etching of native oxides in the mixture of lactic acid and nitric acid (10:1) with rinsing in DI water for 120 min, the thickness was estimated at 12 Å by measuring ellipsometry as shown in Fig. 3. 3 (c). However, it was reduced by rinsing in DI water for shorter time to 30 sec, its thickness was estimated by 7.8 Å as represented in Fig. 3. 5 (a). It is indicating that native oxide was reproduced even in the DI rinsing process by exposed to the DI water (H<sub>2</sub>O).

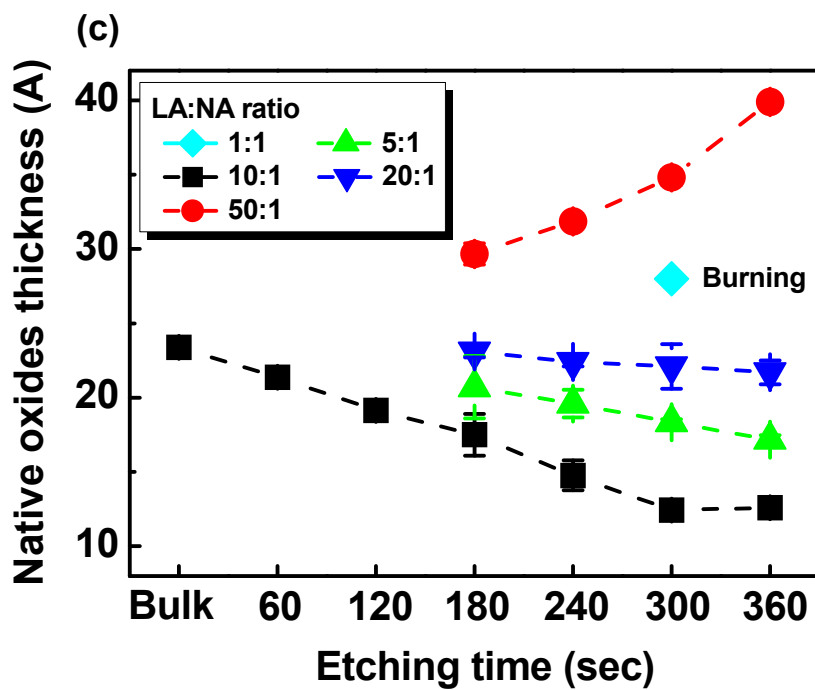
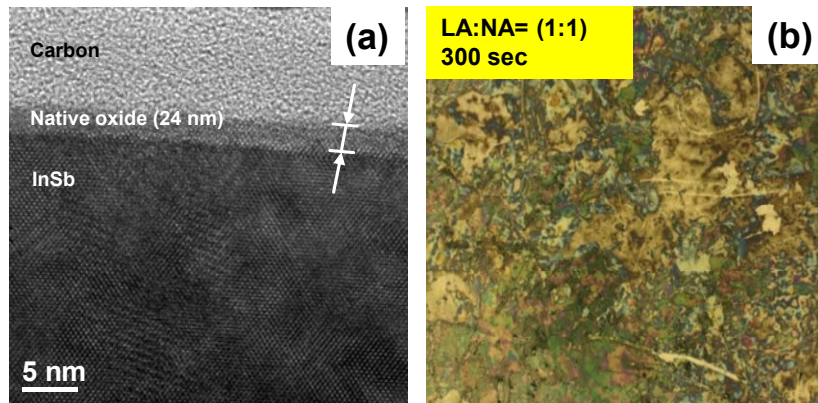


Fig. 3.3. (a) A XTEM image of air exposed InSb substrate with 24 Å thickness of native oxides. (b) Optical microscopy images of surface etched in lactic: nitric acid (1:1) (c) native oxide thickness measured by ellipsometer depending on the mixture ratio and etching time.

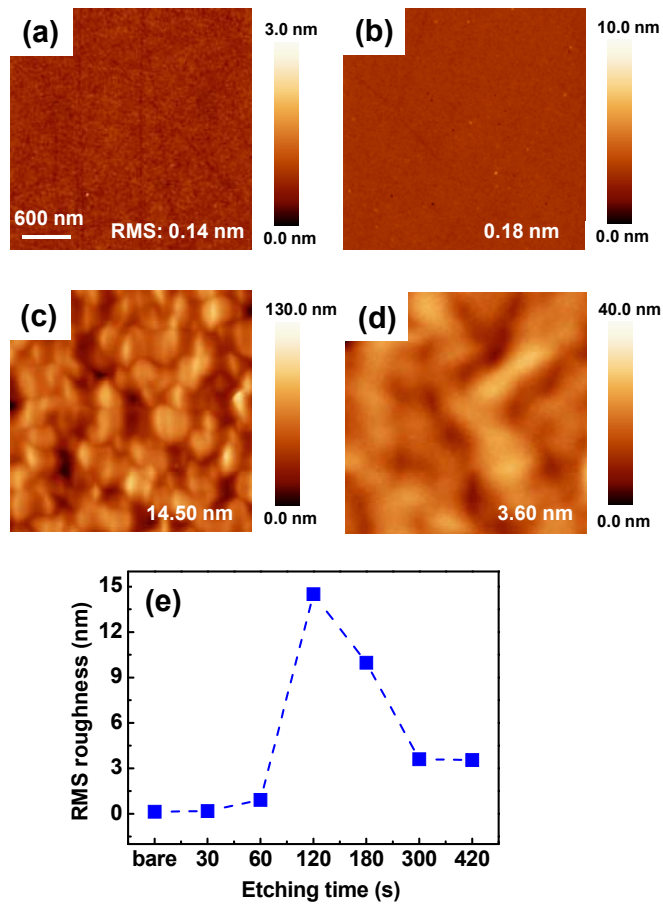


Fig. 3.4. AFM images of InSb surface etched in lactic: nitric acid (10:1) with different etching time (a) 0 sec, (b) 30 sec, (c) 120 sec, (d) 300 sec. (e) A graph of RMS roughness depending on the etching time.

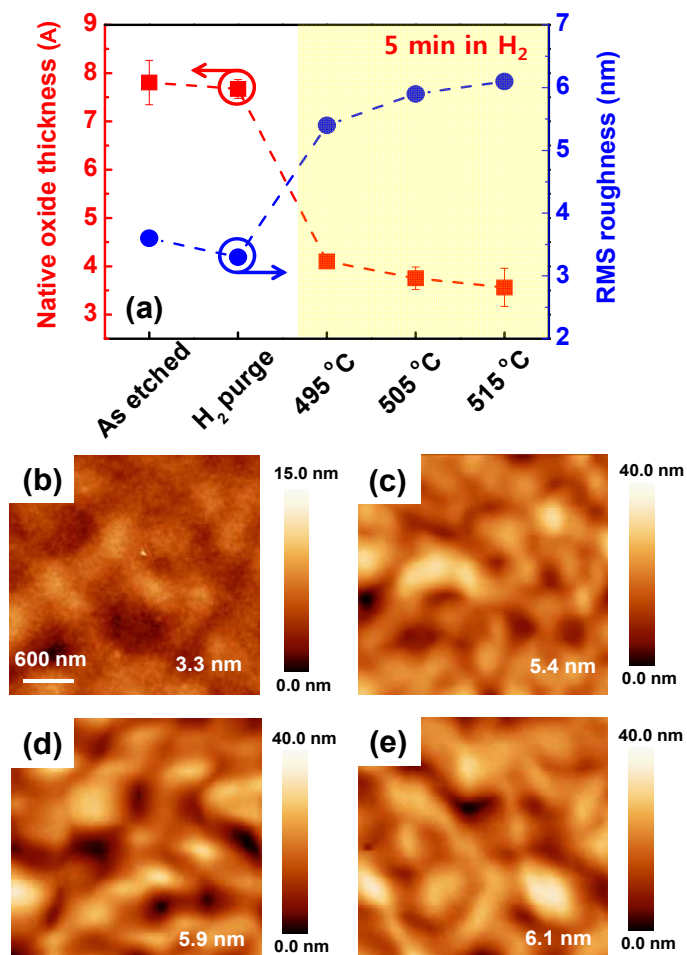


Fig. 3.5. Native oxides thickness and RMS roughness depending on the thermal cleaning temperature and corresponding AFM images of (b) after H<sub>2</sub> purge (c) 495 °C, (d) 505 °C, and (e) 515 °C for 5 min in H<sub>2</sub> ambient

### **3.6. *in-situ* thermal cleaning (TC) of InSb substrate**

#### **3.6.1. H<sub>2</sub> ambient**

##### **3.6.1.1. Effects of TC temperatures on InSb substrate**

The native oxide thickness and surface roughness depending on the TC temperature is represented in Fig. 3.5 (a). As etched InSb sample and rinsed for 30 sec, the thickness of native oxide is 7.8 Å. During the H<sub>2</sub> purge for 20 min, the thickness has not been changed significantly. However, it is significantly decreased up to almost 4.1 Å when the TC was conducted at 495 °C for 5 min. It was gradually decreased with increasing TC temperature to 515 °C. With increasing TC temperatures, surface morphology became rough as shown in Fig. 3.5 (b-e). Just after H<sub>2</sub> purge process, RMS roughness of 3.3 nm was observed, whereas it was significantly increased to 6.1 nm when the sample was thermally cleaned at 515 °C. These results indicated that native oxides thickness and surface morphology was significantly influenced by the applied thermal energy. When a lot of thermal energy was supplied to the sample, native oxides existed on the surface can be desorbed on the surface but rough surface morphology was induced due to the selective desorption.

##### **3.6.1.2. Formation of indium droplets surrounded by rectangular etch pits**

After TC process under H<sub>2</sub> ambient, droplets were observed on the InSb

surfaces. Figure 3.6 (a) illustrates the SEM images of InSb surfaces thermally annealed in H<sub>2</sub> ambient at 515 °C for 5 min which corresponding AFM image is represented in Fig. 3.5 (e). EDS mapping of the sample thermally cleaned at 515 °C was conducted in order to investigate the composition of the droplets. The droplets highlighted with red dotted circles and corresponding EDS mapping images of indium (In) and antimony (Sb) were represented in Fig. 3.6 (b) and (c), respectively. It represented that the composition of droplets were turned out to be an In. In droplets were formed on the InSb surface after thermal annealed under H<sub>2</sub> ambient, indicating that InSb surface was severely damaged by the thermal energy to form the In droplets. The size of In droplet was estimated by 3~4 μm in diameter and its size was dependent on the thermal cleaning temperature and time. With decreasing thermal annealing temperature, the size was decreased to 2 μm when annealed at 495 °C for 5 min. the size was increased to more than 3 times in diameter when the thermal annealing time was increased to 15 min [23].

I also observed rectangular parallelograms around In droplets as illustrated in Fig. 3.6 (a). As I can expect, the formation of rectangular parallelograms was the dependence of thermal annealing temperatures and times. At 495 °C, small size In droplets were formed, resulting in the small sized etch pits formation not rectangular shape this conditions near In droplet. With increasing annealing temperature, more clear etch pits were observed which has some facets bounded by <110> directions. Well defined and much larger rectangular parallelograms were observed when the samples were heated for longer time. The etch figures are bounded and well aligned in the direction of

$\langle 110 \rangle$  when viewed parallel to the  $\langle 100 \rangle$  direction. In order to determine the facet, angles between substrate and facets were investigated using the same samples of 515 °C for 5 min treated as represented in Fig. 3.7 (a). Cleavage direction was represented as A-A'. The angle obtained was 54.4 ° between facet and substrates as shown in Fig. 3.7 (b). Using eq. 3-13, the facet was identified as [24] plane.

$$\cos \theta = \frac{h_1 h_2 + k_1 k_2 + l_1 l_2}{\sqrt{h_1^2 + k_1^2 + l_1^2} \sqrt{h_2^2 + k_2^2 + l_2^2}} \quad [\text{eq. 3-13}]$$

{111} facets were formed due to the polarity effects in zincblende (ZB) structures. In ZB structures, it is known that (110) and (100) exhibits no polarity but (111) shows the polarity which surface is terminated by the In or Sb atoms. Ideally, (100) surface is composed of either In or Sb, however real (100) surfaces consist of both In and Sb atoms, showing non polarity [25]. As a result, the formation of polarity (111) plane was reflected on the InSb surface during thermal annealing. The relative reactivity in ZB-InSb crystal is reported as below [26]:

$$(-111) > (111) \approx (100) > (110)$$

The etch figures were appeared as rectangular parallelograms rather than square when viewed parallel to the  $\langle 100 \rangle$  directions. It is the results of reactivity difference in {111} facets. Sb terminated {111} surface is much more reactivity than that of In terminated {111} surface. Since Sb terminated {111} have more valence electrons, it shows the higher reactivity, resulting in the rectangular etch figures [27].

Figure 3.8 illustrated the process of native oxide desorption and In droplet with rectangular etch pits formation. After native oxides were etched in the mixture of lactic acid and nitric acid, non-uniform native oxides with a thickness of 7.8 Å were re-grown on the InSb surface due to the rinsing in DI water and exposure in air before inserting MOCVD growth chamber (Fig. 3.8. (a)). With increasing thermal annealing temperature, the native oxides were desorbed by the applied thermal energy. The native oxides were desorbed non-uniformly due to the non-uniformity of native oxides thickness and/or lateral variation of the oxides stoichiometry (Fig. 3.8 (b)). A desorption process was the function of thermal cleaning temperature but annealing time was not effective factors. When the InSb surface was exposed as shown in Fig. 3.8 (c), elemental Sb was desorbed from the InSb surface due to the different vapor pressures between In and Sb. Since the vapor pressure of Sb is increased at higher temperature based on the Clausius–Clapeyron equation, preferentially evaporation of Sb from the InSb surfaces was accelerated. As a result, excess In were generated and migrated on the InSb surface to form In droplets. In droplets were collected each others with time the larger ones grow at the expense of the smaller ones to reduce the surface free energy of the island as shown in Fig. 3.8 (d). It is normally called Ostwald ripening process [28]. Due to the thermal energy, rectangular etch pits were also generated surrounded by the In droplets.

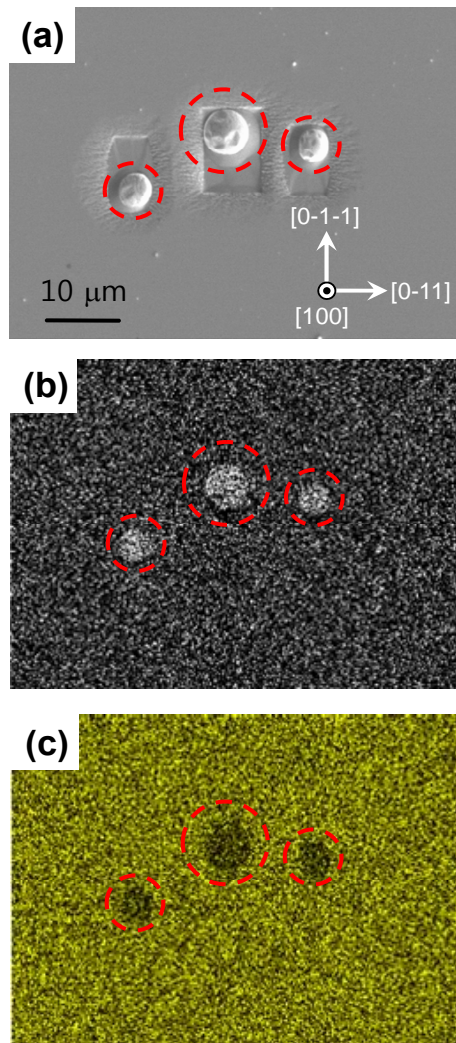


Fig. 3.6. (a) SEM images of InSb surface thermally treated at 515 °C in H<sub>2</sub> ambient. Corresponding EDS mapping images of (b) indium and (c) antimony

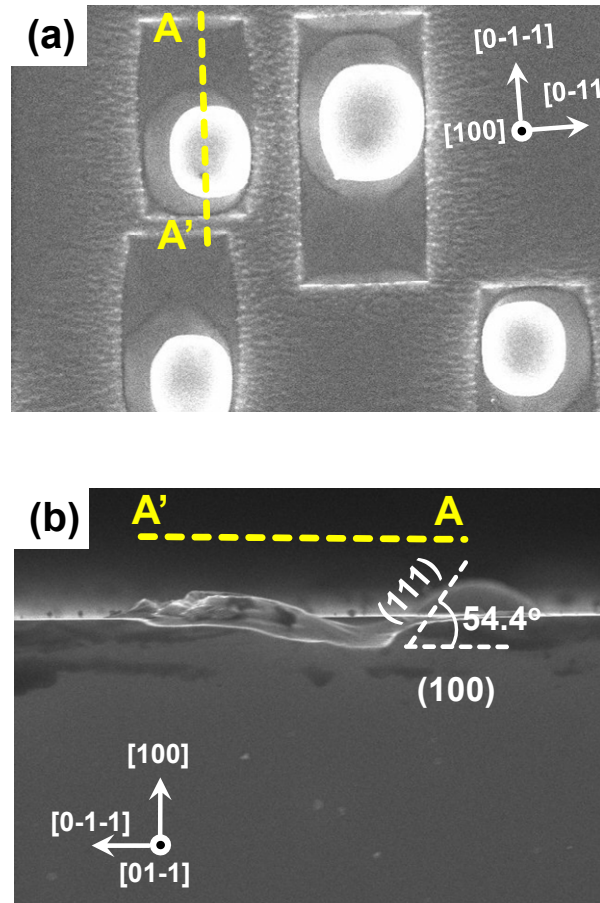


Fig. 3.7. (a) An enlarged SEM images of InSb surface thermally treated at 515 °C in H<sub>2</sub> ambient. (b) XSEM image cleaved by A-A' direction. The angle between (100) and (111) is 54.4°

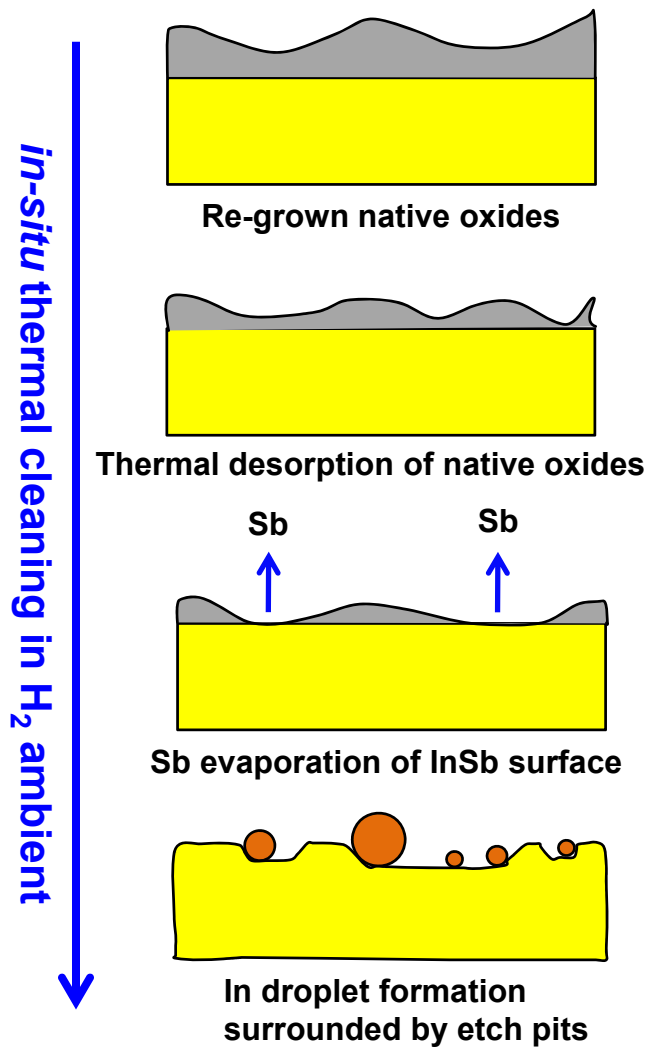


Fig. 3.8. Illustration of native oxide desorption and In droplet formation (a) native oxides re-growth (b) thermal desorption of native oxides (c) Sb evaporation from InSb surface (d) In droplet formation with rectangular etch pits

## **3.6.2. TMSb ambient**

### **3.6.2.1. Effects of TC temperatures on InSb substrate**

Since elemental Sb was evaporated incongruently from InSb surface, In droplets were formed. In order to inhibit the In droplets formation, group V overpressure of trimethylantimony (TMSb) in this experiment was maintained during thermal cleaning process. The formation of In droplets were completely inhibited as shown in Fig. 3.9 (a). SEM image shows that no In droplets on the InSb were formed on the surface when thermally annealed under TMSb mole fraction of 18.1  $\mu\text{mol}/\text{min}$ . The thickness of native oxides on the samples thermally annealed under TMSb ambient was represented with triangle symbol in Fig. 3.9 (b). With increasing TC temperature, the thickness of native oxides has similar thickness of the sample treated under  $\text{H}_2$  ambient, indicating that native oxides was desorbed due to the applied thermal energy. However, RMS roughness was slightly decreased when annealed under TMSb ambient. At 495  $^\circ\text{C}$ , the RMS roughness of 4.6 nm was measured and it was increased to 5.3 nm at 515  $^\circ\text{C}$ . By comparing RMS roughness of the sample treated under  $\text{H}_2$  ambient, the reduction of RMS roughness values was obtained. The slightly decrease of the RMS roughness in the sample treated under TMSb ambient indicates that chemical potential of Sb between gas phases and solid phases was different. Hence insufficient Sb vapor pressure was supplied from gas phase to suppress the evaporation of Sb from the surface.

### **3.6.2.2. Effects of TMSb mole fraction on InSb surface morphology**

A relative rough surface morphology was obtained when 18.1  $\mu\text{mol}/\text{min}$  of TMSb overpressure was maintained. In order to obtain much smooth surface morphology, TMSb molar flow rate was varied from 18.1 to 154.0  $\mu\text{mol}/\text{min}$ . Figure 3.10 (a-d) show the AFM images of InSb surface thermally annealed under TMSb molar flow rate of (a) 18.1, (b) 63.4, (c) 108.7, and (d) 154.0  $\mu\text{mol}/\text{min}$ . When the low TMSb molar flow rate was applied, large features were observed with rough surface morphology and smooth surface morphology with RMS roughness of 1.1 nm was obtained with increasing TMSb molar flow rate to 108.7  $\mu\text{mol}/\text{min}$ . At TMSb molar flow rate of 154.0  $\mu\text{mol}/\text{min}$ , RMS roughness was slightly increased to 2.1 nm. The corresponding surface morphology line profile was represented in Fig. 3.10 (e).

From the illustration of chemical potential difference of Sb between gas phases and InSb surface in Fig. 3. 11, this surface morphology depending on the TMSb flow rate was explained. At TMSb flow rate of 18.1 and 63.4  $\mu\text{mol}/\text{min}$ , chemical potential of Sb from InSb surface was higher than that of Sb in the gas phases, showing rough surface morphology due to Sb desorption at a given annealing temperature. This was explained in Fig. 3.11 (a). As shown in Fig. 3.11 (b), the chemical potential of two phases are

almost balanced by increasing TMSb molar flow rate to 108.7  $\mu\text{mol}/\text{min}$ , smooth surface morphology was obtained by inhibiting the Sb desorption. When the excess TMSb was supplied at a flow rate of 154.0  $\mu\text{mol}/\text{min}$ , gas phase of Sb can affect to surface morphology change due to the low vapor pressure of Sb as shown in Fig. 3.11 (c). This effect was confirmed by Raman spectroscopy measurements as shown in Fig. 3.12. In the TMSb molar flow rate ranges between 18.1 and 108.7  $\mu\text{mol}/\text{min}$ , only two InSb phonon mode was observed at 191 and 180  $\text{cm}^{-1}$ , respectively. These were contributed by the InSb longitudinal phonon mode (LO) and transverse phonon mode (TO). However, two Sb related phonon modes of Sb ( $A_{1g}$ ) and Sb ( $E_g$ ) were observed in the InSb sample thermally treated under TMSb ambient with a flow rate of 154.0  $\mu\text{mol}/\text{min}$ . It represents that Sb induced from gas phase were condensed on the InSb surface, producing Sb related Raman phonon peak. As a result, relatively smooth surface morphology was observed as shown in Fig. 3. 10 (e). When the small amount of Sb was presented on InSb surfaces, Raman measurements can detect it due to the Sb resonance effects.

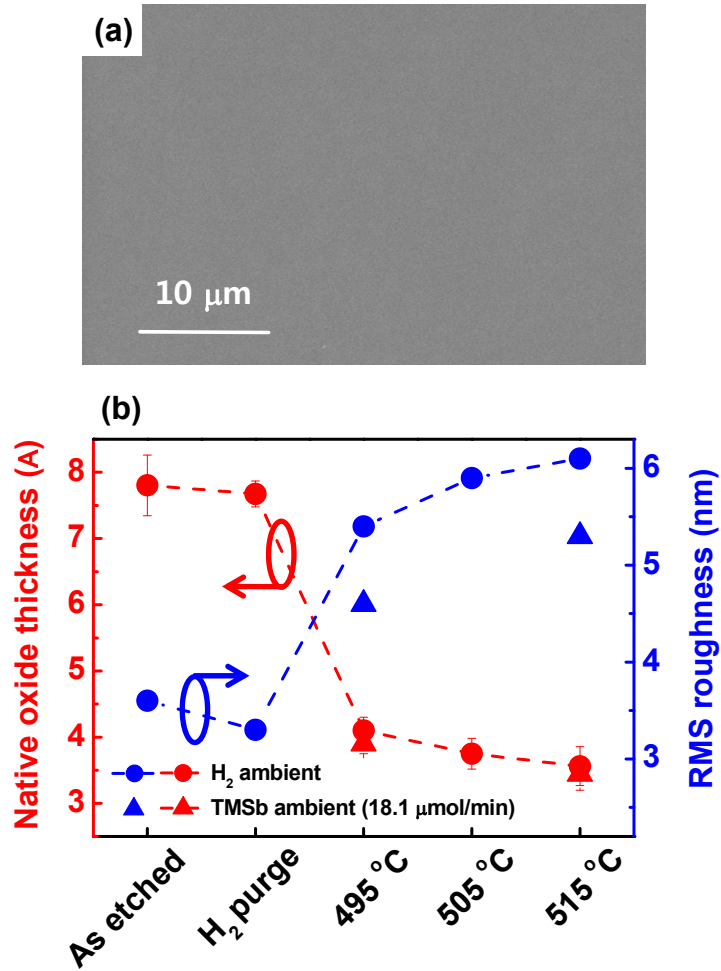


Fig. 3.9. (a) SEM image of InSb thermally annealed at 515 °C for 300 sec (TMSb molar flow rate= 18.1 μmol/min) (b) Native oxide thickness and corresponding RMS roughness of InSb substrates thermally annealed at 495 °C and 515 °C. A data obtained H<sub>2</sub> ambient were included for the comparison.

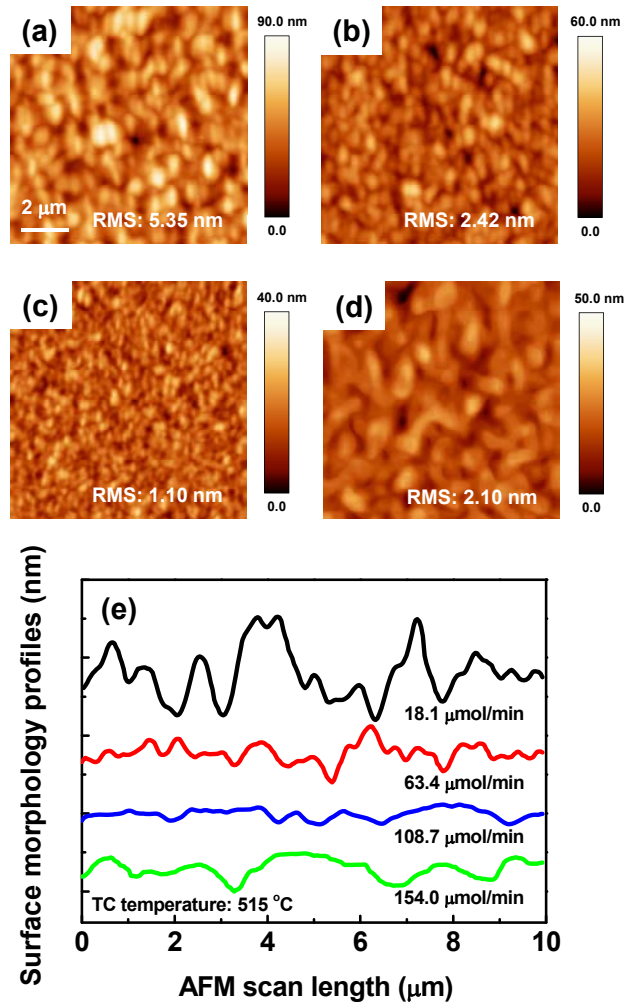


Fig. 3.10. AFM images of InSb annealed under different TMSb molar flow rate of (a) 18.1, (b) 63.4, (c) 108.7, and (d) 154.0  $\mu\text{mol/min}$  and (e) its corresponding surface line profiles.

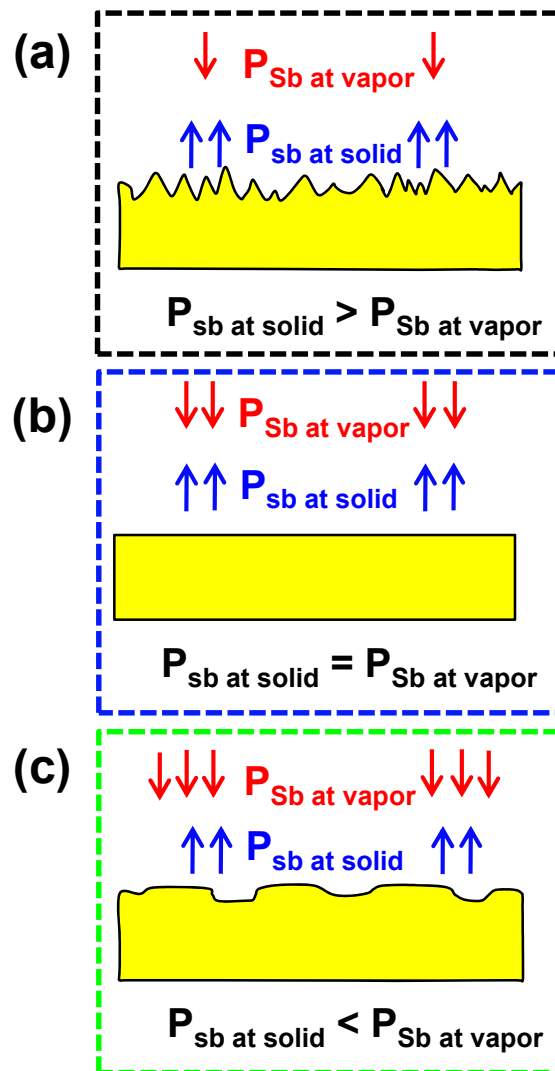


Fig. 3.11. Illustration of chemical potential of Sb between gas phases (vapor) and substrate surface (solid) (a)  $P_{Sb \text{ at solid}} > P_{Sb \text{ at vapor}}$  (b)  $P_{Sb \text{ at solid}} = P_{Sb \text{ at vapor}}$  (c)  $P_{Sb \text{ at solid}} < P_{Sb \text{ at vapor}}$

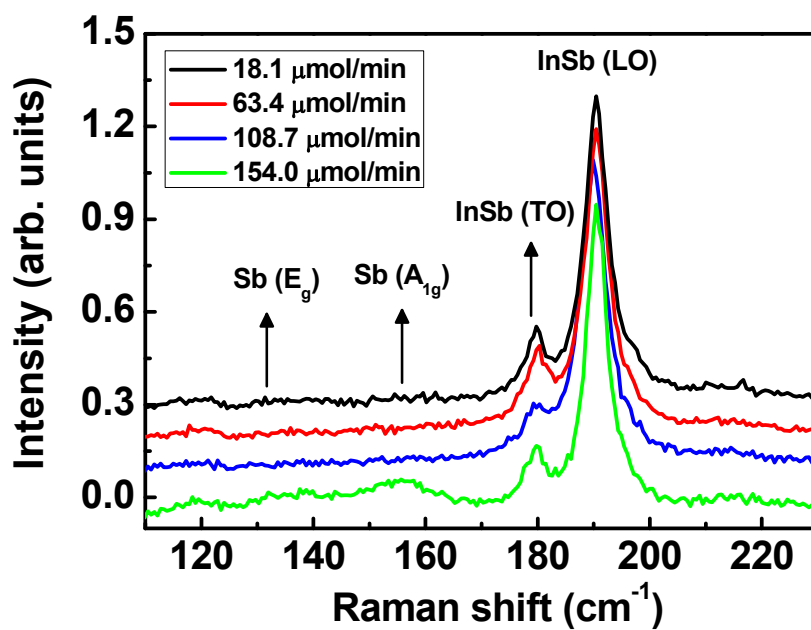


Fig. 3.12. Raman results of InSb samples thermally treated under TMSb ambient. TMSb molar flow rate was varied from 18.1 to 154.0  $\mu\text{mol}/\text{min}$ .

## **3.7. Effects of thermal cleaning ambient on the quality of InSb epilayers**

### **3.7.1. Influence on the crystallinity**

Figure 3.13 (a) shows the high resolution X-ray rocking curve (XRC) of InSb epilayers. When InSb epilayers grown on InSb substrates thermally cleaned under H<sub>2</sub> ambient, full width at half maximum (FWHM) of 19.3 arcsec was obtained. On the other hand, the FWHM of InSb layers grown on InSb substrates thermally cleaned under optimized TMSb ambient was reduced to 10.5 arcsec, implying that, as a result of TMSb overpressure, the crystal quality of InSb epitaxial layer was improved. In addition, XRD measurement of the bare InSb substrates before and after the TC has been done. All of them showed a similar FWHM value of 34 arcsec, which is larger than those of the InSb epitaxial layers. This indicates that the x-ray information of InSb substrate effects on the x-ray rocking curve negligibly. In order to investigate the origin of the broadening of x-ray rocking curve for the sample grown after the TC under H<sub>2</sub> ambient, we performed the reciprocal space mapping (RSM) measurement for the two InSb epitaxial layers. Figure 3.13 (b, c) show the the RSM results of (004) reflection for the two InSb epitaxial layers grown after TC under (b) H<sub>2</sub> (c) TMSb ambient, respectively. The maps were represented in reciprocal lattice units (rlu) with the horizontal axis representing the in-plane scattering vector components ( $Q_x$ ) and the vertical axis representing the scattering vector component ( $Q_y$ ) perpendicular to the epitaxial layer surface. The counter levels of the

horizontal and the vertical scales were kept equal for all the maps. Both mapping of the InSb layers show only one peak of an InSb (004) reciprocal point, which implies that there is no extra materials included in the InSb layers. RSM of the InSb layers grown after TC under H<sub>2</sub> ambient shows that the (004) Bragg spot is somewhat elongated along the Q<sub>x</sub> axis in the reciprocal space as shown in Fig. 3.13 (b). This implies that a crystal quality of the InSb layer grown after TC under H<sub>2</sub> ambient could be degraded by the formation of mosaic structures. It is assumed that this mosaic structure was induced by the growth interference due to the In droplets formed on the InSb (001) surface during the TC under H<sub>2</sub> ambient. In contrary, RSM of the InSb layer grown after TC under TMSb ambient shows an almost circular shaped peak, indicating that high quality of InSb epilayers can be grown as shown in Fig. 3.13 (c).

### **3.7.2. Origin of the degraded quality of InSb epilayers**

As described in the Sec. 3.7.1, crystallinity of InSb epilayers was degraded when it was grown on the InSb substrate thermally annealed under H<sub>2</sub> ambient. The origin of degradation was investigated using low temperature photoluminescence (PL) measurement as shown in Fig. 3.14. Four PL peaks were observed and each peak was denoted from #1 to #4. More detailed explanation of each peak was represented in the chapter 4. The peak #1 was originated from near band edge emission [29, 30]. The peak of #1 was located at a different position. The PL peak of InSb epitaxial layer grown on InSb substrate under H<sub>2</sub> ambient was shifted toward lower emission energy

and the peak intensity was decreased. It implies that point defects were introduced into the InSb epitaxial layer and consequently the film quality was degraded. When InSb was grown under In-rich growth condition, donor type of defects was incorporated into InSb epitaxial layers. This donor defect shows the positive charges due to the ionization and was positioned below conduction band edge, interacting with conduction band electrons. The conduction band edge was fluctuated by the interaction, introducing red shift of PL emission. More detailed and systematic investigation was introduced in chapter 4.

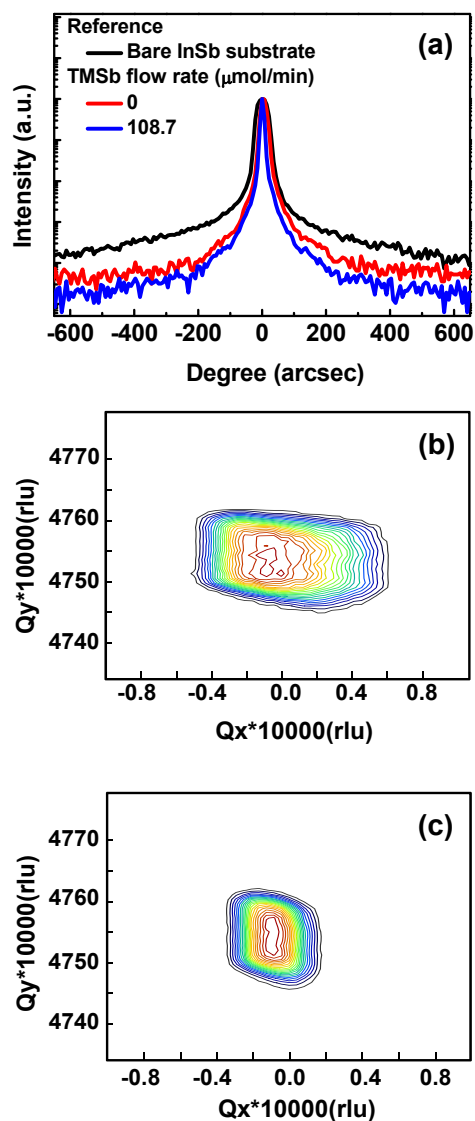


Fig. 3.13. X-ray rocking curve of InSb epitaxial layers grown on InSb substrates thermally treated under either H<sub>2</sub> or TMSb ambient. Reciprocal space mapping results of (004) reflection for the two InSb epitaxial layers grown on the substrate annealed under (b) H<sub>2</sub> and (c) TMSb ambient, respectively.

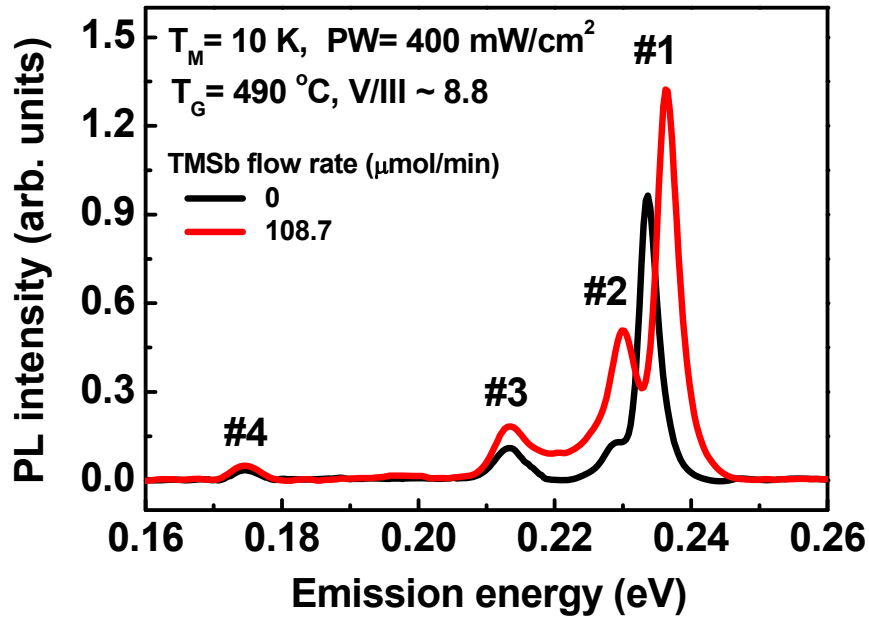


Fig. 3.14. Photoluminescence of InSb epilayers grown on InSb substrate thermally treated under  $\text{H}_2$  and TMSb ambient. The PL emission was obtained at 10 K with a power density of 400 mW.

### 3.8. Summary

I investigated the cleaning of InSb substrate for high quality of epitaxial layer growth using MOCVD. First, initial native oxides of InSb were removed by dipping in optimized wet chemical etchant. The thickness of native oxides was effectively removed by controlling the ratio of the etchant. At non-optimized ratio of etchant, the native oxides became thicker and thicker with increasing etching time and sometimes the surface can be burned when the oxidizer ratio was increased. Then the samples were *in-situ* annealed in the growth chamber with different ambient condition. In case of H<sub>2</sub> ambient, native oxides became thinner and thinner with increasing thermal cleaning (TC) temperature up to 515 °C. However, rough surface morphology was observed due to the applied thermal energy. In this ambient, In droplets surrounded by rectangular etch pits were formed on the surface. In case of TMSb ambient, the formation of In droplets with etch pits were completely inhibited by applied Sb. As a result, surface morphology became smooth and the lowest RMS roughness of 1.1 nm was measured when enough TMSb was applied to suppress the evaporation of Sb from the surface. InSb surface treatment under TMSb ambient influenced on the crystal quality of InSb epilayers. I found that In interstitial defects were incorporated into InSb epilayers when InSb substrates were annealed under H<sub>2</sub> ambient. Induced In droplets may be the source of excess In that can be incorporated in InSb epilayers. Excess In can produce point defects, affecting the crystal quality degradation.

### 3.9. Bibliography

- [1] C. Wilmsen, *Physics and chemistry of III-V compound semiconductor interfaces*: Springer Science & Business Media, 2013.
- [2] R. Biefeld, "The growth of InSb using alternative organometallic Sb sources," *Journal of crystal growth*, vol. 128, pp. 511-515, 1993.
- [3] P. Chiang and S. Bedair, "Growth of InSb and InAs<sub>1-x</sub>Sb<sub>x</sub> by OM-CVD," *Journal of The Electrochemical Society*, vol. 131, pp. 2422-2426, 1984.
- [4] M. Razeghi, "Overview of antimonide based III-V semiconductor epitaxial layers and their applications at the center for quantum devices," *The European Physical Journal Applied Physics*, vol. 23, pp. 149-205, 2003.
- [5] E. Ahn, Y. Lee, J. Kim, E. Yoon, and Y. Kim, "In-situ monitoring of InAs/GaAs QDs by using spectral reflectance," *JOURNAL-KOREAN PHYSICAL SOCIETY*, vol. 49, p. 947, 2006.
- [6] S. Fujieda, M. Mizuta, and Y. Matsumoto, "Improvement of the Electrical Properties of the AlN/GaAs MIS System and Their Thermal Stability by GaAs Surface Stoichiometry Control," *Japanese journal of applied physics*, vol. 27, p. L296, 1988.
- [7] Y.-D. Kim, T.-W. Lee, H. Hwang, Y. Moon, E. Yoon, and F. Nakamura, "Analysis of surface photoabsorption spectra of (001) InP surfaces," *Japanese journal of applied physics*, vol. 38, p. 5033, 1999.
- [8] R. M. Biefeld, "The metal-organic chemical vapor deposition and properties of III-V antimony-based semiconductor materials,"

*Materials Science and Engineering: R: Reports*, vol. 36, pp. 105-142, 2002.

- [9] O. Sugiura, H. Kameda, K. Shiina, and M. Matsumura, "Low-temperature growth of InSb by vacuum MOCVD using TEIn and SbH<sub>3</sub>," *Journal of electronic materials*, vol. 17, pp. 11-14, 1988.
- [10] R. M. Biefeld, "The preparation of InSb and InAs  $1-x$  Sb  $x$  by metalorganic chemical vapor deposition," *Journal of Crystal growth*, vol. 75, pp. 255-263, 1986.
- [11] Y. Choi, R. Sudharsanan, C. Besikci, E. Bigan, and M. Razeghi, "High-Quality InSb Growth on GaAs and Si by Low-Pressure Metalorganic Chemical Vapor Deposition," in *MRS Proceedings*, 1992, p. 375.
- [12] S. Jha, M. K. Wiedmann, and T. Kuech, "A comparative precursor study of the growth behavior of InSb using metal-organic vapor phase epitaxy," *Journal of Crystal Growth*, vol. 315, pp. 87-90, 2011.
- [13] R. M. Biefeld and J. D. Phillips, "Growth of InSb on GaAs using InAlSb buffer layers," *Journal of crystal growth*, vol. 209, pp. 567-571, 2000.
- [14] M. Behet, B. Stoll, W. Brysch, and K. Heime, "Growth of GaSb and InSb by low-pressure plasma MOVPE," *Journal of crystal growth*, vol. 124, pp. 377-382, 1992.
- [15] M. Behet, B. Stoll, and K. Heime, "Comparative study on the low pressure metalorganic vapor phase epitaxial growth of InSb on GaAs with trimethylantimony and triethylantimony as Sb precursors," *Journal of crystal growth*, vol. 135, pp. 434-440, 1994.
- [16] Y. Choi, C. Besikci, R. Sudharsanan, and M. Razeghi, "Growth of

- In<sub>1-x</sub>Tl<sub>x</sub>Sb, a new infrared material, by low-pressure metalorganic chemical vapor deposition," *Applied physics letters*, vol. 63, pp. 361-363, 1993.
- [17] N. Jones, C. Norris, C. Nicklin, P. Steadman, J. Taylor, C. McConville, *et al.*, "An X-ray diffraction study of oxide removal from InSb (001) substrates," *Applied surface science*, vol. 123, pp. 141-145, 1998.
- [18] J. Klem, J. Tsao, J. Reno, A. Datye, and S. Chadda, "Thermal desorption of InSb surface oxides," *Journal of Vacuum Science & Technology A*, vol. 9, pp. 2996-2998, 1991.
- [19] M. A. Herman, W. Richter, and H. Sitter, *Epitaxy: physical principles and technical implementation* vol. 62: Springer Science & Business Media, 2004.
- [20] D. R. Gaskell, *Introduction to the Thermodynamics of Materials*: CRC Press, 2008.
- [21] I. Vermeir, W. Gomes, and P. Van Daele, "Some fundamental aspects of profile etching at InP surfaces," *Journal of The Electrochemical Society*, vol. 142, pp. 3226-3232, 1995.
- [22] P. Bandaru and E. Yablonovitch, "Semiconductor surface-molecule interactions wet etching of InP by  $\alpha$ -hydroxy acids," *Journal of The Electrochemical Society*, vol. 149, pp. G599-G602, 2002.
- [23] S. Park, J. Jung, C. Seok, K. W. Shin, S. H. Park, Y. Nanishi, *et al.*, "Effects of TMSb overpressure on InSb surface morphology for InSb epitaxial growth using low pressure metalorganic chemical vapor deposition," *Journal of Crystal Growth*, vol. 401, pp. 518-522, 2014.
- [24] D. M. Zhernokletov, H. Dong, B. Brennan, J. Kim, and R. M. Wallace,

- "Optimization of the ammonium sulfide (NH<sub>4</sub>)<sub>2</sub>S passivation process on InSb (111) A," *Journal of Vacuum Science & Technology B*, vol. 30, p. 04E103, 2012.
- [25] H. C. Gatos and M. C. Lavine, "Etching Behavior of the {110} and {100} Surfaces of InSb," *Journal of The Electrochemical Society*, vol. 107, pp. 433-436, 1960.
- [26] M. Lavine, A. Rosenberg, and H. Gatos, "Influence of crystal orientation on the surface behavior of InSb," *Journal of Applied Physics*, vol. 29, pp. 1131-1132, 1958.
- [27] H. C. Gatos and M. C. Lavine, "Characteristics of the {111} Surfaces of the III-V Intermetallic Compounds," *Journal of the Electrochemical Society*, vol. 107, pp. 427-433, 1960.
- [28] M. Ohring, *Materials science of thin films*: Academic press, 2001.
- [29] A. Mooradian and H. Fan, "Recombination emission in InSb," *Physical Review*, vol. 148, p. 873, 1966.
- [30] J. Pehek and H. Levinstein, "Recombination radiation from InSb," *Physical Review*, vol. 140, p. A576, 1965.

# Chapter 4. Growth and characterization of InSb epitaxial layers

## 4.1. Introduction

Opto-electronic devices are an interesting device of electronics that combines both electronics and optics. There are two types of devices in principles. When the devices are exposed to incident light energy or photon, the devices produce electrical energy. Sensors and solar cells are included in this category. On the other hand, in case of light emitting diodes (LEDs), the material emits the light when the electrical energy is applied to the materials. In both cases, electrical and optical energy can be used for the operation of devices, so called opto-electronic devices.

In order to operate the opto-electronic devices, both electrical and optical properties are very important, which affect to the device performances. For example, InSb, a major material used in this thesis, is a suitable material of IR PDs detecting for MWIR ranges. As mentioned in the chapter 1, it has not only narrowest band-gap energy, which is related to the optical adsorption wavelength but also superior electron effective mass ( $m_e^*$ ) among other III-V semiconductors that contribute to increase mobility of the material. For a comparison,  $m_e^*$  of InSb and some other III-V semiconductor are represented in table 4.1. Consequently, high speed IR PDs can be fabricated using the material with smaller  $m_e^*$ . The  $m_e^*$  can be deduced from the band

diagram of InSb as shown in Fig. 4.1. From the curvature of the band at E-K diagram,  $m^*$  can be determined from the inverse second derivative of the band, producing equation 4-1 [1].

$$m^* = \hbar^2 \left( \frac{\partial^2 E}{\partial k^2} \right)^{-1} \quad [\text{eq. 4-1}]$$

It clearly represents that the  $m^*$  is much smaller in the direct  $\Gamma$  conduction band (strong curvature) than in the X or X valley, which have weaker curvature in Fig. 4.1.

However, electron and hole mobility are influenced by the scattering due to the lattice and impurity [1]. In lattice scattering a carrier moving through the crystal is scattered by a vibration of the lattice that is a function of temperature. This is dominant mechanism at higher temperature. On the other hand, scattering from impurity in the crystal such as ionized impurities became dominant mechanism at lower temperature regions. Since the lattice atoms in the lower temperature are less agitated, carriers are likely to be scattered more strongly by an interaction with a charged impurity. It implies that we have to know the information of impurities presenting in the materials for the application of high speed and performance opto-electronic devices.



## 4.2. Motivation

In order to investigate the impurities in materials, many techniques such as temperature dependent Hall measurements, adsorption, deep level transient spectroscopy (DLTS), photoluminescence (PL) etc were developed and proposed. Among them, PL is one of the most extensively used spectroscopic techniques due to the easy and non-destructive method. It provides the information of radiative recombination process as well as residual defects in a material. However, PL measurements for defects characterization of InSb has not been widely carried out as successful as other III-V semiconductors although it has been started from 1950's [2, 3]. There are two primary obstacles that have limited PL analysis of defects in InSb [4]. It has the smallest effective mass among all III-V binary semiconductors, which results in a very small donor Mott concentration ( $n \sim 6 \times 10^{13} \text{ cm}^{-3}$ ). Consequently, shallow donor levels are significantly broadened and even merged with conduction band that make it difficult to identify the defect states in InSb materials. Another obstacle is the smallest band-gap energy of InSb which presents difficulties for PL measurements. Photons from room temperature blackbody radiation, having similar energies to the InSb PL, generate noise in the detector and consequently influence on the dramatically reduce the signal to noise (S/N) ratio and high resolution PL measurements is not feasible. Due to the difficulties of InSb characterization via PL measurement, limited numbers of InSb investigation using PL analysis method have been performed.

Since a room temperature PL measurement of bulk InSb conducted by

Moss *et al.* in 1956, the PL studies of bulk n-and p-type InSb were performed at various temperatures to identify the origin of PL emissions [3, 5, 6]. Through these studies, PL emissions associated with band to band transitions, transitions created by an optical phonon as well as transitions involving acceptor impurities such as zinc, silver, germanium and gold were identified. The effect of applied magnetic field and electric field during PL measurement was also studied [4, 6]. Bound exciton of InSb at 231.1 meV was observed in the InSb PL spectrum measured at 5.1 K. It was originated from the acceptor-bound excitation transition under zero magnetic field [7]. PL measurements of homo- and hetero-epitaxial InSb layers grown by metal organic chemical vapor deposition (MOCVD) [8, 9] and molecular beam epitaxy (MBE) [10, 11] under an optimized growth condition were performed. All PL spectra of homo-epitaxial InSb layer showed the same PL spectra of bulk InSb. On the other hand, only single broad PL spectrum of band to band transition was observed and shifted toward higher emission energy for the InSb sample grown on GaAs substrate. These were ascribed either to residual strains in the InSb layers or to a rise in carrier concentration induced by electrically active dislocations at InSb/GaAs interfaces [10, 11].

Until now, in order to growth high quality of InSb epilayers, growth conditions have to be optimized and the effects of growth parameters on InSb epilayers have to be investigated as a fundamental study.

### 4.3. Experimental procedures

In order to growth high quality of unintentionally doped InSb under optimized growth conditions, growth parameters such as growth temperature ( $T_G$ ) and V/III ratio was varied. Basic growth condition and analysis condition was mentioned in the chapter 2. In this chapter,  $T_G$  was changed from 450 to 510 °C and V/III ratio was varied from 2.2 to 13.2 with different MO source supply. TMIn mole fraction was varied from 2.47 to 4.94  $\mu\text{mol}/\text{min}$  and TMSb mole fraction was changed from 18 to 72  $\mu\text{mol}/\text{min}$ .

For the growth of p-InSb, diethylzinc (DEZn) was used as a p-type dopant. To obtain hole concentration for the IR PDs fabrication, like unintentionally doped InSb, the effect of DEZn mole fraction and  $T_G$  on the hole concentration was investigated by changing DEZn mole fraction from 0.144 to 1.22  $\mu\text{mol}/\text{min}$ . The same  $T_G$  range was used.

When the growth rate of InSb grown on InSb substrate was measured, dummy InSb wafer was used to identify the thickness of InSb epilayers and surface profiler was used to measure it. The schematic diagram and measured the thickness of InSb epilayers are represented in Fig. 4.2 (a) and (b).

Since InSb has no semi-insulating substrate, causing the difficulties in the electrical measurements. During the Hall measurements of unintentionally doped and Zn doped InSb, p-type with a carrier concentration of  $10^{18} \text{ cm}^{-3}$  and n-type substrates were used to growth its InSb epilayers on them, respectively.

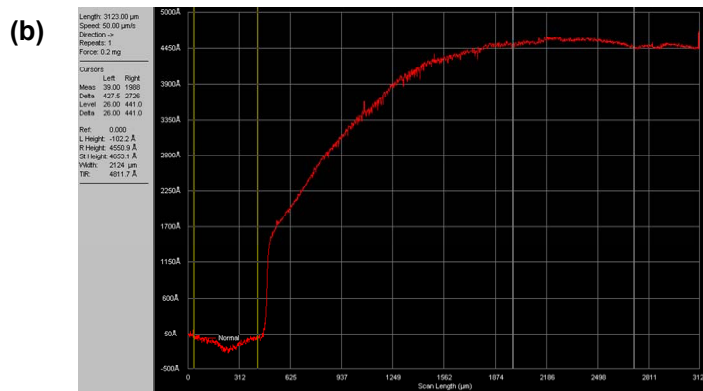
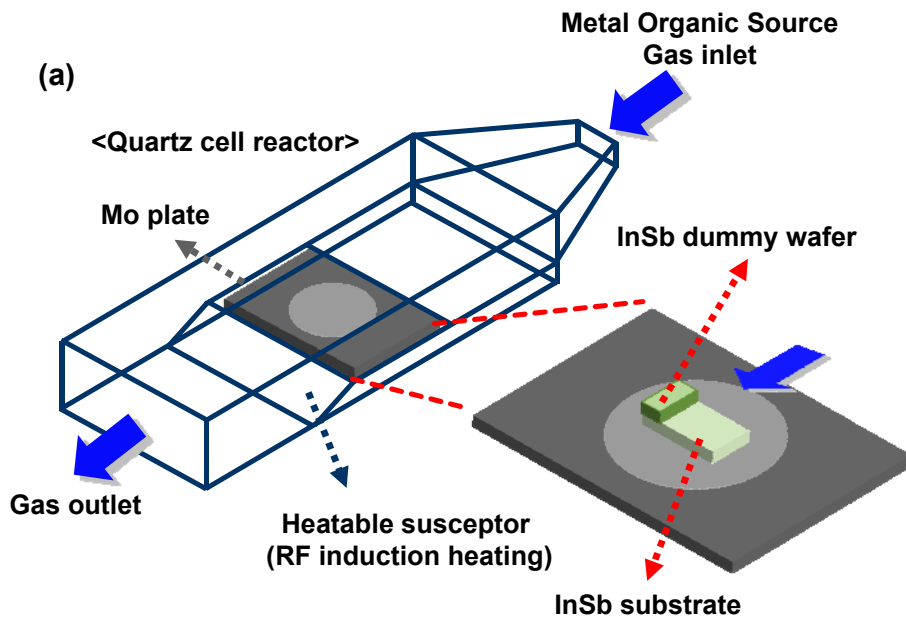


Fig. 4.2. (a) A technique for growth rate measurements and (b) its result measured surface profiler

## **4.4 Epitaxial growth of unintentionally doped InSb**

### **4.4.1. Effects of growth parameters on InSb surface morphologies**

In order to find optimized growth conditions of InSb, the effect of V/III ratio and growth temperature ( $T_G$ ) was investigated. From the AFM images of InSb epilayers as shown in Fig. 4.3, all InSb epilayer has smooth surface morphology with a RMS roughness of less 1 nm, except the InSb samples with indium (In) droplets. At low V/III ratio of 2.2 in all  $T_G$  ranges, rough surface morphology was observed compared to that of InSb grown at other V/III ratio. Especially, at low  $T_G$  in the ranges between 450 and 470 °C, In droplets were formed on the InSb surface. However, In droplets were removed with increasing V/III ratio up to 13.2. However, smooth surface morphology at V/III ratio of 2.2 was observed when InSb were grown at relatively higher  $T_G$  over 490 °C. In this  $T_G$  ranges, smooth surface morphology was observed in all investigated V/III ratio. This rough surface morphology is similar to the results for GaAs and GaP [12-14].

Surface roughness can be normally explained by a combination of factors which include preferential nucleation, surface diffusion, substrate preparation, substrate defects, vapor phase composition and surface reactions [15]. In our case, the surface morphology of InSb grown different V/III ratio was influenced by vapor phase composition. At V/III ratio of 2.2, more In atoms were diffused to the growth surface through boundary layer, resulting in the

In-rich InSb growth surface. As a result, extra In atoms which was not participated in the growth, can be merged together, forming large sized In droplets on the surface. With increasing V/III ratio, more Sb atoms were supplied to the growth surface, content of two sources can be balanced each other to form stoichiometric InSb epilayers. Smooth surface morphology was observed with increasing  $T_G$  from 490 °C, even at V/III ratio of 2.2. Based on the explanation of In droplet removal with increasing V/III ratio, more Sb atoms were supplied to the InSb growth surface, resulting in the removal of In droplets. It was reported that TMSb was not fully decomposed in this  $T_G$  ranges [16]. At a fixed V/III ratio, the decomposition of TMSb was increased with increasing  $T_G$ , and extra Sb atoms were supplied to balance the amount of two sources. At V/III ratio of 8.8, the surface morphology became smooth with increasing  $T_G$ . It was caused by the increase of surface diffusion length of ad-atoms on the surface. If the surface diffusion was too slow to find the step edge sites for the reduction of surface energy, the preferential nucleation was occurred on the surface, generating rough surface morphologies as shown in Fig. 4.3.

#### **4.4.2. Effects of growth parameters on InSb crystallinity**

I observed that crystallinity of InSb epilayer was influenced by the growth parameters. Crystallinity was evaluated by the X-ray Rocking Curve (XRC) measurement as shown in Fig. 4.4. With changing V/III ratio from 2.2 to 13.2 under  $T_G$  of 490 °C, the broad full width at half maximum (FWHM) of 12.11 arcsec was obtained at V/III ratio of 2.2. It was gradually decreased to 11.1 arcsec at V/III ratio of 8.8 then slightly increased with increasing V/III ratio

to 13.2. When the  $T_G$  was varied from 450 to 510 °C at a fixed V/III ratio of 8.8, the same trend of FWHM dependence was observed. At 450 °C, FWHM of 13.33 arcsec was observed and gradually decreased with increasing  $T_G$  up to 490 °C. It was increased to 11.94 arcsec at  $T_G$  of 510 °C. The result of crystallinity with a dependence of growth parameters implies that there might be an incorporation of unknown impurities into InSb epilayers during growth which caused by the non-stoichiometric growth conditions. Based on the crystallinity and surface morphologies of InSb epilayers grown by different growth parameters, optimized growth condition in this MOCVD system was determined that V/III ratio turned out to be 8.8 under  $T_G$  of 490 °C. In-rich growth condition was observed below V/III ratio of 8.8, whereas slightly Sb-rich growth condition was observed over V/III ratio of 8.8. Due to the incomplete decomposition of TMSb sources,  $T_G$  ranges below 490 °C can be In-rich growth condition and maybe Sb-rich growth condition was established at 510 °C.

#### **4.4.3. Growth behavior of InSb grown using TMIn and TMSb**

The growth rate of InSb was measured over a broad range of  $T_G$ , group III precursor mole fraction and group V precursor mole fraction for TMIn/TMSb growth chemistry. The  $T_G$  was varied from 450 to 510 °C while the both reactant mole fractions were held constant with V/III ratio of 8.8 to determine the temperature dependence of the growth rate as shown in Fig 4.5 (a). In the  $T_G$  ranges, the growth rate showed the strong temperature dependence where the growth rate was exponential dependence with  $T_G$ , that is called kinetically limited growth behavior. It implies that the growth of InSb using TMIn and

TMSb was thermally activated over this  $T_G$  ranges. The apparent activation energy, measured from the slope of the Arrhenius plot of the growth rate, was 13.6 kcal/mol. For comparison, apparent activation energy of 14 kcal/mol using the same source combinations used in this study [15, 17]. The differences of apparent activation energy values may be caused by the different reactor geometry, which influence on the extent of the temperature dependent reactions. Therefore, these apparent activation energy is a combination of the temperature dependence of the concurrent processes of gas and surface reactions and the interaction of the reactions with the fluid flow environment within the reactor governing factors such as wall depositions and gas phase temperature [18].

The growth rate was determined over a range of group III mole fraction with the TMIn mole fraction ( $MF_{TMIn}$ ) varying from 2.47 to  $4.94 \times 10^{-6}$  mol/min for the TMIn/TMSb growth chemistries at a constant TMSb mole fraction ( $MF_{TMSb}$ ) of  $36.0 \times 10^{-6}$  mol/min as shown in Fig. 4.5 (b). The dependence of source materials mole fraction on the growth rate was investigated at a constant  $T_G$  of 490 °C. The dependence of TMIn on growth rate exhibited a linear relationship between the growth rate and  $MF_{TMIn}$ .

The effects of group V mole fraction, at a constant group III mole fraction, on the growth rate showed the independently relationship as shown in Fig. 4.5 (c). In this investigated TMSb mole fraction ranges ( $MF_{TMSb}$ ),  $MF_{TMSb}$  was varied from 18.0 to  $72.0 \times 10^{-6}$  mol/min during keeping  $MF_{TMIn}$  of  $4.12 \times 10^{-6}$  mol/min. The accessible range of applied source mole fractions for these growth chemistries was limited by the formation of In droplets at high group

III mole fractions. From the observed results clearly suggest that the InSb growth rate is controlled by the lack of absorbed In species on the surface reacting with the absorbed Sb to form InSb. It represents that the growth surface was saturated by Sb species with low In surface coverage.

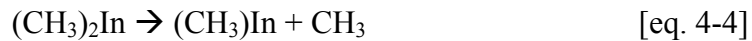
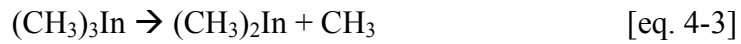
Based on these results, a simple bimolecular Langmuir-Hinshelwood type mechanism is proposed for InSb growth using TMIn and TMSb precursors chemistries, analogous to the growth of GaSb [19].

$$R_{InSb} = \frac{k_{InSb} K_{In} K_{Sb} P_{TMIn} P_{TMSb}}{(1 + K_{In} P_{TMIn})(1 + K_{Sb} P_{TMSb})} \quad [\text{eq. 4-2}]$$

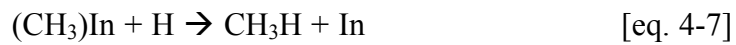
where  $k_{InSb}$  is the rate constant for the surface reaction between the absorbed species,  $K_{In}$  and  $K_{Sb}$  are the equilibrium constants for the adsorption of the dominant In and Sb species arriving at the surface, and  $P_{TMIn}$  and  $P_{TMSb}$  are the partial pressures of the precursors introduced in the gas phases in the chamber which was residual amount of partial pressure of each precursors that total amount of precursors introduced into the deposition chamber minus what is lost due to the parasitic reaction between two precursors and the deposition of solid on the reactor chamber walls. In this model, a high  $MF_{TMSb}$  would lead to a high Sb surface coverage ( $K_{Sb} P_{TMSb} \gg 1$ ), introducing a weak or negligible growth rate dependence on  $MF_{TMSb}$ . On the other hand, at a low In surface coverage ( $K_{In} P_{TMIn} \ll 1$ ) case, there would be a linear dependence of the growth rate on the  $MF_{TMIn}$ . As a result, in this growth condition of InSb, strong dependence of the growth rate on  $MF_{TMIn}$

indicates deficient In growth conditions on the surface, resulting in the enhancement of the growth rate with increasing  $MF_{TMIn}$ .

From the Fig. 4.5 (a-c), we observed that the growth rate was influenced on the growth temperature and showed the linear dependence of  $MF_{TMIn}$  and independent of  $MF_{TMSb}$ . This indicates that TMIn precursors are not fully decomposed at the investigated  $T_G$  ranges from 450 to 510 °C even though it was reported that TMIn in  $H_2$  ambient are fully decomposed [20]. This was caused by hydrogen radicals. Buchan *et. al.*, investigated the decomposition of TMIn  $[(CH_3)_3In]$  in  $H_2$  ambient with mass spectroscopic techniques and suggested the possible process. A chain reaction of TMIn is indicated below.



A possible In formation process is below



From the eq. 4-5, H radical was formed due to the chemical reaction between  $CH_3$  and  $H_2$ . These H radical has important role in producing In atoms from

monomethylindium as shown in eq. 4-7. Larsen *et. al.* reported the decomposition of TMSb [16] and possible chain reaction of TMSb is indicated below



From the decomposition of TMSb, H radicals were generated as indicated eq 4-9 and have import role in decomposition of TMSb as represented in eq. 4-10. H radicals produced in both precursors make an important role to enhance the decomposition of TMSb and to retard the TMIn in the mixture of TMIn and TMSb in H<sub>2</sub> ambient [16]. H radical produced in TMIn decomposition [eq. 4-5] will affect to decompose the TMSb precursor and producing increase of TMSb decomposition rate. As a result, the decomposition of TMIn was retarded due to the depletion of H radicals in the co-existence of TMIn and TMSb systems.

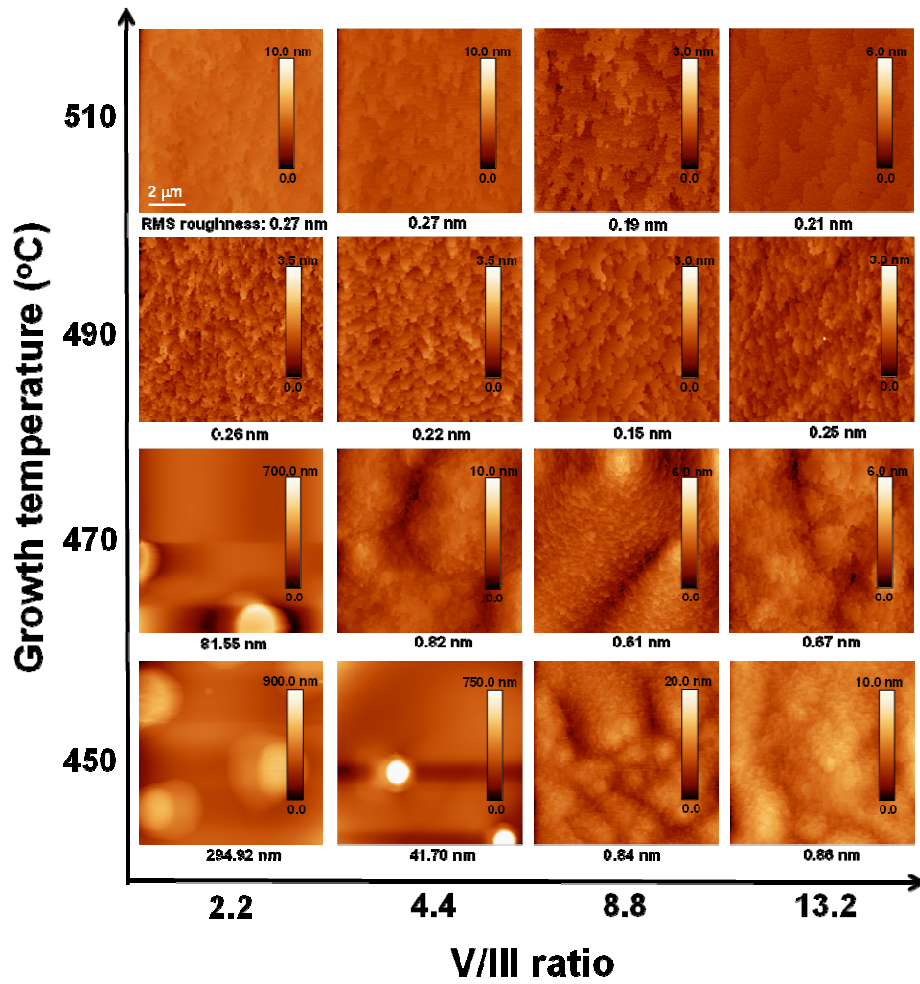


Fig. 4.3. AFM images of InSb epilayers grown at different V/III ratio and growth temperature.

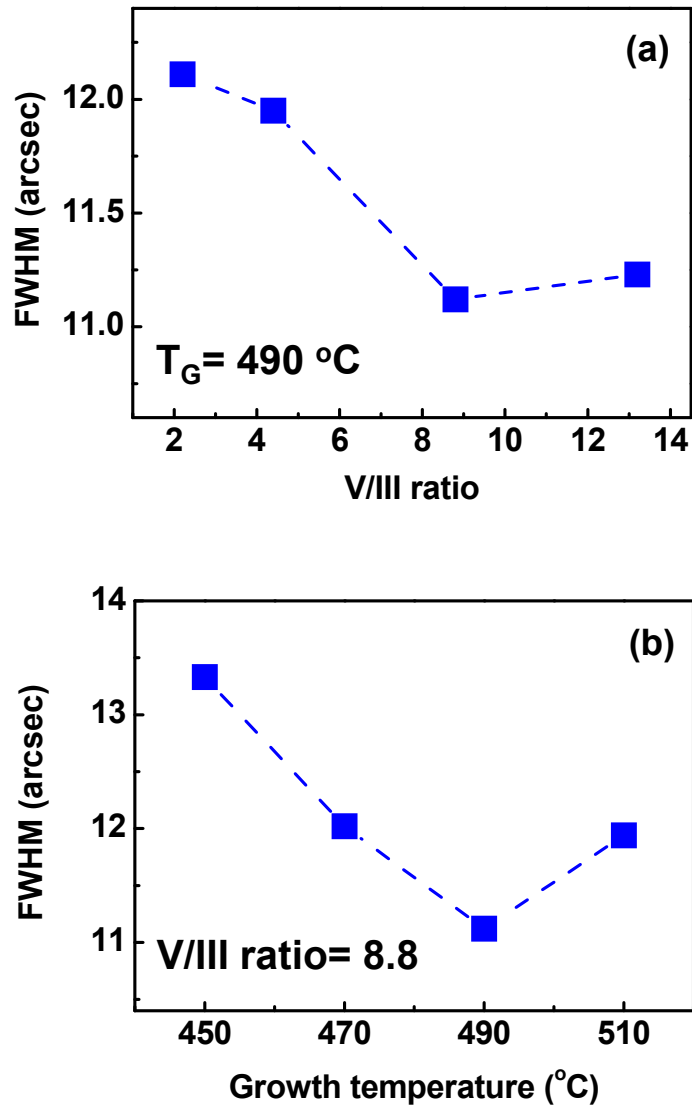


Fig. 4.4. FWHM of InSb grown at different (a) V/III ratio and (b) growth temperature

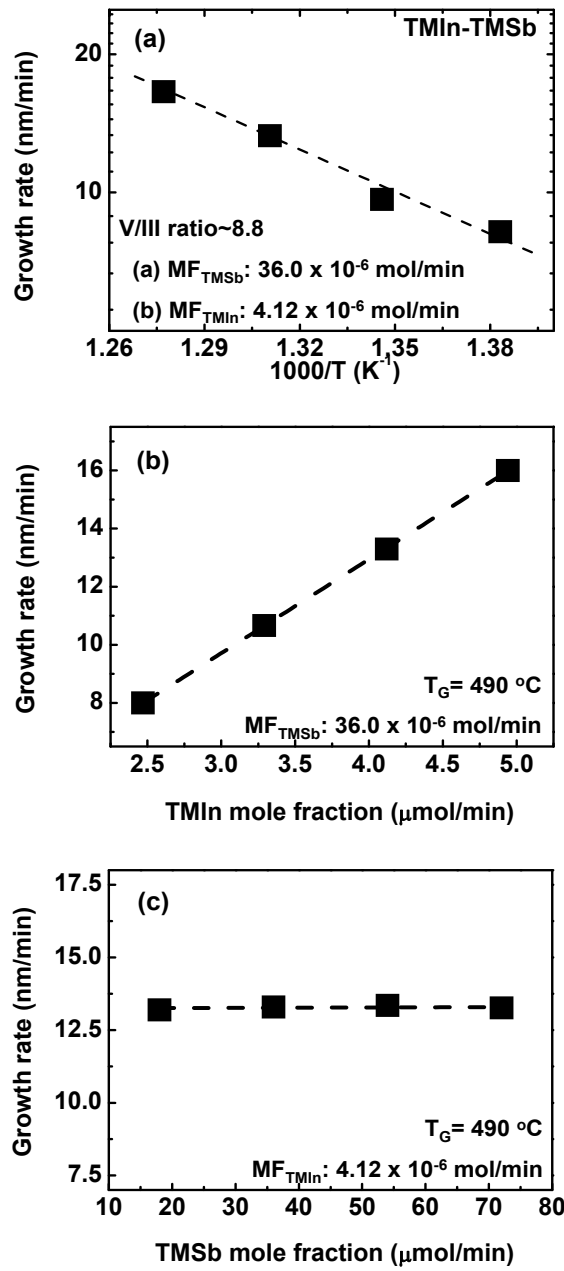


Fig. 4.5. (a) Arrhenius plot of the growth rate of InSb for TMIn/TMSb. Growth rate of InSb at 490 °C for varying (a) TMIn mole fraction and (b) TMSb mole fraction

## 4.5 Optical analysis of unintentionally doped InSb

### 4.5.1. Near band edge (NBE) emission shift

Figure 4.6 (a) shows the 10 K PL spectra obtained from the unintentionally doped InSb epitaxial layers grown on InSb substrates at various V/III ratios. The V/III ratio was varied from 2.2 to 13.2 at a fixed growth temperature ( $T_G$ ) of 490 °C. The PL spectra were intentionally offset along the y-axis with respect to each other for better clarity. The PL spectrum of our InSb samples consisted of four PL peaks positioned near 235 meV (#1), 228 meV (#2), 212 meV (#3) and 175 meV(#4). PL measurements were conducted at 10 K and 532 nm  $Ar^+$  laser with a power density of 400 mW were used for all measurement.

The highest PL emissions (#1) were assigned as near band edge (NBE) emission because the PL emission energies were agreed reasonably well with the previous reported band gap values of InSb [5, 8, 21-24]. From the Fig. 4.6 (a), the shift of the #1 emission was observed depending on the V/III ratio ranging from 2.2 to 13.2. In Fig. 4.6 (b), InSb sample grown at V/III ratio of 8.8 was found to have the highest PL peak position located at 236.2 meV along with the narrowest a full width at half maximum (FWHM) of 3.2 meV. The FWHM was obtained by deconvolution of peak #1, #2 and #3. However, there were red shift of the PL emission and a tendency toward increasing FWHM for samples grown at both lower and higher V/III ratio. The largest red shift of PL emission was appeared at 234.2 meV along with FWHM of

4.2 meV for the InSb sample grown at V/III ratio of 2.2. These behaviors with various V/III ratios can be explained by three main factors of variation of carrier concentrations, residual strains induced in the InSb epilayers and impurity energy level formation (Urbach tail) [25-27].

In order to investigate the origin of NBE emission shift with respect to the V/III ratio, electrical properties of the InSb samples were firstly investigated by Hall measurements at 77 K. A magnetic field of 0.37 T was applied during the measurements. The carrier concentration and Hall mobility of the InSb samples as a function of the V/III ratio were plotted in Fig. 4.7. In the investigated V/III ratio ranges, all InSb sample showed n-type conductivity regardless of V/III ratio, implying that charged donor type of defect was incorporated spontaneously into the InSb epitaxial layers in all V/III ratio range. This result was similar to other reported conductivity type of unintentionally doped InSb samples grown by MOCVD [28, 29].

When the carrier concentrations in InSb epitaxial layers were changed with a dependence of V/III ratio as shown in Fig. 4.7, the NBE can be shifted due to the Burstein-Moss (BM) shift and/or band gap renormalization (BGR) effects [26]. The BM shift was the shift of the absorption edge to higher energies occurring at high doping concentrations. This effect was induced by the band filling. When the carrier concentration was increased, the carrier can be occupied from the bottom of the conduction band and further occupy the higher energy level in conduction band due to the finite density of state. Due to the band filling, absorption transitions cannot occur from the bottom of the conduction band to the top of the valence band. As a result, higher emission

energy was induced. With increasing carrier concentration in InSb, another effect of BGR has to be considered. At high carrier concentration, band gap energy decreases due to the many reasons. The most important reasons for BGR are many-body effects of free carriers which lower the electron energies as compared to a non-interaction carrier system. At higher carrier concentration system, carrier interactions between free carriers became increased due to the small carrier to carrier distance. Electrons can interact with each other either by their long-range coulomb potential or via their electron spin. Electrons in higher carrier systems can be redistributed spatially in order to reduce the long-range Coulomb interaction energy. The energy of the electron added to the semiconductor is reduced by the redistribution of neighboring electrons. Carriers can also interact with their spins. Due to the Fermion nature of electrons, each volume element in phase space can be occupied by at most two electrons with opposite spin due to the Pauli principle. Electrons with the same spin have a repulsive interaction while electrons with opposite spin have an attractive interaction. If electrons were distributed uniformly throughout the crystal, the attractive and repulsive energies would exactly cancel each other. However, due to the interaction, electrons with the same spin tend to position away from each other and electrons with opposite spin tend to locate closer. As a result, the interaction energy reduces the total energy of the electron system. In order to investigate the origin of carrier concentration increase with V/III ratio variation, some InSb epitaxial layer samples grown at V/III ratio of 2.2, 8.8 and 13.2 was measured by SEM. In case of InSb samples grown at V/III ratio of 8.8 and 13.2 showed smooth surface morphology. However InSb sample grown at V/III ratio of 2.2 as shown in Fig. 4.8 (a), droplets were formed on the InSb

surface. Inset was the enlarged SEM image of droplets. To confirm the chemical composition of the droplets, HCl etching and EDX analysis was conducted. If the droplet was composed of In, it was completely removed from the surface after dipping in HCl. Both analyses showed that it was In as shown in Fig. 4.8 (b). It indicates that InSb epitaxial layers were grown under In-rich growth condition at V/III ratio of 2.2. Based on the PL intensity (Fig. 4.8 (c)) and FWHM (Fig. 4.6 (b)) indicates that InSb epitaxial layers were grown under near stoichiometric growth condition at V/III ratio of 8.8, whereas it was grown under Sb-rich growth condition at V/III ratio of 13.2.

From the AFM results as shown in Fig. 4.3, best surface morphologies were obtained at V/III ratio of 8.8 and it was slightly increased with increasing and decreasing V/III ratio. Especially, when enlarged AFM image of V/III ratio of 2.2 at 490 °C, small spots were observed on the InSb surface which was confirmed as In droplets by XRD measurements. It indicates that In-rich InSb growth condition was induced below V/III ratio of 8.8 and it became Sb-rich InSb growth condition at V/III ratio of 13.2. These were coincident with results as explained above.

At V/III ratio of 8.8, the lowest carrier concentration of  $3.7 \times 10^{16} \text{ cm}^{-3}$  was measured with the highest Hall mobility of  $2.3 \times 10^4 \text{ cm}^2/\text{Vs}$  while the increase of carrier concentration with the reduction of Hall mobility was observed at both lower and higher V/III ratio. The highest carrier concentration of  $2.6 \times 10^{17} \text{ cm}^{-3}$  was measured at V/III ratio of 2.2 along with the lowest Hall mobility of  $9.5 \times 10^3 \text{ cm}^2/\text{Vs}$ . This result indicated that an amount of charged defects were increased in InSb epitaxial layers and

affecting to increase background electron densities when they were grown under In-rich and/or Sb-rich growth conditions. As a consequence of the incorporated charged defects, the reduction of Hall mobility was observed by charged impurity scattering, which was dominant scattering mechanism at a low temperature of 77 K [1].

From the Hall measurement at 77 K, charged impurity was incorporated in InSb with dependence of V/III ratio, affecting increasing carrier concentrations. The origin of charged impurity in In-rich and Sb-rich InSb growth conditions were investigated. In general, native defects in InSb were Sb vacancies ( $V_{Sb}$ ), In vacancies ( $V_{In}$ ), Sb interstitials ( $Sb_i$ ), In interstitials ( $In_i$ ), Sb antisites ( $Sb_{In}$ ) and In antisites ( $In_{Sb}$ ). Among these defects, based on the theoretical calculation of native defect formation energy, Høglund *et al.*, reported that  $In_i$ ,  $Sb_{In}$  and  $Sb_i$  were positively charged and worked as donors by providing electrons in both n- and/or p-type InSb [30]. It was reported that  $In_i$  has the lowest defect formation energy in In-rich growth conditions, which corresponds to the V/III of 2.2 in our experiment. In other words, some interstitial sites in the InSb epitaxial layers were occupied by extra In atoms under the In-rich growth condition, leading to the generation of  $In_i$  defects and contributing on n-type conduction. When more donor type of charged defects,  $In_i$ , were incorporated in InSb epitaxial layers grown under In-rich growth environments, the PL peak position of the #1 was red shift due to the band edge fluctuation. As the  $In_i$  was randomly distributed in InSb epitaxial layers, potential fluctuations of the conduction band edge were generated depending on the strong and less interaction due to the local crowding of the  $In_i$ . It leads to the energy state formation below the band edge because it has

positive charge due to the ionization. On the other hand, the effect of the potential fluctuations at V/III ratio of 8.8 can be suppressed due to the small present of residual donor type defect. This red shift of NBE emission due to band edge fluctuation was confirmed by the Hall mobility. At V/III ratio of 2.2 where lots of donor type of defects was incorporated, Hall mobility was decreased due to the impurity scattering but Hall mobility was increase with increasing V/III ratio. In conclusion, red shift of NBE emission was attributed by the band edge fluctuation due to the incorporated donor type defects which modify the band edges to produce the deep well regions as shown in Fig. 4.9 (a). The fluctuated band edge forms the energy state below conduction band edges to generate red shift of NBE emission as represented in Fig 4.9 (b).

When the  $\text{In}_i$  was incorporated in the InSb sample, it may produce locally residual strains in the surrounded InSb crystals, which cause the #1 shift depending on the types of strains [25]. In order to confirm the effect of residual strains on the peak shift, Raman measurement was implemented. Figure 4.10 (a) shows Raman spectroscopy result for all InSb samples. Two phonon modes of InSb were assigned to longitudinal optical (LO) and transverse optical (TO) phonon modes positioned at  $191 \text{ cm}^{-1}$  and  $180 \text{ cm}^{-1}$ , respectively. These values were in good agreement with the reported values [31, 32]. No Raman shift of LO phonon regardless of V/III ratio was observed, indicating that residual strains in InSb epilayers have not been induced [33, 34]. This result represented that incorporated  $\text{In}_i$  was not induced enough residual strains in InSb samples to shift of the #1.

Raman spectrum contained additional valuable information of InSb epitaxial layers to support the crystal quality. Compared to the strong intensity of LO phonon modes, all Raman spectra of InSb epitaxial layers showed the weak intensity of TO phonon modes, which should be forbidden in Raman spectra due to the Raman selection rule for zincblende crystal structure of InSb (001) plane [35]. The appearance of forbidden TO phonon mode in Raman backscattering from an InSb (001) surface indicates the formation of disordered structures. From the calculation of the intensity ratio of the TO mode against that of the LO mode ( $I_{TO}/I_{LO}$ ) as a function of V/III ratio as shown in Fig. 4.9 (c), the formation of TO mode was suppressed at a V/III ratio of 8.8 and it was increased when InSb epitaxial layers were grown under In-rich and Sb-rich growth condition, showing that high quality of InSb epitaxial layers with low degree of disorder was obtained at V/III ratio of 8.8. The degree of disorder structure was reflected in full width at half maximum (FWHM) of LO phonon mode as shown in Fig 4.10 (c). A narrow FWHM of  $7.28 \text{ cm}^{-1}$  was observed at V/III ratio of 8.8 and the FWHM was broaden to  $8.66 \text{ cm}^{-1}$  at V/III ratio of 2.2. This trend was well coincidence with FWHM of PL.

As previously reported, the peaks near 228 meV (#2) and near 212 meV (#3) have been commonly assigned to impurity emission and InSb optical phonon emission, respectively [5, 6].

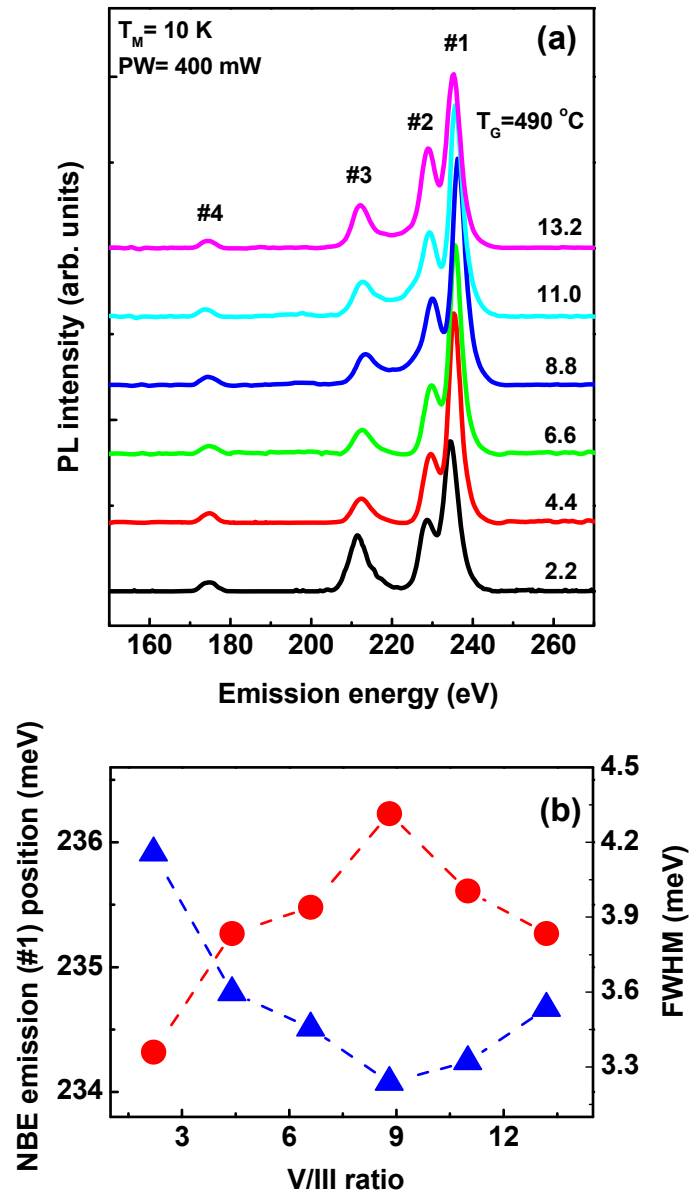


Fig. 4.6. (a) PL spectrum of InSb samples grown at different V/III ratio range from 2.2 to 13.2. (b) Peak position and FWHM of NBE emission with a dependence of V/III ratio

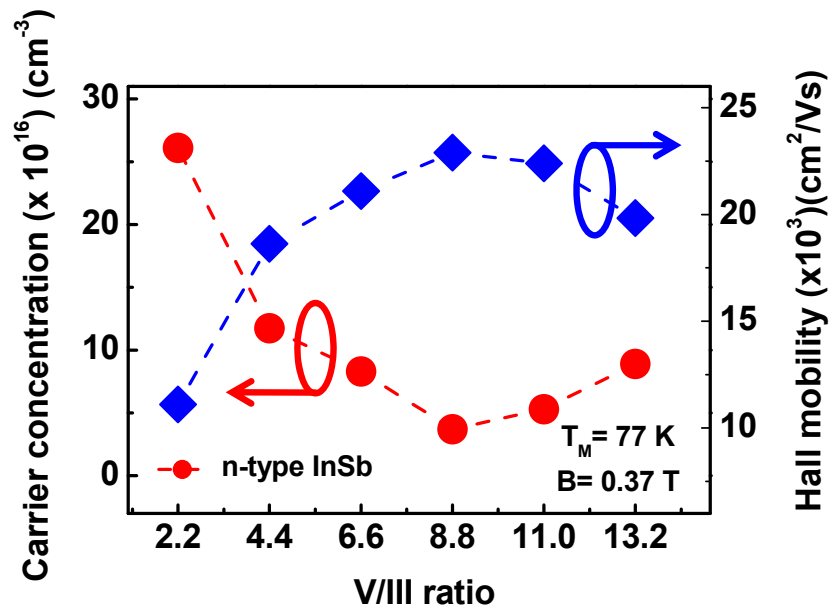


Fig. 4.7. Carrier concentration and Hall mobility for the InSb samples grown at various V/III ratios. Hall measurements were performed at 77 K under applied magnetic field of 0.37 T.

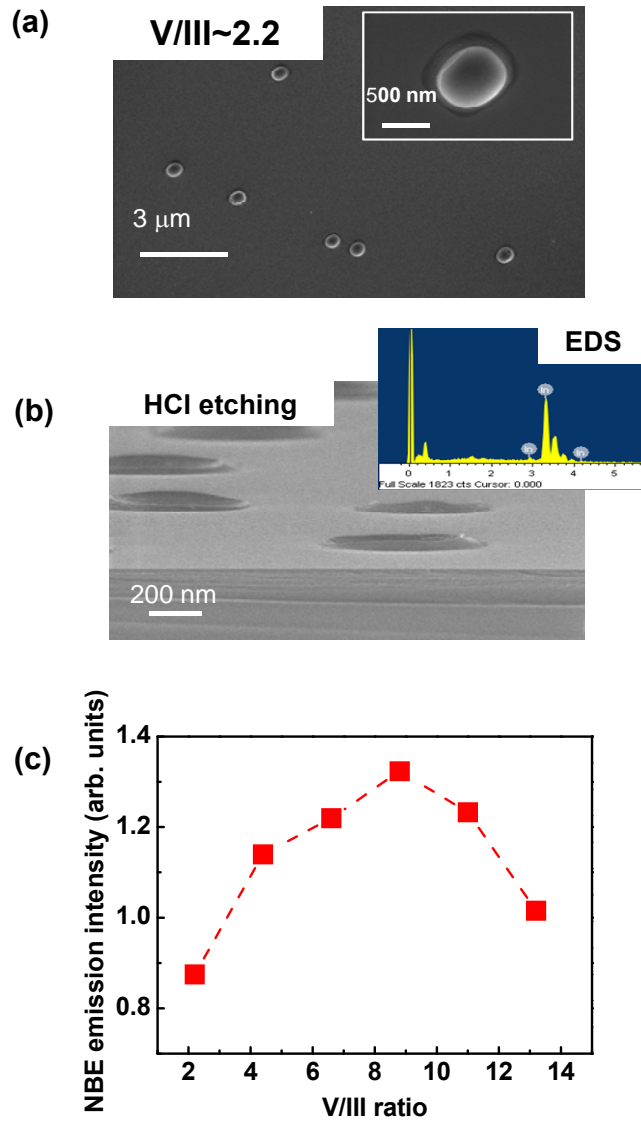


Fig. 4.8. (a) SEM image of InSb sample grown at V/III ratio of 2.2. Inset shows the enlarged image of droplet. (b) Chemical composition of droplet was confirmed by HCl etching and EDX analysis, indicating In droplet. (c) PL intensity of NBE emission with a dependence of V/III ratio

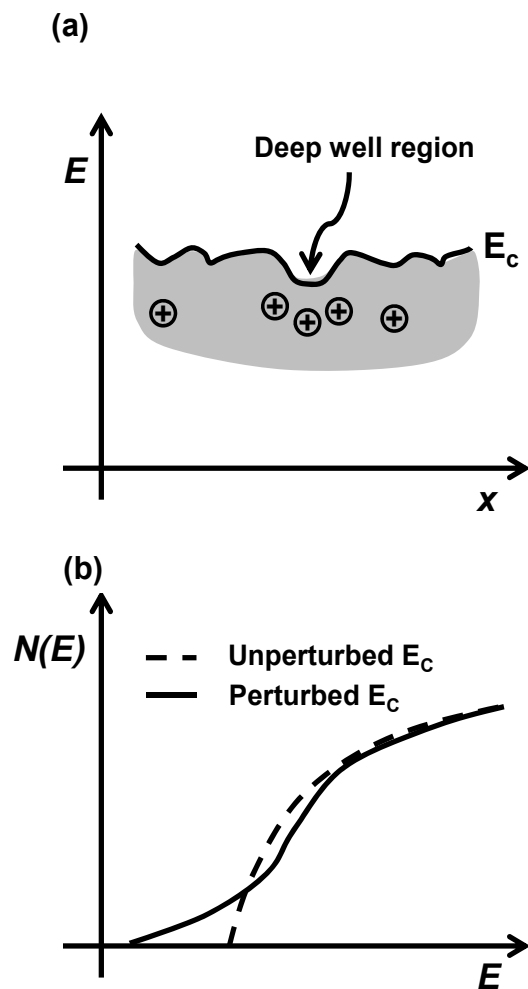


Fig. 4.9. (a) Band edge fluctuation due to incorporated donor type of defects  
 (b) Plots of energy and density of states. Two types of density of state due to perturbed and unperturbed conduction band ( $E_c$ )

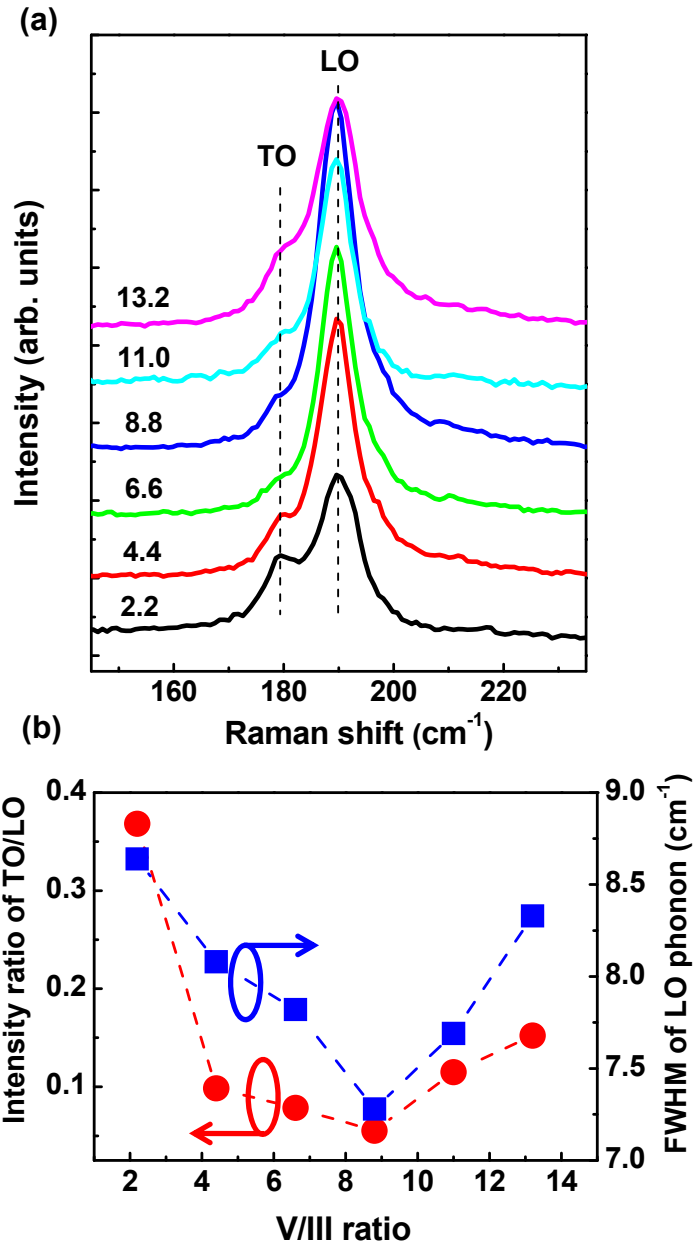


Fig. 4.10. (a) Raman spectrum of all InSb samples (b) Intensity ratio of TO/LO and FWHM of LO phonon with a dependence of V/III ratio.

## 4.5.2. Carbon impurity related PL emission

New PL peak denote #4 was observed at 175 meV in all InSb epitaxial layers as can be seen in Fig. 4.6 (a). Until now, the origin of this PL peak was unclear in both bulk InSb and InSb epitaxial layers.

In order to investigate the origin of the #4, InSb samples were grown at different  $T_G$  ranging from 450 to 510 °C at a fixed V/III ratio of 8.8. PL spectra of the samples were shown in Fig. 4.11 (a). The PL spectra suggested that optical quality of InSb epitaxial layers were significantly influenced by the  $T_G$ . Only strong PL intensity of the Peak #1 was observed in InSb sample grown at 490 °C, while there were sharply drops in the PL intensity at both lower and higher  $T_G$ , indicating that InSb growth windows were very narrow to grow high quality InSb epitaxial layers. The Peak #4 was observed in all InSb samples but its intensity was varied with  $T_G$ . A strong PL intensity of the peak was measured for the sample grown at 450 °C and they were gradually decreased with increasing  $T_G$  to 510 °C. For an easy comparison, the inset in Fig. 4.11 (a) represented the PL spectrum of bulk InSb, showing an absence of the #4. A relative intensity of #4 was plotted in Fig. 4.11 (b). The temperature dependence of the peak intensities suggested that a possible candidate may be carbon, originated from incomplete decomposed metal organic sources of either TMIIn or TMSb.

To further investigate the origin of the #4, SIMS depth profile of carbon (C) were performed for two InSb samples. Figure 4.12 show the SIMS depth profiles of C obtained from InSb epitaxial layers/InSb substrate structures.

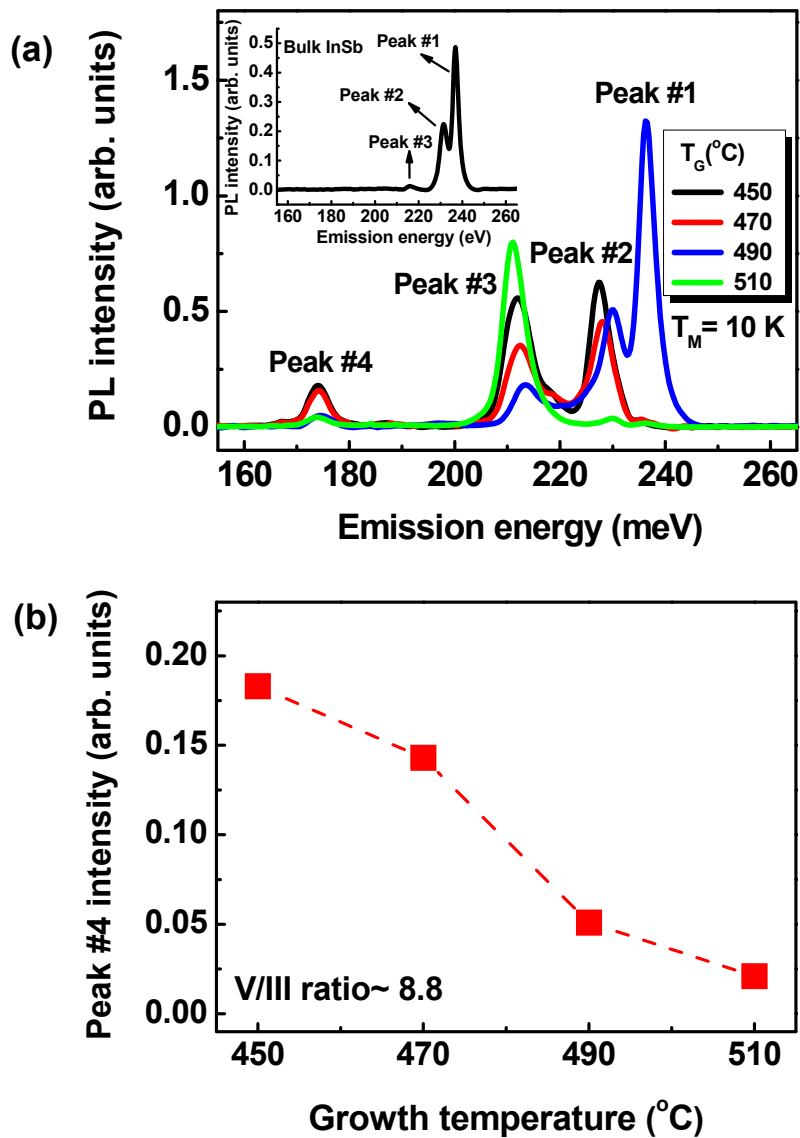


Fig. 4.11. (a) PL spectrum of InSb samples grown at different  $T_G$  ranged from 450 to 510 °C. PL spectrum was measured at 10 K with a power density of 400 mW. The inset shows the PL spectrum of bulk InSb. (b) The relative PL intensity of the #4 was represented as a function of  $T_G$ .

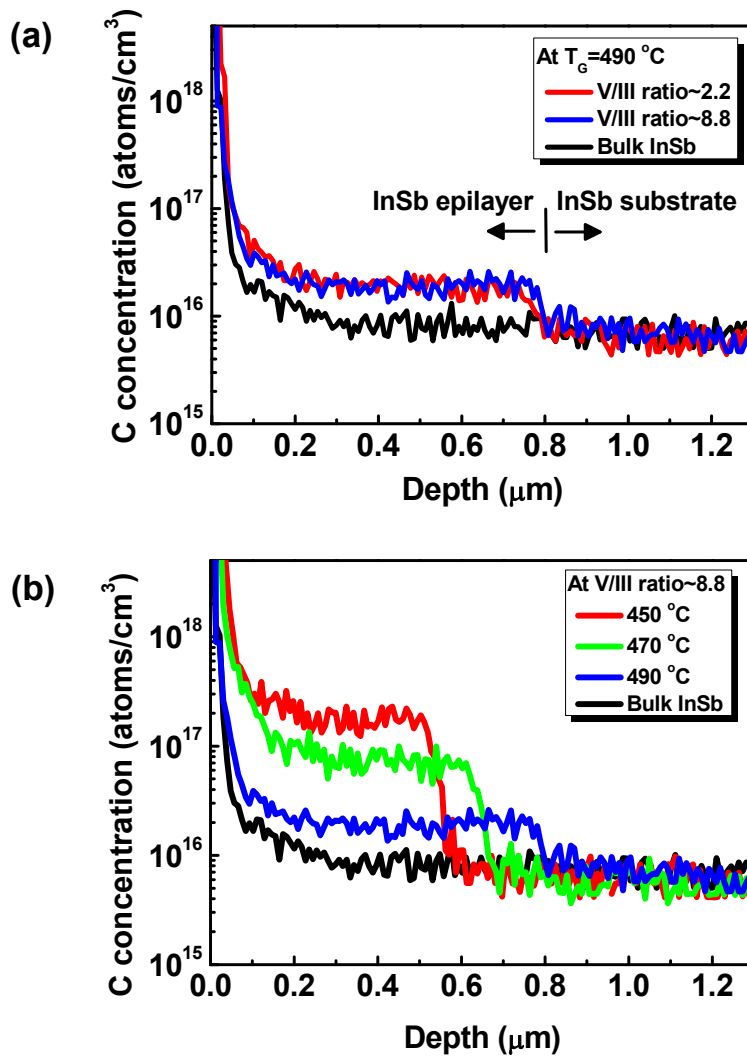


Fig. 4.12. SIMS depth profile of carbon in InSb epilayer/InSb substrate structures. Carbon concentration in InSb samples grown at (a) V/III ratio of 2.2 and 8.8 and (b)  $T_G$  of 450, 470 and 490 °C. SIMS depth profiles of bulk InSb was inserted as a reference

C concentrations were plotted for the samples grown at (a) different V/III ratio of 2.2 and 8.8 (b) different growth temperature of 450, 470 and 490 °C. Figure 4.12 (a) shows that the same C concentration of  $2 \times 10^{16} \text{ cm}^{-3}$  was detected in both two InSb samples but the C concentration in bulk InSb was near the equipment's measuring background level of  $10^{16} \text{ cm}^{-3}$  [36]. On the other hand, we found that the C concentrations in the InSb epitaxial layers were significantly influenced by the  $T_G$  as shown in Fig. 4.12 (b). The highest C concentration of  $2.5 \times 10^{17} \text{ cm}^{-3}$  in the InSb sample grown at 450 °C was detected and the C concentrations were gradually decreased with increasing  $T_G$ . At 490 °C, the C concentration of  $2 \times 10^{16} \text{ cm}^{-3}$  was measured.

In order to make an interpretation of C incorporation mechanism in our InSb samples grown using the mixture of TMIIn + TMSb, we suspected that C atoms can be derived from methyl radicals in TMSb molecules, instead of methyl radicals in TMIIn molecules due to the binding strength differences between of In-CH<sub>3</sub> and Sb-CH<sub>3</sub>. A Sb-CH<sub>3</sub> has much stronger binding strength than the binding strength of In-CH<sub>3</sub> [37]. This explanation was coincident with the TMSb decomposition rate in the investigated temperature region due to the relatively strong binding [37, 38].

## 4.6 P-type doping in InSb

Diethylzinc (DEZn) was used as p-type dopant for InSb and various growth conditions were investigated to obtain p-type doping concentration for the fabrication of InSb PD's.

From Fig. 4.13 (a), the hole concentration increase linearly with increasing DEZn mole fraction at a fixed  $T_G$  of 490 °C. This result is consistent with zinc doping in GaAs and InP [39-41]. When the DEZn mole fraction of 0.144  $\mu\text{mol}/\text{min}$  was applied to the growth chamber, hole concentration of  $4.76 \times 10^{18} \text{ cm}^{-3}$  was obtained with Hall mobility of  $425 \text{ cm}^2/\text{Vs}$ . With increasing DEZn mole fraction up to 1.225  $\text{mmol}/\text{min}$ , hole concentration of  $41.0 \times 10^{18} \text{ cm}^{-3}$  and Hall mobility of  $253 \text{ cm}^2/\text{Vs}$  were obtained, respectively.

The hole concentration was observed to increase as the  $T_G$  was increased as shown in Fig. 4.13 (b) for a fixed DEZn mole fraction. The strong temperature dependence of hole concentration was explained by two mechanism of Zn atom re-evaporation and growth rate. When the temperature become high, the vapor pressure of Zn was increased, introducing the increase of evaporation of Zn atoms from the growth surface [42, 43]. The vapor pressure of Zn is inversely proportional to the Zn incorporation, which is generally expressed as [42]

$$P_{\text{Zn}} = P_0 \exp(-E_0/kT_G) \quad [\text{eq. 4-12}]$$

where  $P_0$  is a pre-exponential factor,  $T_G$  is the growth temperature and  $E_0$  is

the activation energy. As indicated in eq. 4-12, the vapor pressure of Zn is exponentially increased with increasing growth temperature.

However, the growth rate of InSb in this investigated  $T_G$  ranges was found to be increased with increasing  $T_G$  as indicated in Fig. 4.5 (a). In this investigated  $T_G$  ranges, growth rate was controlled by the decomposition of TMIIn precursors, which is not completely decomposed due to the H radical depletion. At high growth rate, the deposited Zn atoms are absorbed into the InSb epilayers before it can be evaporated from the growth surface. On the other hand, Zn atoms diffused out from the surface before they can be incorporated at lower growth rate. Thus, as the growth rate was increased, the residence time of Zn required for incorporation decrease. This effect was also observed in Zn doping in GaAs [44]. Even though, in this  $T_G$  ranges, hole concentration has to be increased due to the increase of growth rate. However the hole concentration was decreased with increasing  $T_G$ , implying that the main mechanism for Zn incorporation was dominated by the Zn re-evaporation with increasing  $T_G$ .

Hall mobility was also influenced by the hole concentration as shown in Fig. 4.13. Lower Hall mobility was observed at higher hole concentration due to the scattering effect. The optimized p-type doping concentration for the device operation was determined with DEZn mole fraction of 0.144  $\mu\text{mol/min}$  grown at 490 °C in order to obtain mid  $10^{18} \text{ cm}^{-3}$  hole concentration.

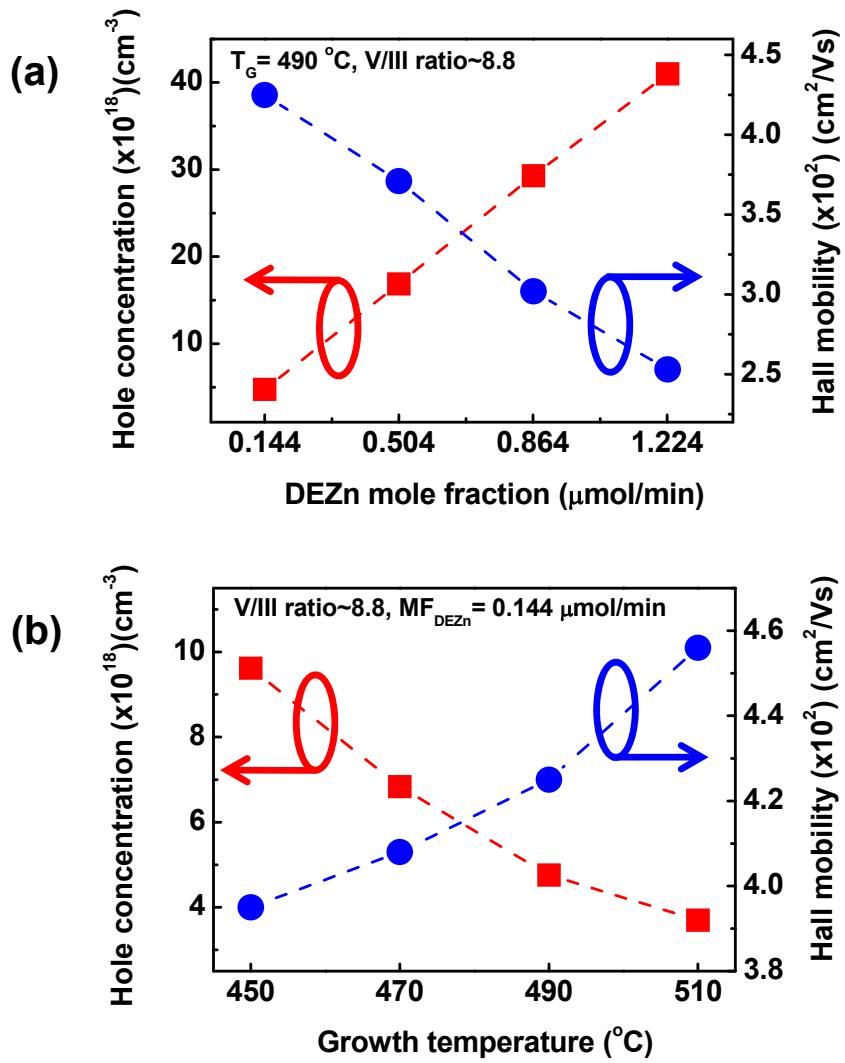


Fig. 4.13. (a) Hole concentration and Hall mobility of Zn doped InSb as a function of (a) DEZn mole fraction (b) growth temperature.

## 4.7 Summary

In this chapter, epitaxial growth using LP-MOCVD under various growth parameters were conducted to obtain high quality InSb epilayers. Surface morphology was significantly influenced by the V/III ratio and growth temperatures. At low V/III ratio, In droplet was formed on the surface due to the insufficient In supply to grow stoichiometric InSb epilayers. On the other hand, at high V/III ratio, although rough surface morphology was observed, Sb hillocks were not observed in this V/III ranges. At low  $T_G$ , In droplet was formed, however it was removed with increasing  $T_G$ , implying that TMSb was not completely decomposed in this investigated  $T_G$  ranges.

From the growth behavior of InSb, the growth rate of InSb using TMIn and TMSb were controlled by the surface reaction limited due to the incomplete precursor decomposition in the  $T_G$  ranges. At a fixed  $T_G$ , growth rate of InSb was dependent on the TMIn mole fraction but independent on the TMSb mole fraction due to the vapor pressure differences between two precursors.

PL measurements were conducted for InSb samples grown at various growth conditions. Red shift of near band edge emission was observed with increasing and decreasing from V/III ratio of 8.8. At the same growth condition, donor type of carrier concentration was increased, implying that donor type of defects was generated during epitaxial growth. These defects were indium interstitial defect. However, the incorporated indium interstitial defect does not induce any residual strains in InSb. As a consequence, the red

shift of near band edge emission was caused by the band edge fluctuation, resulting in the reduction of NBE emission energy. I also observed the new PL peak emission which has not been reported yet. Its origin was caused by the carbon impurity induced by the Sb-CH<sub>3</sub> bonding due to the higher bonding strength.

In order to fabricate p-InSb layers, zinc doping was investigated into InSb with a dependence of DEZn mole fraction and growth temperatures. With increasing DEZn mole fraction, hole concentration showed the linear dependence. With increasing growth temperatures, hole concentration was decreased due to the increase Zn re-evaporation rate caused by the increase of Zn vapor pressure at higher temperature.

## 4.8 Bibliography

- [1] B. G. Streetman and S. Banerjee, *Solid state electronic devices* vol. 4: Prentice Hall New Jersey, 2000.
- [2] T. Moss and T. Hawkins, "Radiation de recombinaison dans l'antimoniure d'indium," *J. Phys. Radium*, vol. 17, pp. 712-712, 1956.
- [3] T. Moss and T. Hawkins, "Recombination Radiation from InSb," *Physical Review*, vol. 101, p. 1609, 1956.
- [4] J. Stotz and M. Thewalt, "Acceptor identification using magnetophotoluminescence of bound exciton states in InSb," *Physical Review B*, vol. 67, p. 155210, 2003.
- [5] J. Pehek and H. Levinstein, "Recombination radiation from InSb," *Physical Review*, vol. 140, p. A576, 1965.
- [6] A. Mooradian and H. Fan, "Recombination emission in InSb," *Physical Review*, vol. 148, p. 873, 1966.
- [7] N. Rowell, "Infrared photoluminescence of intrinsic InSb," *Infrared physics*, vol. 28, pp. 37-42, 1988.
- [8] Z. Fang, K. Ma, D. Jaw, R. Cohen, and G. Stringfellow, "Photoluminescence of InSb, InAs, and InAsSb grown by organometallic vapor phase epitaxy," *Journal of Applied Physics*, vol. 67, pp. 7034-7039, 1990.
- [9] C. Chen, Z. Fang, G. Stringfellow, and R. Gedridge Jr, "The use of triisopropylantimony for the growth of InSb and GaSb," *Journal of Applied physics*, vol. 69, pp. 7605-7611, 1991.

- [10] C. McConville, C. Whitehouse, G. Williams, A. Cullis, T. Ashley, M. Skolnick, *et al.*, "Interfacial studies and electrical characterisation of heteroepitaxial InSb on GaAs (100) grown by MBE," *Journal of Crystal Growth*, vol. 95, pp. 228-234, 1989.
- [11] V. Ivanov-Omskii, I. Petroff, V. Smirnov, S. U. Yuldashev, I. Ferguson, P. Tang, *et al.*, "Magnetophotoluminescence of MBE-grown InSb and InAs," *Semiconductor science and technology*, vol. 8, p. 276, 1993.
- [12] H. Mori and S. Takagishi, "Morphology of GaAs epitaxial layers grown by MOCVD," *Journal of crystal growth*, vol. 69, pp. 23-28, 1984.
- [13] R. M. Biefeld, "The preparation of device quality gallium phosphide by metal organic chemical vapor deposition," *Journal of Crystal Growth*, vol. 56, pp. 382-388, 1982.
- [14] B. J. Baliga and S. K. Ghandhi, "Hillocks on epitaxial GaAs grown from trimethylgallium and arsine," *Journal of Crystal Growth*, vol. 26, pp. 314-316, 1974.
- [15] R. M. Biefeld, "The preparation of InSb and InAs  $1-x$  Sb  $x$  by metalorganic chemical vapor deposition," *Journal of Crystal growth*, vol. 75, pp. 255-263, 1986.
- [16] C. Larsen, S. Li, and G. Stringfellow, "Decomposition mechanisms of trimethylantimony and reactions with trimethylindium," *Chemistry of Materials*, vol. 3, pp. 39-44, 1991.
- [17] R. M. Biefeld, "The metal-organic chemical vapor deposition and properties of III-V antimony-based semiconductor materials," *Materials Science and Engineering: R: Reports*, vol. 36, pp. 105-142, 2002.

- [18] S. Jha, M. K. Wiedmann, and T. Kuech, "A comparative precursor study of the growth behavior of InSb using metal-organic vapor phase epitaxy," *Journal of Crystal Growth*, vol. 315, pp. 87-90, 2011.
- [19] M. K. Rathi, B. E. Hawkins, and T. F. Kuech, "Growth behavior of GaSb by metal-organic vapor-phase epitaxy," *Journal of crystal growth*, vol. 296, pp. 117-128, 2006.
- [20] N. Buchan, C. Larsen, and G. Stringfellow, "Mass spectrometric studies of trimethylindium pyrolysis," *Journal of Crystal Growth*, vol. 92, pp. 591-604, 1988.
- [21] F. Fuchs, K. Kheng, K. Schwarz, and P. Koidl, "Fourier transform photoluminescence excitation spectroscopy of medium-bandgap Hg<sub>1-x</sub>CdxTe and InSb," *Semiconductor Science and Technology*, vol. 8, p. S75, 1993.
- [22] D. Auvergne, J. Camassel, H. Mathieu, and M. Cardona, "Temperature dependence of the band structure of germanium-and zinc-blende-type semiconductors," *Physical Review B*, vol. 9, p. 5168, 1974.
- [23] S. Zwerdling, W. Kleiner, and J. Theriault, "Oscillatory magnetoabsorption in InSb under high resolution," *Journal of Applied Physics*, vol. 32, pp. 2118-2123, 1961.
- [24] C. Littler and D. Seiler, "Temperature dependence of the energy gap of InSb using nonlinear optical techniques," *Applied Physics Letters*, vol. 46, pp. 986-988, 1985.
- [25] C. F. Klingshirn, *Semiconductor optics*: Springer Science & Business Media, 2012.
- [26] E. F. Schubert, *Physical Foundations of Solid-State Devices*: E. Fred

Schubert, 2015.

- [27] J. I. Pankove, *Optical processes in semiconductors*: Courier Corporation, 2012.
- [28] R. Biefeld, S. Kurtz, and I. Fritz, "Doping and p-n junction formation in InAs<sub>1-x</sub>Sb<sub>x</sub>/InSb SLS's by MOCVD," *Journal of electronic materials*, vol. 18, pp. 775-780, 1989.
- [29] P. Chiang and S. Bedair, "p-n junction formation in InSb and InAs<sub>1-x</sub>Sb<sub>x</sub> by metalorganic chemical vapor deposition," *Applied Physics Letters*, vol. 46, pp. 383-385, 1985.
- [30] A. Höglund, C. Castleton, M. Göthelid, B. Johansson, and S. Mirbt, "Point defects on the (110) surfaces of InP, InAs, and InSb: A comparison with bulk," *Physical Review B*, vol. 74, p. 075332, 2006.
- [31] A. Pinczuk and E. Burstein, "Raman Scattering from InSb Surfaces at Photon Energies Near the E<sub>1</sub> Energy Gap," *Physical Review Letters*, vol. 21, p. 1073, 1968.
- [32] R. Leite and J. Scott, "Resonant surface Raman scattering in direct-gap semiconductors," *Physical Review Letters*, vol. 22, p. 130, 1969.
- [33] F. Cerdeira, C. Buchenauer, M. Cardona, and F. Pollak, "Stress-induced shifts of first-order Raman frequencies of diamond and zincblende-type semiconductors," *Phys. Rev. B*, vol. 5, 1972.
- [34] G. Armelles, T. Utzmeier, P. A. Postigo, F. Briones, J. C. Ferrer, P. Peiro, *et al.*, "Raman scattering of InSb quantum dots grown on InP substrates," *Journal of applied physics*, vol. 81, pp. 6339-6342, 1997.
- [35] J. L. Birman, "Theory of infrared and Raman processes in crystals: selection rules in diamond and zincblende," *Physical Review*, vol. 131,

- p. 1489, 1963.
- [36] A. Galuska and F. Greulich, "Detection limit for carbon in InSb during SIMS depth profiling," *Surface and Interface Analysis*, vol. 17, pp. 15-21, 1991.
  - [37] G. B. Stringfellow, *Organometallic vapor-phase epitaxy: theory and practice*: Academic Press, 1999.
  - [38] M. Cherng, H. Jen, C. Larsen, G. Stringfellow, H. Lundt, and P. Taylor, "MOVPE growth of GaInAsSb," *Journal of Crystal Growth*, vol. 77, pp. 408-417, 1986.
  - [39] R. Glew, "Zinc doping of MOCVD GaAs," *Journal of Crystal Growth*, vol. 68, pp. 44-47, 1984.
  - [40] M. K. Hudait, P. Modak, S. Hardikar, and S. Krupanidhi, "Zn incorporation and band gap shrinkage in p-type GaAs," *Journal of applied physics*, vol. 82, pp. 4931-4937, 1997.
  - [41] S. Chichibu, M. Kushibe, K. Eguchi, M. Funemizu, and Y. Ohba, "High concentration Zn doping in InP grown by low-pressure metalorganic chemical vapor deposition," *Journal of applied physics*, vol. 68, pp. 859-861, 1990.
  - [42] K. Okamoto, H. Mawatari, K. Yamaguchi, and A. Noguchi, "Zinc-doped GaAs epilayers grown by atmospheric-pressure MOCVD using diethylzinc," *Journal of crystal growth*, vol. 98, pp. 630-636, 1989.
  - [43] G. Stringfellow, "The role of impurities in III/V semiconductors grown by organometallic vapor phase epitaxy," *Journal of Crystal Growth*, vol. 75, pp. 91-100, 1986.
  - [44] S. Sun, E. Armour, K. Zheng, and C. Schaus, "Zinc and tellurium

doping in GaAs and Al<sub>x</sub>Ga<sub>1-x</sub>As grown by MOCVD," *Journal of crystal growth*, vol. 113, pp. 103-112, 1991.

# Chapter 5. ZnS surface passivation of InSb photodiodes and its device performances

## 5.1. Introduction

There are two major methods to fabricate InSb PDs as described in section 1.3. When the IR PDs were fabricated by p-type ion implantation or sometimes diffusion method, surface effects were not significantly important for device operating. N-type contact can be formed near the p-contact, enabling the reducing the surface effects. However, surface effect became dominant leakage current path when mesa etching process was adopted. InSb pn structures were fabricated using epitaxial growth techniques, mesa etching process must be adapted to fabricate the IR PDs devices as shown in Fig. 5.1 (a). In mesa structures, the problem is that lots of surface area was exposed to air, resulting in the re-oxidation of surface and exposed the lots of surface dangling bonds. The re-oxidized surfaces produce the thermodynamically favorable phases of  $\text{In}_2\text{O}_3$  and elemental Sb as indicated in sec. 3.1. They were low resistance materials to make electrical path through the surface. Another problem was a dangling bond formed on the surfaces. In case of bulk zincblende structures, all bonding were connected each other. However, the periodic zincblende crystal structure terminates abruptly resulting in formation of unsatisfied (dangling) chemical bonds responsible for generation of surface states within the band gap. These states cause pinning of the surface Fermi level near the mid gap and, as a consequence, enhance the surface leakage currents. The schematic diagrams of dangling bonds were

introduced in enlarged square in Fig. 5.1 (a). When the thermal energy, which is not enough to excite electron from balance band to conduction band, was applied to the materials, carriers can be jump to conduction band through trap sites. Thus, in order to improve the overall device performance, methods for elimination of surface current is to deposit appropriate passivation layers on the surface. Through surface passivation techniques, three major dark current components can be eliminated [1]. (a) A generation current associated with the Shockley-Read-Hall (SRH) process in the depletion region of the detector (b) thermally generated diffusion current associated with Auger or radiative process in both the n- and p- extrinsic regions of the detector (c) A surface current associated with the surface states in the junction.

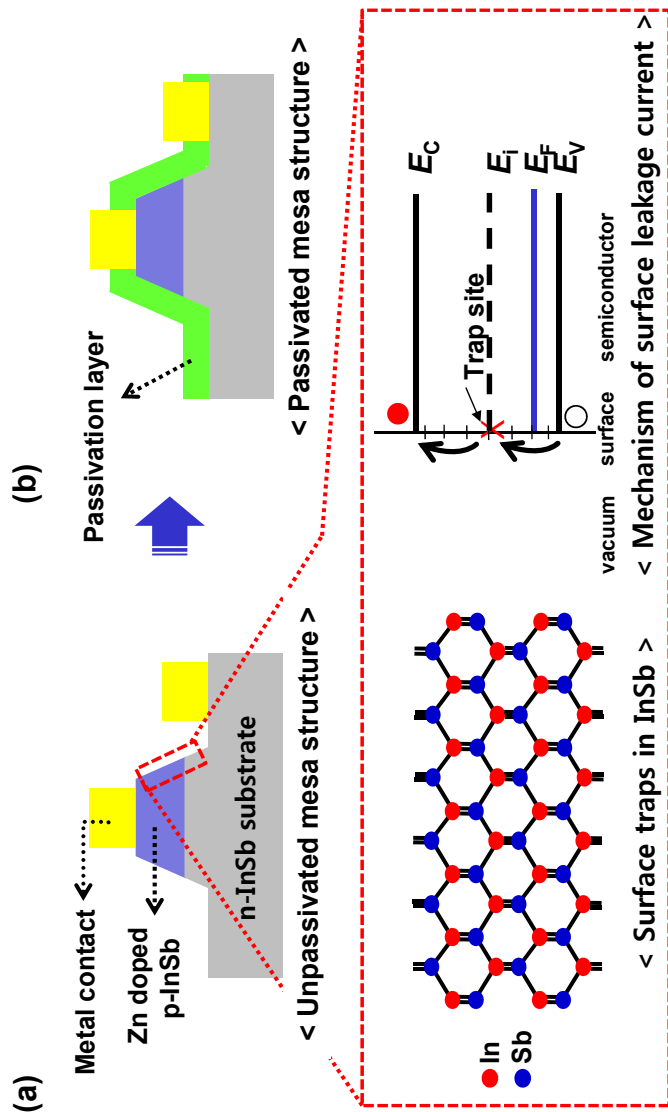


Fig. 5.1. (a) Unpassivated InSb IR PDs structures. Enlarged square express the detail structure of surface with dangling bonds, which acting as trap sites for the increase of surface leakage current. (b) A possible solution is passivation layer deposition on InSb IR PDs.

## 5.2. Motivation

Since 1980's, a great deal of efforts has been devoted to the development of InSb passivation materials including silicon nitride ( $\text{Si}_x\text{N}_y$ ) [2, 3], aluminium oxides ( $\text{Al}_2\text{O}_3$ ) [4, 5], silicon dioxide ( $\text{SiO}_2$ ) [6-12] and sulfur passivation [13-19].

Olcaytug *et al.* reported that deposition conditions of a total pressure, source gas flow rate, RF power and crystallographic orientation of InSb affect the quality of dielectrics [3]. This report also shows that the interface trap density at the midgap ( $D_{it}$ ) of  $\text{Si}_3\text{N}_4/\text{InSb}$  metal-oxide-semiconductor (MOS) structure is  $6.7 \times 10^{12} \text{ cm}^{-2}\text{eV}^{-1}$ . Ullrich *et al.* used the room temperature plasma enhanced reactive deposition to deposit the  $\text{Si}_3\text{N}_4$  films on InSb substrate and obtained the interface trap density of  $\sim 10^{12} \text{ cm}^{-2}\text{eV}^{-1}$  ranges by capacitance-voltage (C-V) measurement [2]. For the passivation of InSb PDs,  $\text{Si}_x\text{N}_y$  is not appropriate due to the high density of  $D_{it}$ . These days,  $\text{Al}_2\text{O}_3$  was investigated for the InSb passivation materials [4, 5].  $\text{Al}_2\text{O}_3$  was deposited using atomic layer deposition. They proposed the self cleaning effects as a result of chemical reactions between trimethylaluminium (TMAI) and native oxides. TMAI can react with  $\text{In}_2\text{O}_3$  and  $\text{Sb}_2\text{O}_3$  to form a volatile species. However, even though it has advantages of self cleaning effects, it also poor interface properties rather than that of  $\text{SiO}_2$ . They obtained the  $D_{it}$  of an order of  $10^{12} \text{ cm}^{-2}\text{eV}^{-1}$  ranges.

One of the most extensively studied dielectric was  $\text{SiO}_2$  due to the most superior interface properties with the interface trap density of  $10^{11} \text{ cm}^{-2}\text{eV}^{-1}$

ranges. However, deterioration of interface properties in deposited SiO<sub>2</sub> was reported. When the native oxides of InSb were exposed to silane (SiH<sub>4</sub>), chemical reactions between native oxides and SiH<sub>4</sub> were observed [7, 11]. These chemical reactions produced the elemental In and Sb, which have charges affecting to the surface band bending and acts as surface leakage conduction paths due to the low resistivity [20, 21]. These elements formation were also observed during SiO<sub>2</sub> films deposition above the temperature of 200 °C [22] and accelerated during heat treatments [22, 23]. H. Huff *et. al.*, reported that In and Sb atom can act as surface trap sites near the conduction band edge and the valence band edge, respectively [24]. The non-uniform SiO<sub>2</sub> films with a mean granularity size of 150 nm were also observed when SiH<sub>4</sub> was dissociated heterogeneously on the native oxides surface [6]. It is due to the nucleation sites formation from heterogeneously dissociated Si particles arriving on the surface.

Sulfur (S) passivation was widely used due to its advantages. It has extra 6 electrons in outer shells which can terminate the dangling bonds of (100) zincblende structures' surface. Thus, S passivation for InSb has been studied [13-19]. They reported that InSb surface was effectively terminated by S atoms, producing In-S and Sb-S bindings. However, the binding of In-S and Sb-S has weak binding strength, it can be decomposed easily [16]. Especially during annealing process, stronger bonding of In-S can be decomposed even at 300 °C. As a result, reliability problems can be occurred, introducing poor device reliability.

In this thesis, new passivation materials, zinc sulfid (ZnS), for high

interface properties and long-term reliability was proposed. It also effectively saturates the surface dangling bonds with S and it has also low fixed charge density ( $1.2 \times 10^{11} \text{ cm}^{-2}$ ) which affects to make inversion or accumulation layers near the surface [25]. It can be used as a self encapsulation material.

### 5.3. Experiment procedures

In order to investigate the interface properties of Au/ZnS/InSb metal-insulator-semiconductor (MIS) structures, ZnS was deposited on the wet cleaned n-InSb substrates using electron beam evaporation with a base pressure of  $2 \times 10^{-6}$  torr. The deposition rate was varied from 0.5 to 2.0 Å/sec. The Au metal gate contact was deposited on the ZnS films by electron beam evaporation using shadow mask with an area of  $1.9 \times 10^{-3}$  cm<sup>2</sup> and indium was used as a bottom contact. Capacitance-voltage (C-V) measurements were performed in a cryostat chamber at liquid N<sub>2</sub> temperature using Agilent 4980A LCR meter at a frequency of 1 MHz and a sweep rate of 0.1 V/sec. The interface trap density ( $D_{it}$ ) was evaluated by Terman's methods [26]. The chemical composition of ZnS films was determined by the Auger Electron Spectroscopy (AES) in an accelerating voltage of 5 kV and a current of 10 nA of the electron beam. Chemical binding states were examined by X-ray photoelectron spectroscopy with monochromatic Al K $\alpha$  with photon energy of 1486.6 eV. The base pressure of XPS measurements was  $4.8 \times 10^{-9}$  mbar. In order to identify the defects in the films, photoluminescence (PL) measurement was performed at 10 K in a He closed-cycle cryogenic system using a 325 nm line of He-Cd laser with 0.1 mW.

For the current-voltage (I-V) measurements, p-type InSb epitaxial layers were grown on n-type InSb substrate and intrinsic InSb epitaxial layers were inserted using LP-MOCVD as described in the Sec. 4.6.

More detailed process of mesa structures was described in the Sec. 2.3.

## 5.4. Interfacial properties of Au/ZnS/InSb MIS structures

### 5.4.1. Effects of deposition rate on interface trap density ( $D_{it}$ )

In order to obtain suitable ZnS passivation layers for our InSb substrates, zinc sulfide (ZnS) passivation layers with a thickness of 300 nm were deposited on InSb substrate. The deposition rate was varied from 0.5 to 2.0 A/sec. The interface trap density ( $D_{it}$ ) was evaluated by Terman's method. In Fig. 5.2 (a) showed the C-V curves of ZnS films deposited by different deposition rates. For the reference, ideal C-V curves of ZnS were also represented. At 0.5 A/sec, small stretched out of C-V curve (stiff slope) was observed and it became stretched out largely (smooth slope) with increasing deposition rate. It implies that large  $D_{it}$  was formed at the interface regions with increasing ZnS deposition rate. By comparison with a ideal C-V curves, the values of  $D_{it}$  was extracted using Terman's method. The extracted values of  $D_{it}$  were shown in Fig. 5.2 (b). At 0.5 A/sec,  $D_{it}$  of  $1.5 \times 10^{11} \text{ cm}^{-2}\text{eV}^{-1}$  was obtained, whereas it became increase to  $5.1 \times 10^{11} \text{ cm}^{-2}\text{eV}^{-1}$  with increasing ZnS deposition rate up to 2.0 A/sec. These values were much lower than that of  $\text{Si}_x\text{N}_y$  [2, 3] and  $\text{Al}_2\text{O}_3$  [4, 5] and is similar to that of  $\text{SiO}_2$  [6-12].

In order to investigate the superior interface properties to other dielectrics, chemical binding states were examined by XPS, representing that interface was terminated with S as shown in Fig. 5.3. Figure 5.3 (a) shows an XPS spectrum of In 3d peak obtained at the interface regions of the ZnS/InSb structures where ZnS was deposited at 0.5 A/sec.

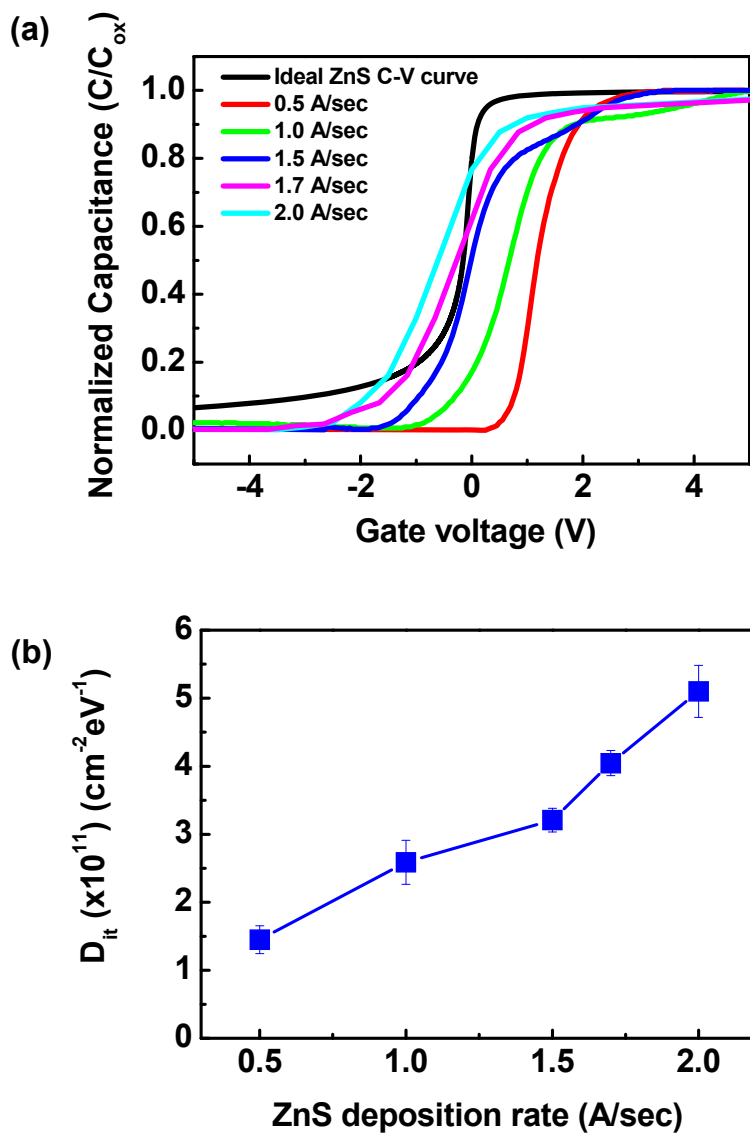


Fig. 5.2. (a) Capacitance-voltage curves of Au/ZnS/InSb MIS structures. The ideal C-V curves is inserted as a reference. (b) The calculated  $D_{it}$  at the mid gap as a function of ZnS deposition rate.

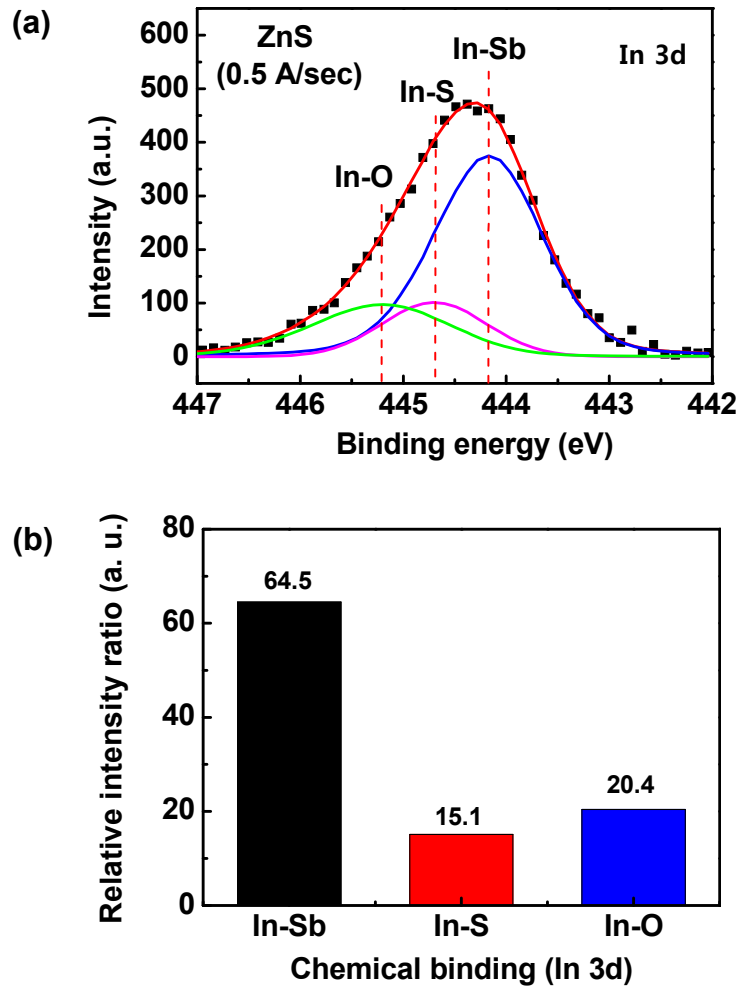


Fig. 5.3. (a) An XPS spectrum of In 3d region recorded at the interface regions of ZnS/InSb deposited at 0.5 A/sec. The deconvolution of In 3d spectra into three different chemically shifted components of In-Sb, In-S and In-O binding. (b) Relative intensity ratio of its binding area to total area of XPS peak.

The broad XPS peak was observed so the deconvolution of the peak was conducted to identify the chemical components at the interface regions. Three chemical bindings of In-Sb, In-S and In-O were considered and its position was 444.2 eV, 444.7 eV and 445.2 eV, respectively [27-29]. As represented in Fig. 5.3 (b), In-S binding was formed at the interface regions, affecting to reduce  $D_{it}$  by forming S termination which has almost 15 %. Each values of relatively intensity ratio were calculated by the ratio of each deconvoluted peak area to total In 3d peak area. Most of the bindings at the interface were In-Sb bindings which possess 64.5 % and In-O binding has 20.4 %.

#### **5.4.2. Effects of deposition rate on fixed charge density ( $N_f$ )**

Fixed charge density ( $N_f$ ) was evaluated from the relatively shift of C-V curves compared to that of ideal C-V curves. As shown in Fig. 5.2 (a), it was found that increasing the deposition rate caused parallel shifts of the C-V curves toward lower gate voltages, indicating that the quantity of fixed charges located at the interface were influenced by the deposition rate [30]. The flat-band voltages were obtained at the normalized capacitance of 0.8 which is a theoretical capacitance at zero-bias. It shows that the flat-band voltage was gradually decreased from +1.41 V for the sample deposited at 0.5 Å/sec to -0.16 V for the sample at 2.0 Å/sec as shown in Fig. 5.4.

Considering the work function difference between Au and InSb, C-V curve is shifted in parallel to 0.48 V with respect to the ideal C-V curve where fixed charge density is zero. Taking into account such metal-semiconductor work

function difference ( $\Phi_{ms}$ ), the fixed charge density ( $N_f$ ) was calculated from the flat-band voltage shift of the C-V curves as follows [30]

$$N_f = \frac{(\phi_{ms} - V_{fb}) \times C_p}{q} \quad [\text{eq. 5-1}]$$

where  $V_{fb}$  is the gate voltage to obtain the flat-band conditions,  $C_p$  is the capacitance of the passivation film in the accumulation region and  $q$  is the electronic charges. Figure 5.4, the calculated fixed charge density as a function of the ZnS deposition rate, shows that it decreased gradually from  $2.24 \times 10^{11} \text{ cm}^{-2}$  at  $0.5 \text{ \AA/sec}$  to  $1.64 \times 10^{10} \text{ cm}^{-2}$  at  $1.7 \text{ \AA/sec}$  in the negative range, and then it was converted to  $9.53 \times 10^{10} \text{ cm}^{-2}$  in the positive range at  $2.0 \text{ \AA/sec}$ . It implies that the positive fixed charges generated in the ZnS films compensated the residual negative fixed charges in InSb and that positive fixed charge density increased with increasing the deposition rate, the deposition rate of  $2.0 \text{ \AA/sec}$  it was more than enough to compensate all the residual negative fixed charges in InSb layer. Considering above fixed charge density, I believe that the sample deposited at  $1.7 \text{ \AA/sec}$  is close to the ideal flat-band condition of zero  $N_f$ .

### 5.4.3. Chemical composition analysis of ZnS films

I speculate that the positively charged defects were originated from native point defects in the ZnS film. Figure 5.5 shows the dependence of Zn/S ratio at the interface on the ZnS deposition rate, determined by Auger Electron Microscopy (AES) analysis. It shows that the Zn/S ratio increased linearly

from 0.93 for the sample deposited at 0.5 Å/sec to 1.35 for the sample at 2.0 Å/sec, implying that ZnS film became more S-deficient at higher deposition rate. This effect was explained by two reasons. First, it has been reported that the vapor pressure between Zn and S is different and the vapor pressure of S at a given temperature has six orders of magnitude higher values than that of Zn. At higher deposition rates caused the more evaporation of S than that of Zn at a source, introducing S deficient ZnS film formation. This kind of effects was well known for the Al<sub>2</sub>O<sub>3</sub> and SiO<sub>2</sub> deposition by electron beam evaporation. Second, as the deposition rate was increased, more Zn and S vapor species were evaporated from the source and contribute to the increase of substrate temperature, thereby higher vapor pressure of S can re-evaporate from the substrate surface before incorporating into the ZnS films. Similar result was reported [31].

#### **5.4.4. Defect origin of S-deficient ZnS films**

In the previous sections, stoichiometry of ZnS films became S-deficient with increasing deposition rate as shown in Fig. 5.5. In order to investigate the origin of defects in S-deficient ZnS films, PL measurements were conducted at 10 K. Figure 5.6 shows PL emission spectra of the ZnS films deposited at different rates. They showed multiple broad peaks in the range from 350 nm to 600 nm. For clearer indexing of the peaks Gaussian curve fitting was applied to deconvolute the PL spectrum of the sample. Four PL peak positions were observed which were located at 365 nm, 396 nm, 420 nm and 460 nm. These PL peak position were attributed to sulphur interstitial (I<sub>S</sub>) [32], sulphur vacancy (V<sub>S</sub>) [33-35], zinc vacancy (V<sub>Zn</sub>) and zinc interstitial

( $I_{Zn}$ ) [32, 35, 36], respectively. It was clear that the 396 nm and 420 nm peaks are strong for all the samples, which is consistent with a theoretical calculation of the defect formation energy in ZnS film [37]. Based on the calculation, Varley *et al.* reported that  $V_S$  and  $V_{Zn}$  are dominant native defects in S-deficient ZnS film. The PL result also shows that the intensity of the 396 nm peak increased with increasing deposition rate while the intensity of the other peaks were unchanged, indicating that the concentration of  $V_S$  defect increased with increasing the deposition rate. This agrees with the result that more S-deficient ZnS film was deposited at the higher deposition rates, as shown in Fig. 5.5. Based on the results above, I considered that the C-V curve shifts towards lower gate voltage with increasing the deposition rate, as shown in Fig. 5.2 (a), was due to the formation of  $V_S$ , a positively charged defect, in the S-deficient ZnS films.

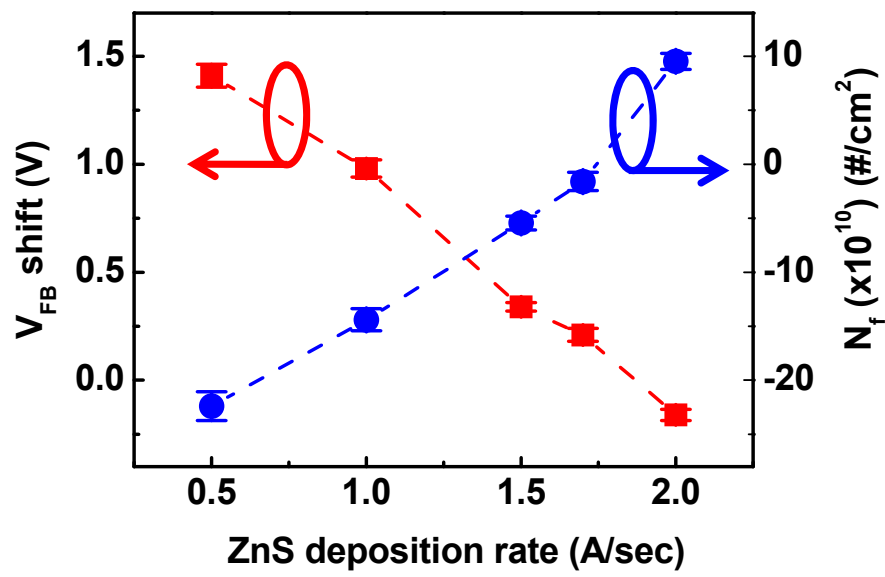


Fig. 5.4. Flat band voltage shift and fixed charge density ( $N_f$ ) calculated from flat band voltage shifts as a function as ZnS deposition rate.

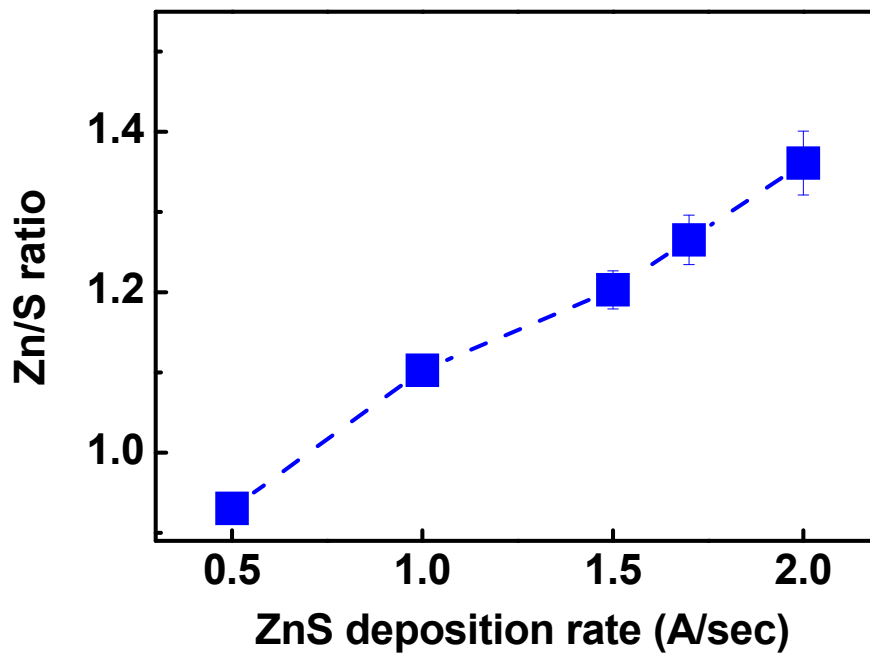


Fig. 5.5. Intensity ratio of Zn/S at the interface of ZnS/InSb obtained from AES depth profiles measurements

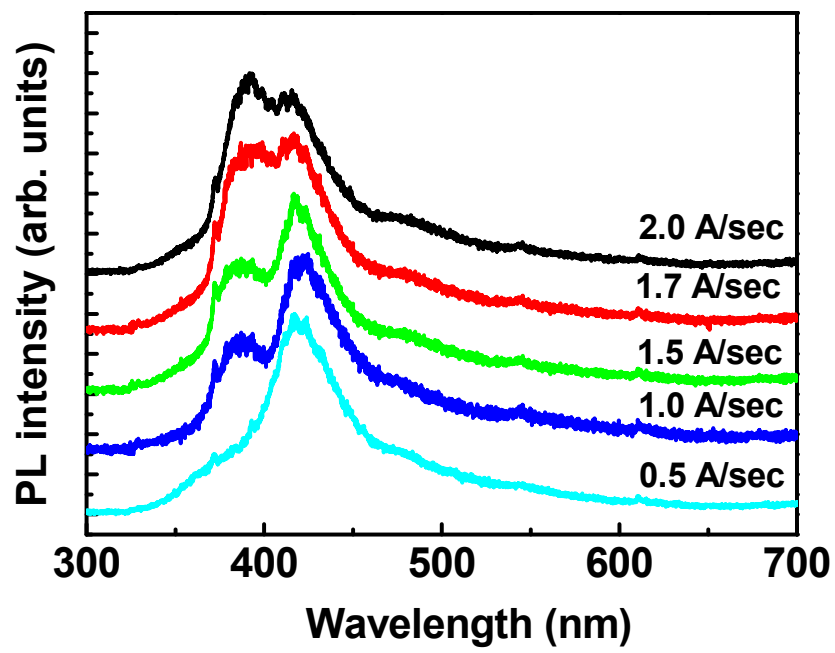


Fig. 5.6. PL emission spectra of ZnS films deposited at different deposition rates.

## 5.5. Surface leakage currents of ZnS passivated InSb PDs

### 5.5.1. Theoretical background

The effectiveness of passivation is commonly evaluated using variable area diode array (VADA) method [38]. Because the perimeter related current is associated with a high density of surface or interface states at the semiconductor-air or semiconductor-passivation interface. For the square mesa diode, the total dark current density is the summation of bulk component of dark current and the surface component of dark current. If the bulk component of dark current is dominant, the VADA curves will have a slope closed to zero, which shows not slope. However, surface component of the dark current become dominant mechanism, then the slope of VADA experiments will have a slope, which means the increase in the dark current density for the smaller devices. Hence, smaller area diodes will be more sensitive to perimeter or surface effects than diodes of the same slope but larger diode sizes. The perimeter to area ratio ( $P/A$ ) is inversely proportional to the diode feature sizes and hence magnifies the surface or perimeter related issues, when parameters such as current density or  $1/R_oA$  are plotted against  $P/A$ . The total or effective zero bias resistance area products ( $R_oA$ ) for the diodes are expressed below:

$$\frac{1}{R_oA} = \left[ \left( \frac{1}{R_oA} \right)_{bulk} + \frac{1}{r_{surface}} \frac{P}{A} \right] \quad [\text{eq. 5-2}]$$

where  $(R_oA)_{\text{bulk}}$  is the bulk  $R_oA$  contribution in  $\Omega\text{cm}^2$  obtained from the intercept of the linear fit with the  $1/R_oA$  axis,  $r_{\text{surface}}$  is the surface resistivity in  $\Omega\text{cm}$  for the diode and is obtained from the inverse slope of the linear fit of  $1/R_oA$  versus  $P/A$  data. Higher values of surface resistivity indicate weaker dependence of the diode's characteristics on the surface effects. The schematic illustration was represented in Fig. 5.7. The optical image of the sample for VADA measurements was represented in Fig. 5.8.

### **5.5.2. The dependence of deposition rates on the surface leakage currents**

The effectiveness of ZnS passivation layer deposited with different deposition rates was investigated using current-voltage (I-V) measurements. The mesa diode structures of different sizes in the range from  $300 \times 300$  to  $800 \times 800 \mu\text{m}^2$  were fabricated to measure the surface effects on the surface leakage currents. Figure 5.9 (a) shows the results of VADA measurements.

From the results of VADA measurement as shown in Fig. 5.9 (b), the dark current density,  $1/R_oA$ , was observed to increase for smaller diode sizes (high  $P/A$ ), indicating the surface leakage current is more dominant for smaller diode. Among the ZnS deposition conditions, InSb samples deposited at  $1.7\text{\AA}/\text{sec}$  has smooth slope, representing the most effective deposition conditions. The surface resistivity ( $r_{\text{surface}}$ ) calculated from the inverse slope of the  $1/R_oA$  vs  $P/A$  revealed that among the samples, the diode with ZnS passivation layer deposited at  $1.7 \text{\AA}/\text{sec}$  showed the largest  $r_{\text{surface}}$  value of

52.0  $\Omega$  cm which is somewhat higher than the value, 33  $\Omega$  cm, reported for silicon dioxide passivated type II InAs/GaSb photodiodes [39]. However, the values of other deposition conditions has lower surface resistivity, indicating that ZnS passivation layers deposited at 0.5, 1.0, 1.5 and 2.0 A/sec have poor qualities to restrict the surface leakage current. These results were consistent with C-V data that MIS structure with ZnS passivation layer deposited at 1.7 A/sec was close to the ideal flat-band condition. At other deposition conditions, inversion or accumulation was generated near ZnS/InSb interface, making conducting path for the surface leakage current. Detailed illustration was represented in Fig. 5.10. Before depositing ZnS passivation layers, InSb surface contained native oxides, which were spontaneously formed. It contains the negative charges which were confirmed by many other researchers [24, 40, 41]. These negative charges make an accumulation layer for p-InSb regions and depletion layer for n-InSb regions, acting as electrical surface leakage current path as represented in Fig. 5.10 (a). However, the negative charges on the native oxides were compensated by the positive charges on the ZnS films when ZnS films were deposited on the unpassivated InSb mesa structures as shown in Fig. 5.10 (b). This passivation produces the charge compensation at the interface regions to make near flat band condition where surface leakage currents were inhibited.

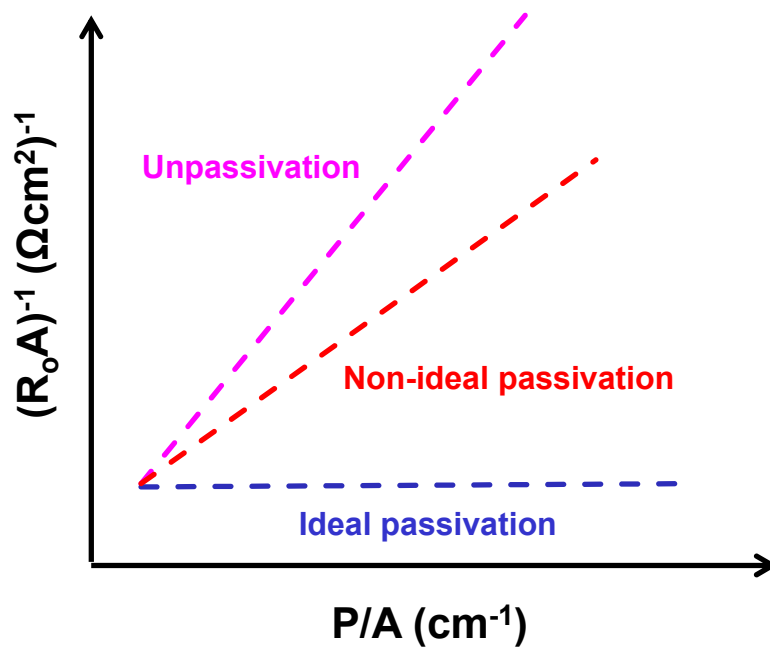


Fig. 5.7. Schematic illustration of  $1/R_o A$  versus perimeter to area ( $P/A$ ) ratio. This graph represents the dependence of ideal passivation, non-ideal passivation and unpassivation on  $R_o A$  products.

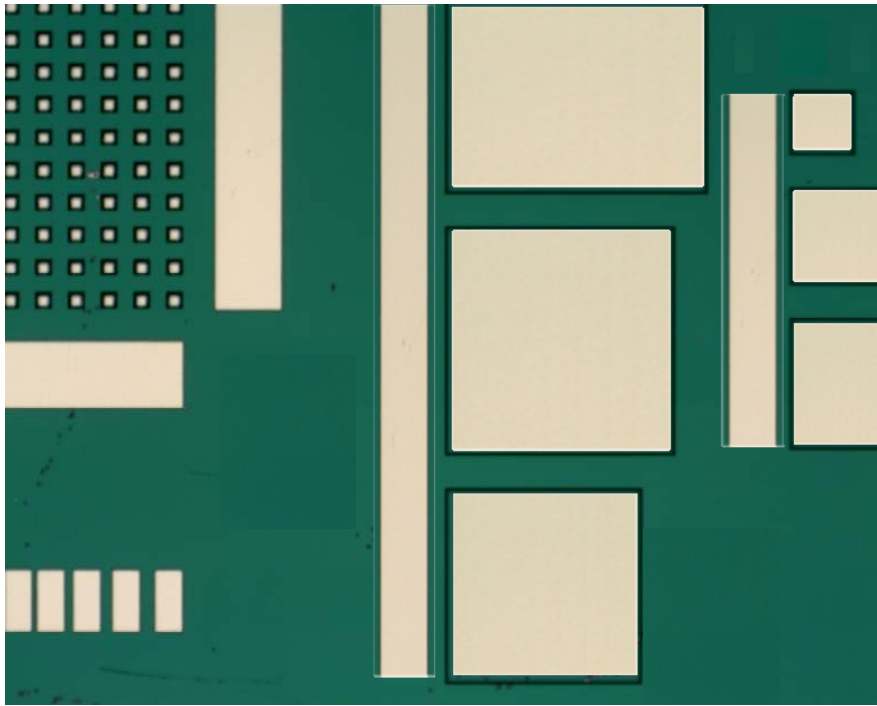


Fig. 5.8. Optical microscope image of the sample for VADA measurements

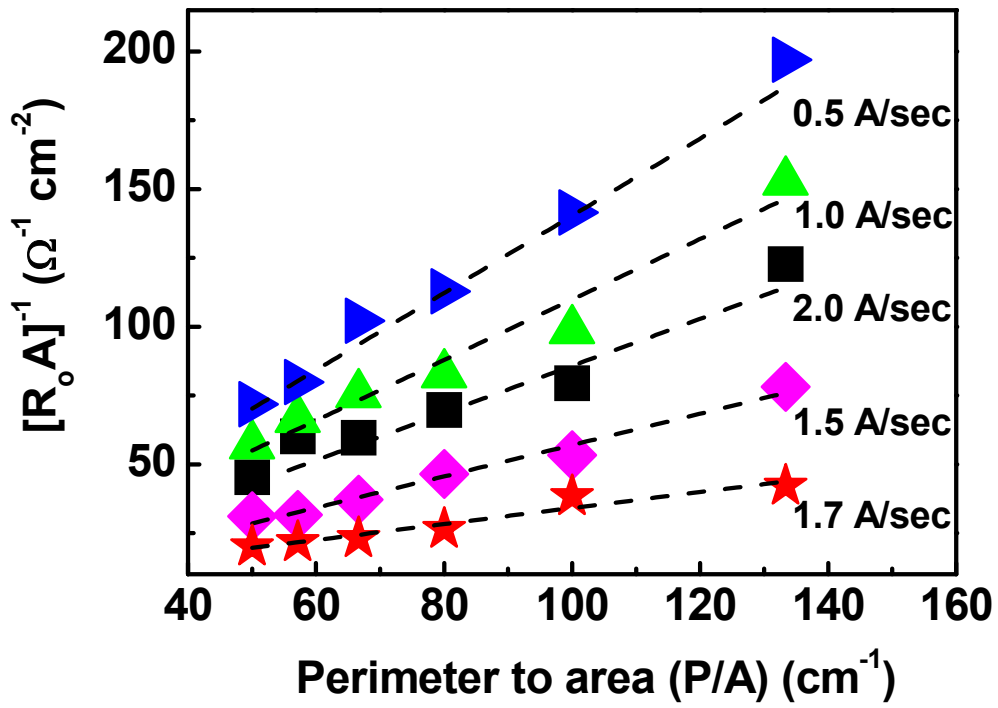


Fig. 5.9. (a) I-V curves for the ZnS passivated InSb pn IR PDs (b) dependence of  $1/R_oA$  vs P/A ratio for the InSb pn diodes

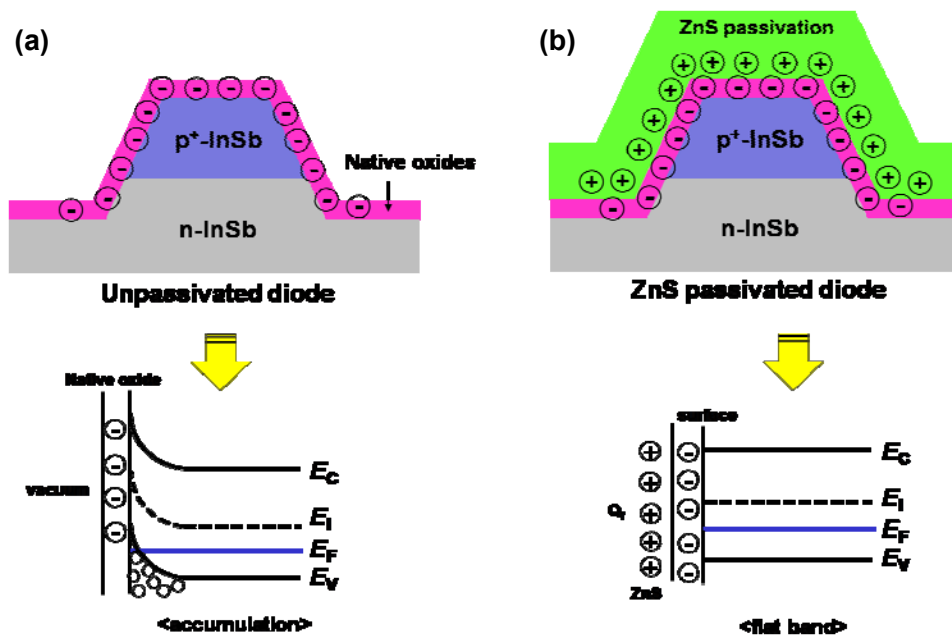


Fig. 5.10. Schematic images of (a) unpassivated InSb pn structure and (b) ZnS passivated InSb pin structure and corresponding band diagrams were represented.

## 5.6. Device performance

### 5.6.1. Dark current

Dark current is very important parameter in photodiode which represents device performance. In photodiode technology, high signal to noise (S/N) ratio is required in order to obtain high resolution of devices. Dark current was related to the noise intensity so the reduction of dark current is key issue. In order to investigate the dark current level in our sample, pn structures were grown using LP-MOCVD as shown in Fig. 5.11. The detailed device fabrication process was described in chapter 2. Two types of samples were prepared to compare the effectiveness of ZnS passivation. First sample was mesa type InSb pin based photodiode structures without surface passivation.

On the other hand, second sample was also mesa type InSb pn based photodiode structures but passivated ZnS with deposition rate of 1.7 Å/sec where  $N_f$  was significantly reduced. Figure 5.12 (a) shows the bias dependent dark current density for the unpassivated and ZnS passivated photodiodes measured at 80 K. ZnS passivated samples shows a reduction of almost one order of magnitude in dark current density compared with the unpassivated one. It was attributed by the surface effect because dark current was controlled by the bulk limited and surface limited as described in equation 5-2. In case of bulk limited dark current, it was also controlled by the diffusion current ( $I_{diffu}$ ), generation-recombination current ( $I_{G-R}$ ), trap assisted tunneling current ( $I_{TAT}$ ) and band to band tunneling current ( $I_{BTB}$ ) [42]. Figure 5. 12 (b)

shows the corresponding differential resistance area product at zero bias ( $R_oA$ ) versus applied voltage of two samples. When the mesa type InSb photodiodes were passivated with ZnS films, the  $R_oA$  value of  $1.5 \times 10^4 \Omega \text{ cm}^2$  was obtained when ZnS films were deposited whereas, it was significantly decreased in unpassivated InSb sample. Its value was around  $20 \Omega \text{ cm}^2$ . This value was comparable with other reported results. When the gate ring structures for the surface potential control was applied to the device structures,  $5 \times 10^4 \Omega \text{ cm}^2$  was obtained when  $\text{SiO}_2$  was deposited using low temperature CVD [43] and photo-CVD[44]. The value of  $1.2 \times 10^4 \Omega \text{ cm}^2$  were also obtained when siliconoxynitride ( $\text{Si}_x\text{N}_y\text{O}_z$ ) was used as a passivation layers[45]. However, in this study, gate ring structures were not applied to the device because the surface potential was intentionally controlled by the fixed charges by changing the stoichiometric of ZnS films, which shows the much higher  $R_oA$  values compared to that of reported values of  $\sim 10^3 \Omega \text{ cm}^2$  [46].

### **5.6.2. Spectral response**

In order to confirm the effectiveness of ZnS passivation on mesa type InSb photodiodes, spectral response, which is normally called by photocurrent, photo response, measurements were performed. Spectral response measurement setup was consisted with a Fourier transform infrared spectrometer (FTIR, Vertex 80v), cryostat temperature controller (Lakeshore), current amplifier (Keithley 428 preamplifier), detector controller and computer. The measured diodes image was shown in Fig. 5. 13.

Figure 5.14 (a) shows the spectral response of three samples for unpassivated and SiO<sub>2</sub> and ZnS passivated InSb photodiodes measured at 80 K under zero bias. Spectral response of two samples represents that the zero bias cut-off wavelength was almost 5.5 μm which well matched to the InSb band gap of 0.225 eV. It should be note that the relative intensity of spectral response was almost 10 times increased when ZnS passivation was conducted. From the temperature dependence spectral response as shown in Fig. 5.14 (b-c), similar spectral response intensity was observed with increasing temperature to 100 K for two samples, indicating that high quality of InSb epitaxial layers can be grown in this experiment. With increasing temperature further, spectral response was significantly decreased and cut-off wavelength was shifted towards longer wavelength region. In case of ZnS passivated sample as shown in Fig 5.14 (c), spectral response was detected even at 220 K with a cut-off wavelength of 6.6 μm. By comparing the temperature dependence spectral response of two samples, spectral response was detected at 180 K in unpassivated sample while it was detected at 220 K in passivated sample, indicating that surface leakage current is dominant role to improve device performances. Over 220 K for unpassivated sample and 260 K for passivated sample, the spectral responses were not detected due to the thermal noise.

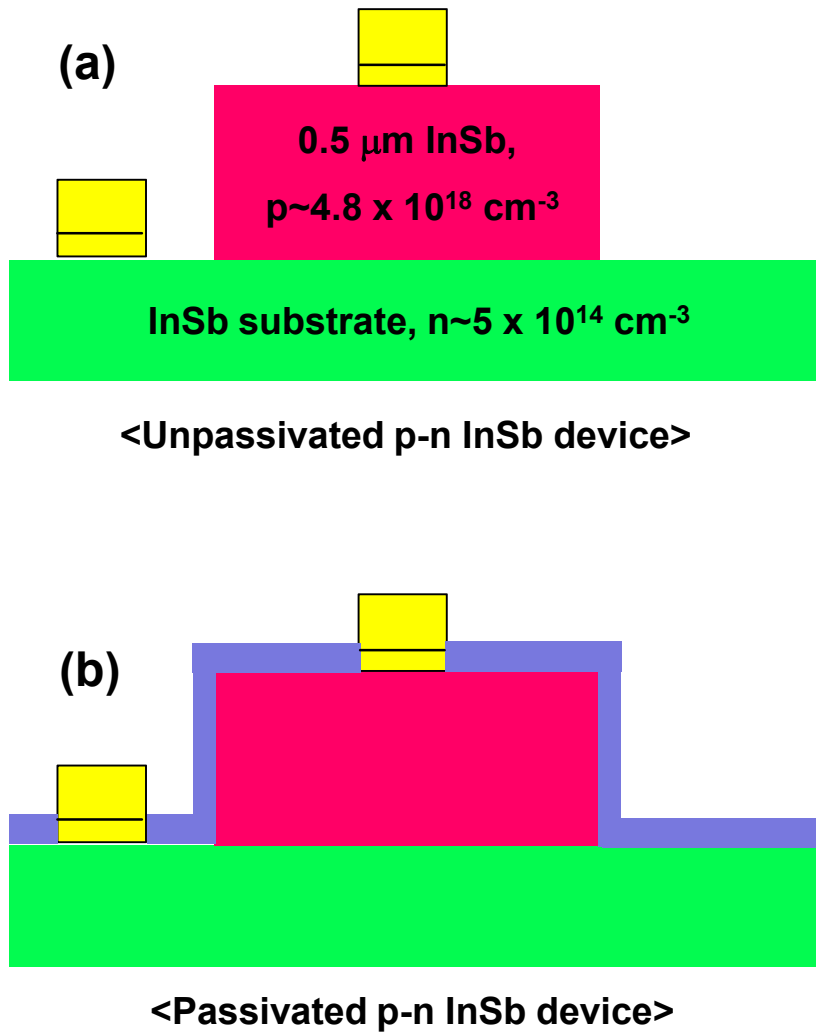


Fig. 5.11. Schematic images of (a) unpassivated mesa type InSb pn structure and (b) ZnS passivated mesa type InSb pn structure.

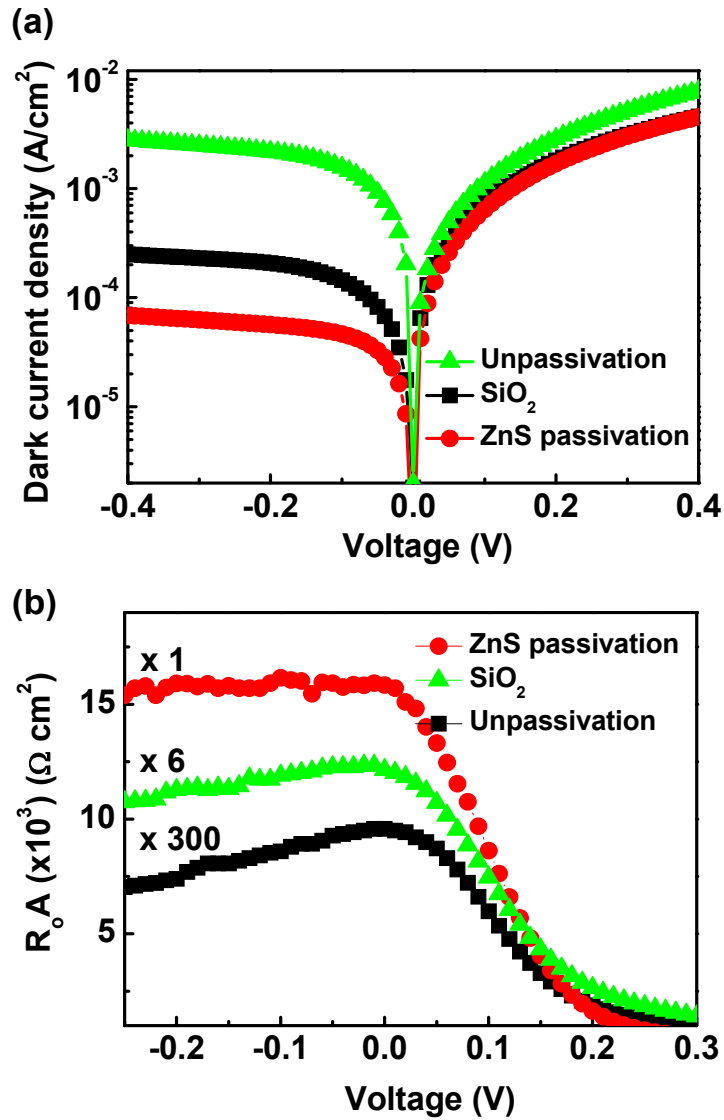


Fig. 5.12. (a) Dark current density versus applied voltage of the unpassivated, SiO<sub>2</sub> and the ZnS passivated photodiodes measured at 80 K. (b) Differential resistance area product at zero bias (R<sub>0</sub>A) vs applied voltage of three samples.

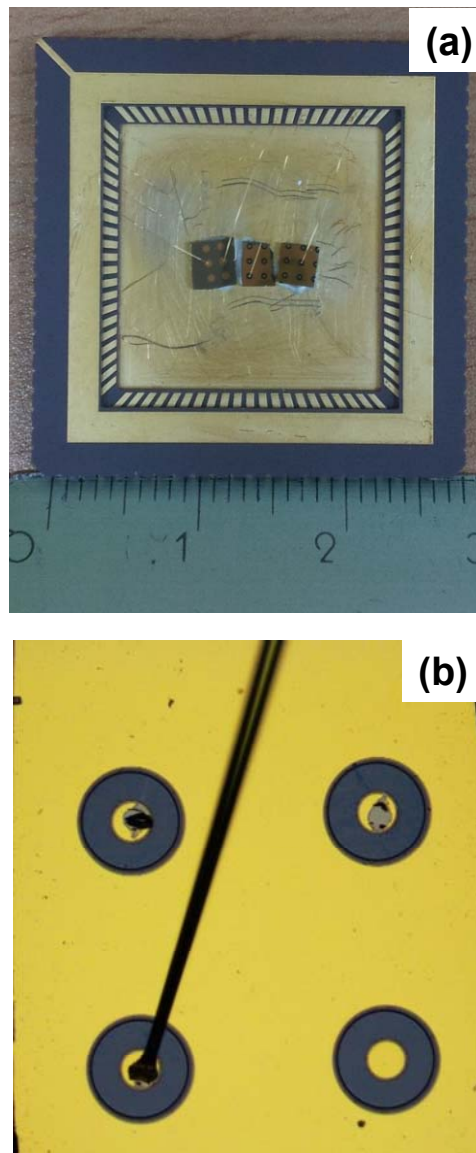


Fig. 5.13. (a) Photograph of measured samples. Contacts were connected by Au wiring to the sample holder. (b) Optical microscope image of ZnS passivated InSb photodiodes.

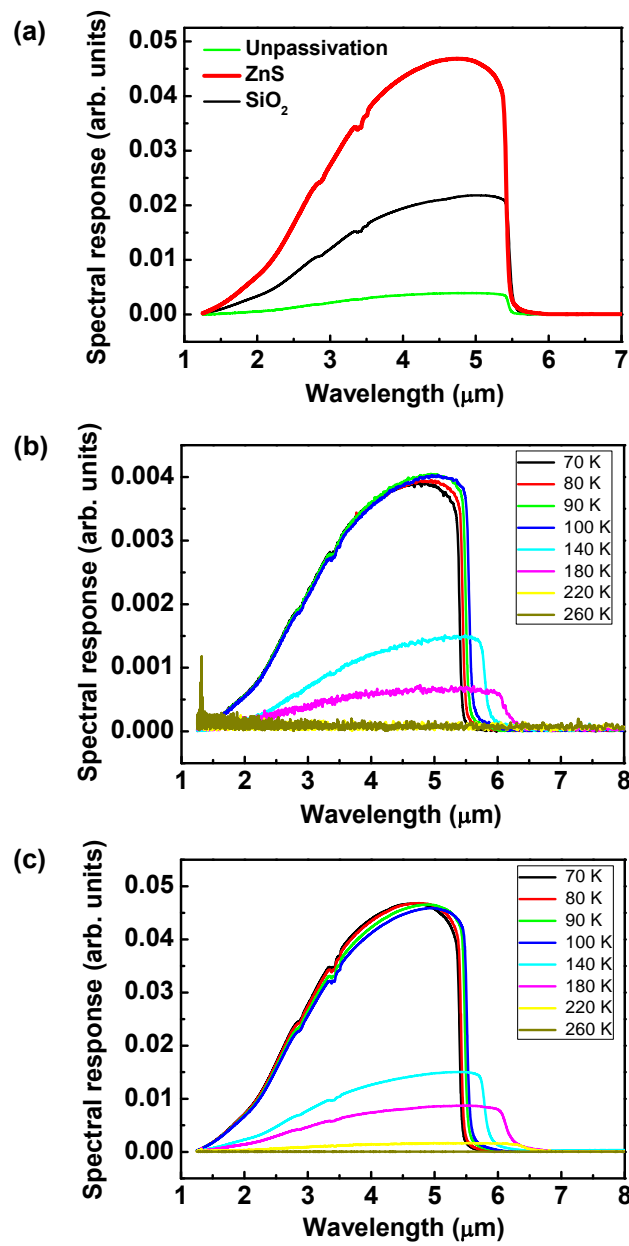


Fig. 5.14. (a) Spectral response of unpassivated and passivated sample. Temperature dependence of spectral response of (b) unpassivated and (c) passivated samples.

### 5.6.3. Responsivity and detectivity (D\*)

Finally InSb photodiode performance was determined by measuring responsivity and detectivity.

The responsivity of the IR photodiodes was defined as the ratio of the electrical signal to the incident radiation power. Electrical signal was obtained from measuring the voltage or current. So, the unit of responsivity was expressed either V/W or A/W. The responsivity was dependent on wavelength. The responsivity varies with incident photon energy, device bandgap, absorption coefficient and quantum efficiency of the material and determined the peak spectral responsivity of a given detector by using equation [5-1]

$$R_{\lambda} = (\text{Electrical output}) / (\text{Radiant input power}) = (I_{s,\lambda}) / (\Delta P_{\lambda}) \text{ [A/W]} \quad [\text{eq. 5-1}]$$

where  $\Delta P_{\lambda}$  was described as incidence rms optical power shown in eq. 5-2.

$$\Delta P_{\lambda} = \left( \frac{A_d A_b}{\pi R^2} \right) T_w T_{\lambda} W_{\lambda} M_f \Delta \lambda \quad [\text{eq. 5-2}]$$

where,  $A_d$  is detector optical area [ $\text{cm}^2$ ],  $A_b$  is blackbody aperture diameter [ $\text{cm}^2$ ] of 0.5 inch,  $R$  is distance from the detector to blackbody aperture where 20 cm in this case,  $T_w$  is window transmittance (0.7),  $T_{\lambda}$  is maximum

transmittance of optical band pass filter,  $M_f$  is modulation factor (0.5),  $\Delta\lambda$  is optical transmitting band [ $\mu\text{m}$ ] and  $W_\lambda$  is spectral radiant power which is described in eq. 5-3.

$$W_\lambda = \frac{C_1}{\lambda^5} \frac{1}{\exp(C_2 / \lambda T_{bb}) - 1} \quad [\text{eq. 5-3}]$$

where,  $C_1$  is  $3.7418 \times 10^4$  [ $\text{W}\mu\text{m}^4/\text{cm}^2$ ],  $C_2$  is  $1.4387 \times 10^4$  [ $\mu\text{mK}$ ] and  $T_{bb}$  is blackbody source temperature [ $\text{K}$ ] where 1173 K in this measurements.

Detectivity (normally represented  $D^*$ ) for photovoltaic photodetector can be expressed as

$$D^* = \frac{R \times \sqrt{\text{Area}}}{\text{Noise} / \sqrt{\Delta f}} = \frac{\sqrt{A_d \Delta f}}{\sqrt{I_n^2}} R_\lambda \quad [\text{eq. 5-4}]$$

where,  $R$  is the responsivity,  $I$  is dark current, and noise is background device noise level measured during the measurement. The unit of  $D^*$  was described as  $\text{cmHz}^{1/2}/\text{W}$

The responsivity of three samples was represented in Fig. 5.15 (a). Responsivity signal was observed in the wavelength range of 1.5 ~ 5.18  $\mu\text{m}$  ranges. Less 1 nm and over 5.18  $\mu\text{m}$  was not measured due to the equipment limitation. When InSb device was passivated with ZnS films under optimized

conditions, responsivity was increased but low responsivity intensity was observed when SiO<sub>2</sub> films were deposited and unpassivation was conducted. As shown in Fig. 5.15 (b), detectivity was measured for three samples. In order to obtain detectivity, background device noise level has to be measured as described in eq. 5-4. However, due to the equipment limitation, accurate noise level measurement has not been conducted.

So I can compare the relative D\* among three samples. Maximum D\* was observed at 5.18 μm for all samples. When InSb samples were passivated by ZnS films, D\* of 10<sup>8</sup> cmHz<sup>1/2</sup>/W order of magnitude was observed and its intensity of D\* was almost keep constant when the reverse bias was applied to -0.6 V. In case of SiO<sub>2</sub> and unpassivation samples, lower D\* was observed. D\* of low 10<sup>7</sup> cmHz<sup>1/2</sup>/W was observed. The reduction of D\* for SiO<sub>2</sub> and unpassivation samples were due to the increase of surface leakage current as represented in eq. 5-4 as D\* was influenced by the dark current density. In case of both two samples, the surface leakage current was increased due to the ineffective passivation, contributing to the reduction of D\*.

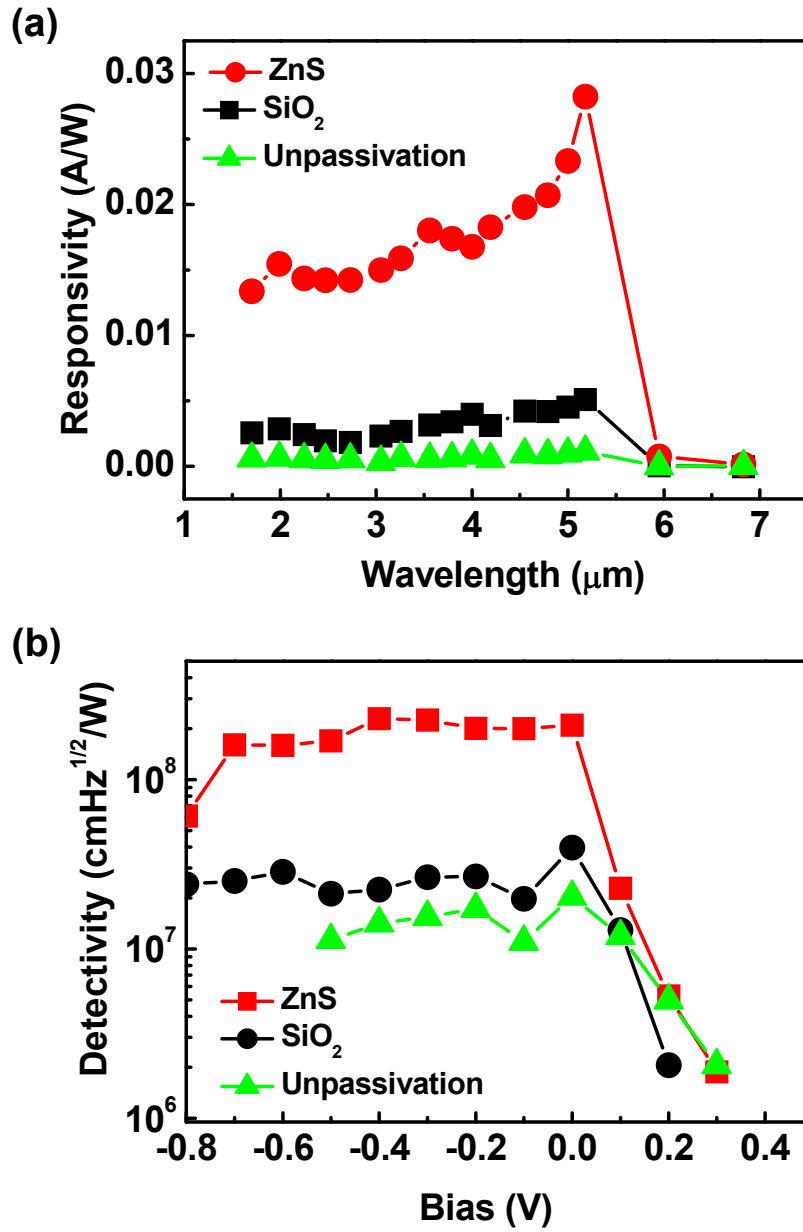


Fig. 5.15. (a) Responsivity and (b) detectivity ( $D^*$ ) of three samples measured at 77 K under zero bias.

## 5.7. Summary

In this chapter, in order to deposit dielectric film with superior interfacial quality to the other reported dielectrics, S-based dielectrics such as ZnS was chosen for the effective passivating the dangling bonds as a passivation layers. ZnS showed the similar  $D_{it}$  of  $\sim 10^{11} \text{ cm}^{-2}\text{eV}^{-1}$  which is similar values of that of  $\text{SiO}_2$  deposited photo-CVD. The origin of low  $D_{it}$  was originated from S termination with InSb bonding, producing In-S and Sb-S. With increasing deposition rate,  $D_{it}$  was slightly increased but  $D_{it}$  has the lower values of  $5 \times 10^{11} \text{ cm}^{-2}\text{eV}^{-1}$  in all deposition conditions. On the other hand, the lowest  $N_f$  was observed at 1.5 A/sec deposition condition which is contrast to the result of  $D_{it}$ . This was due to the charge compensation effects. With increasing deposition rate, ZnS films became S-deficient films due to the vapor pressure differences between Zn and S. From the PL measurements, amount of sulfur vacancy was generated with increasing deposition temperature. These defects showed the positive charges in the ZnS films. As a result, InSb surface contained the negative charges can be compensated by the positive charges by depositing ZnS films. Charge balanced devices have the lowest surface leakage currents but it was increased in other charge unbalanced devices due to the accumulation or inversion layer formation, which acts as electrically conducting path.

By surface passivating with ZnS films, device performance was improved due to the restriction of surface effects which contributes to increase dark current. When ZnS films were deposited on mesa type InSb photodiodes, almost two orders of magnitude in dark current was reduced. The reduction

of dark current was also influence on the IR photodiode device performances. When ZnS film were deposited which is effective way to suppress surface leakage current, spectral response, responsivity and detectivity was improved by comparing to that of SiO<sub>2</sub> and unpassivation samples.

## 5.8. Bibliography

- [1] E. A. Plis, M. N. Kutty, and S. Krishna, "Passivation techniques for InAs/GaSb strained layer superlattice detectors," *Laser & Photonics Reviews*, vol. 7, pp. 45-59, 2013.
- [2] B. Ullrich, F. Kuchar, R. Meisels, F. Olcaytug, and A. Jachimowicz, "Capacitance-voltage measurements on a p-type InSb metal/insulator/semiconductor structure with Si<sub>3</sub>N<sub>4</sub> as the insulator," *Thin Solid Films*, vol. 168, pp. 157-163, 1989.
- [3] F. Olcaytug, K. Riedling, and W. Fallmann, "C/V measurements of MIS structures on n-InSb formed by room temperature reactive deposition of Si<sub>3</sub>N<sub>4</sub>," *Electronics Letters*, vol. 16, pp. 677-678, 1980.
- [4] C. Hou, M. Chen, C. Chang, T. Wu, and C. Chiang, "Interfacial cleaning effects in passivating InSb with Al<sub>2</sub>O<sub>3</sub> by atomic layer deposition," *Electrochemical and Solid-State Letters*, vol. 11, pp. D60-D63, 2008.
- [5] H. D. Trinh, Y. C. Lin, E. Y. Chang, C.-T. Lee, S.-Y. Wang, H. Q. Nguyen, *et al.*, "Electrical Characteristics of MOSCAPs and the Effect of Postdeposition Annealing Temperatures," *Electron Devices, IEEE Transactions on*, vol. 60, pp. 1555-1560, 2013.
- [6] J. Langan and C. Viswanathan, "Characterization of improved InSb interfaces," *Journal of Vacuum Science and Technology*, vol. 16, pp. 1474-1477, 1979.
- [7] R. Vasquez and F. Grunthaner, "XPS study of interface formation of CVD SiO<sub>2</sub> on InSb," *Journal of Vacuum Science and Technology*, vol.

- 19, pp. 431-436, 1981.
- [8] Y. Avigal, J. Bregman, and Y. Shapira, "Correlation between electrical and compositional properties of SiO<sub>2</sub>/InSb interfaces," *Journal of applied physics*, vol. 63, pp. 430-434, 1988.
- [9] K. Takahashi, A. Onozuka, and Y. Tanaka, "Characterization of InSb interface with oxide films," *Japanese journal of applied physics*, vol. 35, p. 61, 1996.
- [10] K. Germanova and E. Valcheva, "Characterization of interface electrical properties in SiO<sub>2</sub>/InSb metal/insulator/semiconductor structures prepared by plasma-enhanced chemical vapour deposition," *Thin solid films*, vol. 148, pp. 243-250, 1987.
- [11] R. P. Vasquez and F. J. Grunthaner, "Chemical composition of the SiO<sub>2</sub>/InSb interface as determined by x-ray photoelectron spectroscopy," *Journal of Applied Physics*, vol. 52, pp. 3509-3514, 1981.
- [12] J. D. Langan, "Study and characterization of semiconductor surfaces and interfaces," *Ph. D thesis, University of California, Santa Barbara, USA*, 1979.
- [13] G. Eftekhari, "The influence of rapid thermal annealing and sulfur passivation on the electrical characteristics of anodically grown InSb MOS structures," *Thin solid films*, vol. 278, pp. 150-154, 1996.
- [14] T. V. Lvova, A. L. Shakhmin, I. V. Sedova, and M. V. Lebedev, "Sulfur passivation of InSb (100) surfaces: Comparison of aqueous and alcoholic ammonium sulfide solutions using X-ray photoemission spectroscopy," *Applied Surface Science*, vol. 311, pp. 300-307, 2014.

- [15] S. Ichikawa, Y. Suzuki, N. Sanada, N. Utsumi, T. Yamaguchi, X. Gong, *et al.*, "A (NH<sub>4</sub>)<sub>2</sub>S<sub>x</sub>-treated InSb (001) surface studied by using x-ray photoelectron spectroscopy, low-energy electron diffraction, and inverse photoemission spectroscopy," *Journal of Vacuum Science & Technology A*, vol. 17, pp. 421-424, 1999.
- [16] M. V. Lebedev, M. Shimomura, and Y. Fukuda, "Chemical analysis of a sulfur-treated InSb (111) A surface by XPS," *Surface and Interface Analysis*, vol. 42, pp. 791-794, 2010.
- [17] P. King, T. D. Veal, M. J. Lowe, and C. F. McConville, "Surface electronic properties of clean and S-terminated InSb (001) and (111) B," *Journal of Applied Physics*, vol. 104, p. 083709, 2008.
- [18] D. M. Zhernokletov, H. Dong, B. Brennan, J. Kim, and R. M. Wallace, "Optimization of the ammonium sulfide (NH<sub>4</sub>)<sub>2</sub>S passivation process on InSb (111) A," *Journal of Vacuum Science & Technology B*, vol. 30, p. 04E103, 2012.
- [19] T. Lvova, M. Dunaevskii, M. Lebedev, A. Shakhmin, I. Sedova, and S. Ivanov, "Chemical passivation of InSb (100) substrates in aqueous solutions of sodium sulfide," *Semiconductors*, vol. 47, pp. 721-727, 2013.
- [20] T. P. Sun, S. C. Lee, and S. J. Yang, "The electrical characteristics of metal/SiO<sub>2</sub>/InSb capacitor fabricated by photoenhanced chemical vapor deposition," *Journal of Vacuum Science & Technology B*, vol. 7, pp. 1115-1121, 1989.
- [21] F. M. Mohammedy and M. J. Deen, "Growth and fabrication issues of GaSb-based detectors," *Journal of Materials Science: Materials in*

- Electronics*, vol. 20, pp. 1039-1058, 2009.
- [22] J. Lee, S. Park, J. Kim, C. Yang, S. Kim, C. Seok, *et al.*, "Comparative analysis of oxide phase formation and its effects on electrical properties of SiO<sub>2</sub>/InSb metal-oxide-semiconductor structures," *Thin Solid Films*, vol. 520, pp. 5382-5385, 2012.
- [23] T. P. Sun, S. C. Lee, K. C. Liu, Y. M. Pang, and S. J. Yang, "High-performance metal/SiO<sub>2</sub>/InSb capacitor fabricated by photoenhanced chemical vapor deposition," *Journal of applied physics*, vol. 68, pp. 3701-3706, 1990.
- [24] H. Huff, S. Kawaji, and H. C. Gatos, "Field effect measurements on the A and B {111} surfaces of indium antimonide," *Surface Science*, vol. 5, pp. 399-409, 1966.
- [25] Y.-H. Kim, S.-H. Bae, H. C. Lee, and C. K. Kim, "Surface leakage current analysis of ion implanted ZnS-passivated n-on-p HgCdTe diodes in weak inversion," *Journal of Electronic Materials*, vol. 29, pp. 832-836, 2000.
- [26] L. M. Terman, "An investigation of surface states at a silicon/silicon oxide interface employing metal-oxide-silicon diodes," *Solid-State Electronics*, vol. 5, pp. 285-299, 1962.
- [27] L.-W. Lai, J.-T. Chen, L.-R. Lou, C.-H. Wu, and C.-T. Lee, "Performance Improvement of (NH<sub>4</sub>)<sub>2</sub>S<sub>x</sub>-Treated III–V Compounds Multijunction Solar Cell Using Surface Treatment," *Journal of The Electrochemical Society*, vol. 155, pp. B1270-B1273, 2008.
- [28] X. Tang, R. Van Welzenis, F. Van Setten, and A. Bosch, "Oxidation of the InSb surface at room temperature," *Semiconductor science and*

- technology*, vol. 1, p. 355, 1986.
- [29] D. Datta, S. Garg, B. Satpati, P. Sahoo, A. Kanjilal, S. Dhara, *et al.*, "60 keV Ar<sup>+</sup>-ion induced modification of microstructural, compositional, and vibrational properties of InSb," *Journal of Applied Physics*, vol. 116, p. 143502, 2014.
- [30] T. Hori, *Gate dielectrics and MOS ULSIs*: Springer, 1997.
- [31] R. Bunshah, R. Nimmagadda, W. Dunford, B. Movchan, A. Demchishin, and N. Chursanov, "Structure and properties of refractory compounds deposited by electron beam evaporation," *Thin Solid Films*, vol. 54, pp. 85-106, 1978.
- [32] A. K. Kole, C. S. Tiwary, and P. Kumbhakar, "Ethylenediamine assisted synthesis of wurtzite zinc sulphide nanosheets and porous zinc oxide nanostructures: near white light photoluminescence emission and photocatalytic activity under visible light irradiation," *CrystEngComm*, vol. 15, pp. 5515-5525, 2013.
- [33] S. Kar and S. Chaudhuri, "Controlled synthesis and photoluminescence properties of ZnS nanowires and nanoribbons," *The Journal of Physical Chemistry B*, vol. 109, pp. 3298-3302, 2005.
- [34] P. a. Hu, Y. Liu, L. Fu, L. Cao, and D. Zhu, "Self-assembled growth of ZnS nanobelt networks," *The Journal of Physical Chemistry B*, vol. 108, pp. 936-938, 2004.
- [35] X. Zeng, S. S. Pramana, S. K. Batabyal, S. G. Mhaisalkar, X. Chen, and K. Jinesh, "Low temperature synthesis of wurtzite zinc sulfide (ZnS) thin films by chemical spray pyrolysis," *Physical Chemistry Chemical Physics*, vol. 15, pp. 6763-6768, 2013.
- [36] E. Mosquera and N. Carvajal, "Low temperature synthesis and blue

- photoluminescence of ZnS submicronparticles," *Materials Letters*, vol. 129, pp. 8-11, 2014.
- [37] J. Varley and V. Lordi, "Electrical properties of point defects in CdS and ZnS," *Applied Physics Letters*, vol. 103, p. 102103, 2013.
- [38] V. Gopal, "A general relation between zero-bias resistance-area product and perimeter-to-area ratio of the diodes in variable-area diode test structures," *Semiconductor science and technology*, vol. 11, p. 1070, 1996.
- [39] A. Hood, M. Razeghi, E. H. Aifer, and G. J. Brown, "On the performance and surface passivation of type II InAs/GaSb superlattice photodiodes for the very-long-wavelength infrared," *Applied Physics Letters*, vol. 87, pp. 151113-151113-3, 2005.
- [40] H. Pagnia, "Field effect and surface photoconductivity studies on InSb films," *Surface Science*, vol. 10, pp. 239-253, 1968.
- [41] E. Kreutz, H. Pagnia, and W. Waidelich, "X-Ray Induced Conductivity Changes in InSb," *physica status solidi (b)*, vol. 27, pp. K111-K114, 1968.
- [42] A. Rogalski, *Infrared detectors*: CRC Press, 2010.
- [43] J. Rosbeck, I. Kasai, R. Hoendervoogt, and M. Lanir, "High performance Be<sup>+</sup> implanted InSb photodiodes," in *Electron Devices Meeting, 1981 International*, 1981, pp. 161-164.
- [44] I. Bloom and Y. Nemirovsky, "Surface passivation of backside-illuminated indium antimonide focal plane array," *Electron Devices, IEEE Transactions on*, vol. 40, pp. 309-314, 1993.
- [45] C. Hurwitz and J. Donnelly, "Planar InSb photodiodes fabricated by

Be and Mg ion implantation," *Solid-State Electronics*, vol. 18, pp. 753-756, 1975.

- [46] P. McNally, "Ion implantation in InAs and InSb," *Radiation Effects*, vol. 6, pp. 149-153, 1970.

## Chapter 6. Conclusions

In this thesis, I investigated how to growth high quality of InSb epitaxial layers and how to improve InSb PDs performances. Based on these purpose, this thesis is composed of three sections: surface preparation, InSb epilayer growth and its quality analysis and passivation for the InSb.

In order to growth high quality of InSb epilayers, the preparation of substrates where epilayers can be grown is very important and well prepared substrate is the first step of epitaxial growth. Two types of thermal cleaning method were investigated. First, InSb substrate was thermally cleaned under  $H_2$  ambient to suppress the Sb secondary phase formation. However, In droplets surrounded by rectangular etch pits were observed even though the thickness of native oxides became thin. To suppress the In droplet formation, InSb substrates were thermally cleaned under TMSb ambient. In this annealing condition, the formation of In droplet was inhibited completely. The surface morphology became smooth by suppressing the evaporation of Sb from the InSb surface as TMSb precursor was supplied. It was found that substrate preparation can affect to the quality of InSb epilayers. Crystal quality of InSb grown on InSb substrates thermally cleaned under TMSb ambient showed the better quality than that of InSb grown on InSb grown on InSb substrate thermally cleaned under  $H_2$  ambient. It was caused by the In droplet formed on the InSb surface, which interrupt the InSb growth to produce surfaces with cracks. It might also act as sources of extra In supply, to make non-stoichiometric InSb epilayer. From the PL measurements, red shift of near band edge emission was observed, which was originated from

the In related defect formation.

For the high quality InSb epilayer growth, growth parameters such as V/III ratio and growth temperature was varied. At a fixed growth temperature, In-rich InSb was grown at lower V/III ratio. On the other hand, Sb-rich InSb was grown at higher V/III ratio. At an optimized V/III ratio of 8.8, InSb epilayers with smooth surface morphologies and high crystal quality was observed. At low V/III ratio of 2.2, extra In was supplied to form a In droplet on the surface. In droplets were removed from the surface with increasing growth temperature at a fixed V/III ratio, implying that TMSb was not completely decomposed in this investigated growth temperature regions. The best surface morphology with high crystal quality of InSb epilayers can be grown at 490 °C under V/III ratio of 8.8.

Growth behaviors of InSb epilayers were investigated by changing growth temperature, group III mole fraction and group V mole fraction. From the experiments of growth rate vs growth temperature, it was found that InSb growth rate was controlled by the surface reaction kinetics. Its growth rate was dependent on the group III mole fraction but independent on the group V mole fraction due to the vapor pressure differences between In and Sb. Based on the growth behavior of InSb, TMIn was also incompletely decomposed in this investigated regions due to the H radicals depletion in TMIn decomposition. H radicals produced at TMIn decomposition process help to increase the TMSb decomposition.

From the PL measurements, near band edge emission was shifted with

dependence of V/III ratio. The peak position at highest emission energy was observed at InSb epilayers grown under V/III ratio of 8.8 and InSb samples grown at other V/III ratio was shifted toward lower emission energy. All InSb samples showed n-type conductivity. A carrier concentration of InSb epilayers grown at V/III ratio of 8.8 has the lowest values and it was gradually increased with decreasing or increasing V/III ratio, implying that donor types of charged impurity was incorporated into InSb epilayers with decreasing or increasing V/III ratio. It turned out to be an indium interstitial defect, which shows the lowest defect formation energy in In-rich and Sb-rich growth conditions.

The origin of new PL peak, which has not been reported yet, was investigated in this thesis. From the InSb epilayers grown at different growth temperature, it shows the the intensity of the new PL peak has relationship with growth temperatures. With increasing growth temperature, the intensity of the PL peak was decreased, implying that its origin was maybe related to the carbon from the metalorganic precursors. Carbon concentration measured by SIMS depth profiles shows the same trends with PL intensity. It indicates that the new PL peak was originated from the carbon.

P-type doping for InSb was studied using diethylzinc (DEZn). With increasing DEZn mole fraction, hole concentration increased linearly. With increasing growth temperatures, hole concentration was decreased due to the Zn re-evaporation on the surface due to the increase of vapor pressure of Zn.

For InSb surface passivation, ZnS films were deposited with dependence of deposition rate. High quality of interfacial properties at ZnS/InSb was

observed as compared to that of other passivation materials. It was caused by the S termination with InSb dangling bonds, producing In-S and Sb-S bonding. However  $D_{it}$  was gradually increased with increasing deposition rates, implying that the effect of S termination was reduced. In this deposition conditions, negative fixed charges density was reduced at 1.5 A/sec and it became positive fixed charges from the C-V measurements. This was due to the formation of positive fixed charges with increasing ZnS deposition rate. The formed sulfur vacancies, which have positive charges, can compensate the negative fixed charges existing on the InSb surface, introducing near flat-band condition near the surface. This charge compensation suppresses the surface leakage current.

ZnS passivation was found to be very effective way to reduce the dark current in mesa type InSb photodiodes. With ZnS passivation films, dark current was significantly reduced, introducing device performance such as spectral response. In case of ZnS passivation, the spectral response was even observed at 220 K which implies that the device operation temperature can be increased.

The reduction of surface leakage current was also influenced on the IR device performances such as responsivity and detectivity. When ZnS films were deposited, responsivity and detectivity was improved due to the reduction of surface leakage current by comparing to that of SiO<sub>2</sub> and unpassivation samples.

## Abstract (in Korean)

중적외선을 검출할 수 있는 적외선 감지 소자는 해외 선진국의 주도하에 군사용으로 개발이 되었지만, 현재는 산업용, 의료용에 이르기까지 그 활용 분야를 점점 확대하고 있다. 그 결과, 시장 규모도 급격하게 성장하고 있다. 하지만 해외 선진국에서는 적외선 감지 소자의 제작 기술을 수출 금지 품목으로 지정하여 기술의 해외유출을 엄격하게 제한하고 있다. 하지만 국내의 적외선 감지 소자 제작 기술은 기초 단계에 머물러 있기 때문에, 세계적인 기술 수준과의 격차를 좁히기 위해서 체계적인 연구가 시급하다.

중적외선 검출 소자의 재료로 가장 널리 사용되는 물질은 인듐안티모나이드 (InSb)이다. InSb는 밴드갭이 적외선 파장대 영역과 일치하며, III-V족 화합물 반도체 중에서 이동도가 가장 높기 때문에 매우 적합한 물질이다. 기존에는 n타입 기판에 p타입 물질을 확산 및 이온 주입 방법을 이용하여 소자를 제작하였지만, InSb 기판의 표면에 결함을 형성하여 소자의 동작 특성이 저하되는 문제점이 있다. InSb 에피 성장을 통해서 극복하고자 하는 노력이 있었지만, Sb의 특성 때문에 고품질의 InSb 에피층을 성장하는데 어려움이 있다. 따라서 본 연구에서는 유기금속화학기상증착법을 이용하여 InSb 에피층을 성장하고, 표면적, 구조적, 전기적, 광학적 분석을 체계적으로 진행하여 고품질의 에피층을 성장하는데 목적을 두었다. 또한 ZnS 표면 보호막 연구를 통하여 소자 동작 특성

향상에 대한 연구를 진행하였다.

고품질의 에피층을 성장하기 위한 첫 번째 전제조건은 eip-ready의 기판을 준비하는 것이다. As, P, N계열의 물질 성장과 달리 Sb는 낮은 평형 증기압 및 hydride 소스가 존재하지 않기 때문에 Sb 이차 상 (phase)형성과 같은 문제를 야기하여 기판 처리가 매우 어렵다. 따라서 Sb 분위기에서 열처리에 대한 논란이 많다. 하지만 본 연구에서 Sb 분위기에서 열처리는 매우 중요한 것을 발견하였다. Sb 분위기가 형성되지 않으면 표면에서 원하지 않는 In droplet과 직사각형 모양의 에칭 핏이 형성되기 때문이다. 이것은 InSb 기판에서 In과 Sb의 평형 증기압 차이에 따라서 Sb이 선택적으로 증발되기 때문이며, zinblende 구조의 에칭 특성이 열처리 과정 중에 반영되어 에칭 핏이 형성된다. 이런 열처리 조건은 이후에 형성되는 InSb 에피층의 특성에 영향을 주어 특성이 저하되는 결과를 초래하였다.

고품질의 박막을 성장하기 위해서 성장 변수 (V/III ratio, 성장 온도)를 변화하면서 최적화된 조건을 찾고, 에피층의 표면적, 구조적, 전기적, 광학적 특성을 평가하였다. 성장 온도는 490 °C, V/III ratio는 8.8에서 가장 우수한 품질의 InSb 에피층이 성장되었다. 저온에서 V/III ratio를 낮추면 In droplet이 형성되었으며, 충분한 Sb이 공급되지 못했기 때문이다. 고온에서 V/III ratio를 낮추면 In droplet 형성이 억제되었다. 이것은 TMSb 소스가 성장 온도

영역에서 충분히 분해가 되지 못했기 때문이며 성장 온도의 증가가 Sb를 추가적으로 공급하여 In droplet 형성을 억제하였다. InSb의 성장 거동 기구로부터 InSb의 성장 속도는 표면에서 반응속도 (surface reaction kinetic regime) 및 TMIIn 유량에 영향을 받지만, TMSb 유량에는 영향을 받지 않았다. 이 결과로부터 TMIIn 소스도 성장 온도 영역에서 충분한 분해가 일어나지 않는다는 것을 알 수 있다. 본 연구에서 InSb의 광학적인 분석을 통해서 2 가지 현상이 발견되었다. 첫 번째는, InSb의 밴드갭이 InSb의 조성에 의해 영향을 받았다. In이 충분한 조건에서 성장된 InSb 에피층에는 인듐 침입형 (Indium interstitial) 결함이 형성되어서 밴드갭 에너지가 줄어들게 보이는 효과를 보였다. 두 번째로, 기존에 보고되지 않은 탄소와 관련된 PL emission을 처음으로 발견하였고, 그 원인을 규명하였다.

마지막으로 소자 동작 특성을 향상하기 위해서 InSb의 표면 보호막으로 황화아연 (ZnS)을 연구하였다. 기존에 사용되는 SiO<sub>2</sub>는 절연막 증착 중 혹은 증착 후에 InSb의 자연 산화막 및 InSb와 계면 반응이 발생할 수 있다. 이러한 문제를 해결하기 위해서 황을 포함하는 황화아연은 표면 보호막으로 사용한 결과, SiO<sub>2</sub>를 증착한 것과 비슷한 우수한 계면 특성을 얻었으며, 이때 계면 트랩 밀도는  $2 \times 10^{11} \text{ cm}^{-2}\text{eV}^{-1}$ 였다. 화학적 조성이 불균일한 황화아연 박막의 증착을 통해서 평탄대 전압을 형성하여 표면 누설 전류 통로를 억제할 수 있었고, 그 결과 표면 누설 전류가 억제되는 것을 관찰하였다.

ZnS의 증착 유무에 따라서 적외선 감지 소자의 동작 특성을 관찰하였다. 그 결과, 표면 보호막을 증착하지 않은 샘플에 비하여 암전류는 감소하였다. 이것은 표면으로 흐르는 표면 누설 전류가 억제되어서 총 암전류 값이 감소를 하였다. 또한 소자의 spectral response에도 영향을 주었다. ZnS 표면 보호막이 증착되면 약 10배의 강도가 증가하였으며, 온도 의존성에서도 더 높은 온도에서 spectral response가 관찰되었다. 또한 반응도 (Responsivity)와 검출도 (Detectivity)와 같은 적외선 소자의 특성 측정을 통해서도 ZnS 표면 보호막이 증착이 되면 소자 특성이 향상되는 것이 관찰이 되었으며, 이것은 ZnS 표면 보호막의 증착이 표면 누설 전류를 줄여서 암전류, spectral response, 반응도, 검출도와 같은 기본적인 검출소자의 동작 특성 향상에 영향을 주었음을 보여주는 것이다.

---

---

### 주요어 :

인듐안티모나이드, 저압 유기화학기상증착법, 적외선 감지 소자, 실시간 열처리, 광발광, p타입 도핑, 황화아연, 표면 보호막, 표면 누설 전류, 광반응도, 광검출도

학번 : 2009-20602

---

---

# Publication List

## Journal Papers:

### International

1. **Sehun Park**, Jinwook Jung, Chulkyun Seok, Keun Wook Shin, Sung Hyun Park, Yasushi Nanishi, Yongjo Park and Euijoon Yoon, “Effects of TMSb overpressure on InSb surface morphology for InSb epitaxial growth using low pressure metalorganic chemical vapor deposition”, *Journal of Crystal Growth*, 401, 518 (2014)
2. **Sehun Park**, Daehan Choi, Hwanyeol Park, Daeyoung Moon, Duk Kyu Bae, Yongjo Park and Euijoon Yoon, “Suppression of surface leakage current in InSb photodiode by ZnS passivation”, *International Journal of Nanotechnology*, Accepted, (2015)
3. **Sehun Park**, Hwanyeol Park, Jinwook Jung, Daeyoung Moon, Min-Su Park, Dae-Myeong Geum, Sang Hyuk Kim, Won Jun Choi, Jin Dong Song, Eunsoo Oh, Yongjo Park and Euijoon Yoon, “Photoluminescence and intrinsic properties of MOCVD grown InSb epitaxial films” (In preparation)
4. Jaeyel Lee, **Sehun Park**, Jungsub Kim, Changjae Yang, Sujin Kim, Chulkyun Seok, Jinsub Park and Euijoon Yoon, “Comparative analysis of oxide phase formation and its effects on electrical properties of

- SiO<sub>2</sub>/InSb metal-oxide-semiconductor structures”, Thin Solid Films, 520, 5385 (2012)
5. Jinsub Park, Daeyoung Moon, **Sehun Park**, Sung Hyun Park and Euijoon Yoon, “Growth of GaN layer on patterned Al/Ti Metal mask by metal organic chemical vapor deposition”. Japanese Journal of Applied Physics, 51, 025501 (2012)
  6. Chulkyun Seok, Minkyung Choi, **Sehun Park**, Jinwook Jung, Yongjo Park, In-Sang Yang and Euijoon Yoon, “Raman spectroscopy of the damages induced by Ar-ion beam etching of InSb (100) surface”, ECS Solid State Letters, 3, P27 (2014)
  7. Kuen Wook Shin, Sung Hyun Park, Sewoung Oh, **Sehun Park**, Yongjo Park, Euijoon Yoon, “Reduction of threading dislocations in Ge epitaxial layers on Si (001) substrates by rapid thermal annealing”, Journal of Korean Physics Society.
  8. Xiren Chen, Jinwook Jung, Zhen Qi, Liangqing Zhu, **Sehun Park**, Liang Zhu, Euijoon Yoon and Jun Shao, “ Infrared photorefectane investigation of resonant levels and band edge structures in InSb”, Optical Letters, 40, 5295 (2015)

## **Domestic**

1. 김정섭, 하승규, 양창재, 이재열, **박세훈**, 최원준, 윤의준, “유기금속화학기상증착법을 이용한 적층 InAs 양자점 적외선 수광 소자 성장 및 특성 평가 연구 (Study of multi-stacked InAs quantum dot infrared photodetectors grown by metal organic chemical

vapor deposition)”, 한국진공학회지, 19, 217, (2010)

## **Proceedings:**

### **International**

1. Chulkyun Seok, Minkyung Choi, In-Sang Yang, **Sehun Park**, Yongjo Park and Euijoon Yoon, “Multi-step plasma etching process for development of highly photosensitive InSb mid-IR FPAs”, in Proc. SPIE 9070, Infrared Technology and Applications XL, (2014)
2. Chulkyun Seok, Sujin Kim, Jaeyel Lee, **Sehun Park**, Yongjo Park and Euijoon Yoon, “Analysis of failure of C-V characteristics of MIS structure with SiO<sub>2</sub> passivation layer deposited on InSb substrate via Raman spectroscopy”, in MRS/Proceedings, Vol. 1670 (2014)

## **Patents:**

1. 박세훈, 윤의준, 박용조, 김치연, “적외선 감지 소자 및 적외선 감지 소자의 제조 방법 (PHOTODIODE AND METHOD OF MANUFACTURING THE SAME)”, 출원번호: 10-2015-0165786

## Conference Presentation:

### International

1. **Sehun Park**, Daehan Choi, Hwanyeol Park, Daeyoung Moon, Yongjo Park, Euijoon Yoon, “Study of InSb surface passivation and its effects on electrical properties”, 16<sup>th</sup> International Conference on Thin Films (ICTF-16), October, 13-16, Dubrovnik, Croatia, (**Awarded as a best oral presentation**)
2. **Sehun Park**, Jinwook Jung, Sung Hyun Park, Chulkyun Seok, Keun Wook Shin, Yasushi Nanishi and Euijoon Yoon “Effects of TMSb overpressure on InSb surface morphologies during a thermal cleaning process by low pressure metalorganic chemical vapor deposition” 17<sup>th</sup> International Conference on Crystal Growth and Epitaxy (ICCGE-17), August, 11-16 2013, University of Warsaw, Warsaw, Poland
3. **Sehun Park**, Chulkyun Seok, Sujin Kim, and Euijoon Yoon “Effects of deposition temperatures on the chemical species formation at the interfaces of Si<sub>3</sub>N<sub>4</sub>/InSb structures” SNU-Ritsumeikan Joint Workshop, Mar 09, Ritsumeikan Univ. Japan
4. **Sehun Park**, Jaeyel Lee, Jungsub Kim, Changjae Yang, Sujin Kim, Chulkyun Seok, Jinsub Park, Euijoon Yoon “Quantitative analysis of formation and thermal stability of oxide phases between SiO<sub>2</sub> and InSb” SPIE Photonics West 2011, Jan 22~27, Moscone center, San Francisco, USA

5. **Sehun Park**, Jaeyel Lee, Sujin Kim, Chulkyun Seok, Changjae Yang, Jinsub Park, Euijoon Yoon, “The origin of interface states in  $\text{Si}_3\text{N}_4/\text{InSb}$  and  $\text{SiO}_2/\text{InSb}$  MOS structure for InSb photodiodes” The 6<sup>th</sup> SNU-Ritsumeikan University Joint workshop on compound semiconductors, NOV, 10, 2010, ISRC, SNU, Korea
6. **Sehun Park**, Jaeyel Lee, Jungsub Kim, Jujin Kim, Chulkyun Seok, Changjae Yang, Jinsub Park, Euijoon Yoon, “ The analysis of interface property between dielectric ( $\text{Si}_3\text{N}_4$ ,  $\text{SiO}_2$ ) and InSb for infrared photo-detector application” International Union of Materials Research Societies-International Conference on Electronic Materials 2010 (IUMRS-ICEM 2010), Aug 22~27, 2010, KINTEX, Seoul, Korea.
7. **Sehun Park**, Sung Hyun Park, Chulkyun Seok, Sujin Kim and Euijoon Yoon, “Effects of deposition temperatures on the chemical species formation at the interfaces of  $\text{Si}_3\text{N}_4/\text{InSb}$  structures fabricated by plasma enhanced chemical vapor deposition”, ISPlasma2012, Mar 4-8, 2012, Chubu University, Japan,
8. Chulkyun Seok, **Sehun Park**, Jinwook Jung, Yongjo Park and Euijoon Yoon, “Ion beam induced structural damages on InSb surface studied by Raman spectroscopy”, 16<sup>th</sup> International Symposium on the Physics of Semiconductors and Applications (ISPSA 2013), July 3-5, Ramada Plaza Jeju Hotel, Jeju, Korea
9. Jaeyel Lee, **Sehun Park**, Jungsub Kim, Changjae Yang, Euijoon Yoon, “The study of  $\text{SiO}_2$  passivation layers grown by plasma enhanced chemical vapor deposition for InSb photodiodes”, 30<sup>th</sup> International Conference on the Physics of Semiconductors (ICPS 2010), 2010, 07.25~30, COEX, Seoul, Korea

10. Jaeyel Lee, **Sehun Park**, Jungsub Kim, Changjae Yang, Sujin Kim, Jinsub Park, Euijoon Yoon, “Comparative analysis of oxide phase formation and its effects on electrical properties of SiO<sub>2</sub>/InSb MOS structures”, 30<sup>th</sup> International Conference on the Physics of Semiconductors, July 25~30, 2010, COEX, Seoul, Korea
11. Jaeyel Lee, **Sehun Park**, Jungsub Kim, Changjae Yang, Sujin Kim, Jinsub Park, Euijoon, “Correlation between In and Sb oxide at SiO<sub>2</sub>/InSb interface and electrical properties of InSb MOS structures” 10<sup>th</sup> Asia-Pacific Conference on Plasma Science and Technology (APCPST), July 4~8, 2010, Jeju, Korea
12. Jinsub Park, SungHyun Park, **Sehun Park**, Duck-Jae You, Daeyoung Moon, Euijoon Yoon, “Growth of a-plane GaN on vicinal r-plane sapphire substrates” SPIE Photonics West 2011, Jan 22~27, Moscone center, San Francisco, USA (Poster)
13. Jungsub Kim, Seung-Kyu Ha, Changjae Yang, Jaeyel Lee, **Sehun Park**, Won Jun Choi Euijoon Yoon, “Characteristics of multi-stacked InAs/InGaAs dot-in-a-well structures grown by metal organic chemical vapor deposition for quantum dot infrared photodetector” ” International Union of Materials Research Societies-International Conference on Electronic Materials 2010 (IUMRS-ICEM 2010), Aug 22~27, 2010, KINTEX, Seoul, Korea
14. Jungsub Kim, Changjae Yang, Uk Sim, Jaeyel Lee, **Sehun Park**, Euijoon Yoon, “ The study of InAs quantum dots grown by using Sb surfactant during the post growth interruption”, International Union of Materials Research Societies-International Conference on Electronic Materials 2010 (IUMRS-ICEM 2010), Aug 22~27, 2010, KINTEX, Seoul, Korea (

15. J. Lee, J. Kim, C. J. Yang, **S. Park**, and E. Yoon, "The study of passivation layers grown by PECVD for InSb infrared" 2nd International conference on microelectronics and plasma technology (ICMAP), 2009. 9.22~25, Busan, Korea
16. J. Kim, S. -K. Ha, C. Yang, J. Lee, **S. Park**, W. J. Choi and E. Yoon, "Fabrication of multi-stacked InAs/InGaAs dot-in-a-well structures by metal organic chemical vapor deposition for quantum dot infrared photodetector", 30<sup>th</sup> International Conference on the physics of Semiconductors (ICPS 2010), 2010.07.25~30, COEX, Seoul, Korea
17. Jungsub Kim, Seung-kyu Ha, Changjae Yang, Jaeyel Lee, **Sehun Park**, Won Jun Choi and Euijoon Yoon "The study of multi-stacked InAs/InGaAs dot-in-a-well structures for quantum dot infrared photodetector by metal organic chemical vapor deposition" The 6<sup>th</sup> International Conference on Semiconductor Quantum Dots, (Quantum dot 2010), 2010.04.26~30, East Midlands Conference Centre, Nottingham, UK

## **Domestic**

1. **박세훈**, 정진욱, 석철균, 신상훈, 송진동, 윤의준, "유기금속화학기상증착법을 이용한 InSb의 p타입 도핑 연구", 2013 한국군사과학기술학회, 2013.07.03, 제주컨벤션센터, 제주도
2. **박세훈**, 이재열, 김정섭, 김수진, 석철균, 양창재, 박진섭, 윤의준, "InSb 적외선 감지 소자용 Si<sub>3</sub>N<sub>4</sub>, SiO<sub>2</sub> 절연막 계면 특성 연구"

- 제 39 회 하계 한국진공학회, 2010, 08, 20, 비체펠리스, 충남 보령,
3. **박세훈**, 이재열, 김정섭, 양창재, 이강일, 국승희, 서광석, 한민구, 윤의준, “The study of SiO<sub>2</sub>, Si<sub>3</sub>N<sub>4</sub> passivation layers of InSb photodetector”, 2010 한국군사과학기술학회, 2010. 06. 17 제주컨벤션센터, 제주도
  4. **박세훈**, 이재열, 김정섭, 양창재, 윤의준, “InSb 적외선 감지소자 pn 접합 형성 연구”, 제 38 회 한국진공학회 학술대회, 2010. 2. 19. 현대성우리조트, 강원도 횡성
  5. 정진욱, **박세훈**, 석철균, 박용조, Xiren Chen, Jun Shao, 윤의준 “Unusual Photoluminescence Peak Shift of InSb Epitaxial Layers Grown by LP-MOCVD”, 제 21 회 한국반도체학술대회, 2014. 02.24~26, 한양대학교
  6. 정진욱, **박세훈**, 석철균, 윤의준, “Homo-epitaxial growth of inSb by MOCVD”, 2012 한국광전자학회, 2012, 11, 15, 광주과학기술원
  7. 석철균, **박세훈**, 정진욱, 박용조, 윤의준 “ 고성능 중적외선 검출소자 제작을 위한 InSb 플라즈마 식각 방법 비교 연구”,

2013 한국군사과학기술학회, 2013. 07.03, 제주컨벤션센터,  
제주도

8. 정진욱, 박세훈, 석철균, 박용조, 윤의준,  
“ 유기화학기상증착법을 이용한 고품질의 InSb 에피 성장”, 제  
9 회 국방기술학술대회, 2013. 10.11~12, 고려대, 서울
9. 석철균, 정진욱, 박세훈, 박용조, 윤의준, “ 고성능 중적외선  
검출소자 제작을 위한 인듐안티모나이드 (InSb)의 2-step 식각  
공정 연구”, 제 9 회 국방기술학술대회, 2013. 10.11~12,  
고려대, 서울
10. 석철균, 최민경, 정진욱, 박세훈, 박용조, 양인상, 윤의준  
“Effects of Surface Damage on Raman Spectrum of Etched  
InSb (100) Surface” 제 21 회 한국반도체학술대회, 2014.  
02.24~26, 한양대학교
11. 이재열, 김정섭, 양창재, 박세훈, 윤의준, “The Study of SiO<sub>2</sub>,  
Si<sub>3</sub>N<sub>4</sub> passivation layers grown by PECVD for the indium  
antimonide photodetector”, 한국재료학회 추계 학술대회,  
2009. 11. 5. 포항공과대학교, 경상북도 포항시

12. 이재열, 김정섭, 양창재, **박세훈**, 윤의준, “InSb 적외선 감지소자용  $\text{SiO}_2$ ,  $\text{Si}_3\text{N}_4$  절연막 연구”, 제 17 회 지상무기학술대회, 2009. 9. 16. 대전컨벤션센터, 대전
13. 이재열, 김정섭, 양창재, **박세훈**, 윤의준, “PECVD 로 증착한 InSb 적외선 감지소자용  $\text{Si}_3\text{N}_4$  절연막에 대한 연구”, 제 37 회 한국진공학회 하계 학술대회, 2009. 8. 21. 오션리조트, 전라남도 여수시
14. 이재열, 김정섭, 양창재, **박세훈**, 윤의준, “Study of passivation layers for indium antimonide photodetectors”, 한국재료학회 추계 학술대회, 2009. 5. 22. 무주리조트, 전라북도 무주
15. 김정섭, 하승규, 양창재, 이재열, **박세훈**, 최원준, 윤의준, “Study of multi-stacked InAs quantum dot infrared photodetector grown by metal organic chemical vapor deposition”, 제 38 회 한국진공학회 학술대회, 2010. 2. 19. 현대성우리조트, 강원도 횡성
16. 정진욱, **박세훈**, 석철균, 윤의준, “유기화학기상증착법을 이용한 InSb 동종 에피성장 연구”, 2013 한국군사과학기술학회, 2013.07.03, 제주컨벤션센터, 제주도

17. 석철균, **박세훈**, 정진욱, 윤의준, “고성능 증적외선 검출소자 제작을 위한 InSb 플라즈마 식각 방법 비교 연구”, 2013 한국군사과학기술학회, 2013.07.03, 제주컨벤션센터, 제주도

### **Awarded Event:**

1. **“Young Researcher Award”**, Sehun Park, Daehan Choi, Hwanyeol Park, Daeyoung Moon, Yongjo Park, Euijoon Yoon, “Study of InSb surface passivation and its effects on electrical properties”, 16<sup>th</sup> International Conference on Thin Films (ICTF-16), October, 13-16, Dubrovnik, Croatia,
2. 2009 년 캠퍼스 특허전략 유니버시아드, 선행기술 조사부문, **장려상**, “E5. 연속주조 방법에 따라 강제품을 연속으로 제조하는 방법 및 장치”
3. 2010 년 캠퍼스 특허전략 유니버시아드, 선행기술 조사부문, **장려상**, “E5. 자기세정 강판 관련 특허”